Experimental Study on Immersion Freezing of Size Selected Mineral Dust Particles

A dissertation submitted to the

ETH ZURICH

for the degree of

Doctor of Sciences

presented by

FELIX LÜÖND

Dipl. Phys. ETH Zürich

born 22 November 1980

citizen of Sattel (SZ)

accepted on the recommendation of

Prof. Dr. Ulrike Lohmann, examiner
Dr. Olaf Stetzer, co-examiner
Dr. Frank Stratmann, co-examiner

2009

Abstract

Atmospheric ice nucleation has a large influence on the hydrological cycle and cloud radiative properties. In mixed-phase clouds occurring at temperatures between 0°C and roughly -40°C, ice predominantly nucleates by one of the four heterogeneous modes of ice nucleation involving the presence of an insoluble ice nucleus (IN). These modes are contact freezing, immersion freezing, condensation freezing and deposition nucleation. Although heterogeneous ice nucleation has been extensively studied in the past, there is still a lack in understanding which intrinsic properties define the efficiency of an IN. Often, different modes of ice nucleation cannot be separated in an experiment, and a variety of experimental techniques leads to a large scatter in the measured data.

In the present thesis, a new instrument has been developed, based on the principle of a continuous flow diffusion chamber (CFDC), to measure ice nucleation in the immersion mode with single immersed aerosol particles. The "immersion mode cooling chamber" (IMCA) produces cloud droplets with single immersed particles by cloud droplet activation of aerosol particles, and gradually cools them to the experimental temperature at which the frozen fraction of the droplets is measured. IMCA is coupled to the Zurich ice nucleation chamber (ZINC) which keeps the experimental temperature constant at a relative humidity close to water saturation. Water saturation is established to prevent droplets from evaporating before reaching the detector. The frozen fraction of droplets is measured at the bottom of ZINC by the "ice optical detector device" (IODE), a recently developed depolarization detector. Droplet activation of the aerosol particles occurs in the warm part of IMCA where supersaturation with respect to liquid water is established by applying different temperatures to both humidified chamber walls. Computational fluid dynamics (CFD) simulations have been performed to find suitable chamber dimensions and experimental parameters to grow nucleated droplets large enough that they do not evaporate in subsaturated zones before reaching the detector.

First experiments with IMCA on freezing of cloud droplets in the immersion mode have been successfully conducted. Experiments with size selected kaolinite particles between 200 nm and 800 nm in diameter have yielded median freezing temperatures between -35°C for 200 nm particles and -33°C for 800 nm particles. The influence of particle size is not very strong, but clearly discernable. Above the median freezing temperature, the decrease of the frozen fraction of cloud droplets is slower than expected from nucleation theory. This gives rise to the conjecture that there is a small contribution from deposition nucleation to the ice crystals identified by the detector. Although calculation of the droplet evolution based on the CFD simulations does not predict droplets to evaporate before reaching the detector, a certain amount of unactivated aerosol particles is likely to be present in the experiment and nucleate ice in the deposition mode. This contradiction to the calculation is probably due to the simplified assumption of immediate droplet nucleation at the top of IMCA. The contribution of deposition nucleation has been estimated and subtracted from the measured ice crystals to isolate immersion freezing.

The measured frozen fraction of droplets has been fitted to nucleation theory using models with differing description of the IN surface. Whereas a model assuming a constant contact angle between IN and ice embryo for all IN poorly represent the data, best fits have been obtained with models distributing active sites, i. e. preferential sites for nucleation, of different efficiency on the IN surface. The resulting fits suggest that the dependence of IN efficiency on particle size is not only based on the larger surface area of larger particles, but also on the higher probability for active sites of high efficiency on a larger surface area. More experiments assessing the time dependence of freezing are required to decide whether

such a model is preferentially based on classical nucleation theory (CNT) or if a simpler deterministic model can be used to describe immersion freezing.

Zusammenfassung

Eisnukleation in der Atmosphäre hat einen starken Einfluss auf den hydrologischen Zyklus und auf die Strahlungseigenschaften von Wolken. In Mischphasenwolken, die bei Temperaturen zwischen 0°C und ungefähr -40°C auftreten, bilden sich Eiskristalle vorwiegend durch einen der vier heterogenen Eisnukleations-Mechanismen, die jeweils die Anwesenheit eines unlöslichen Eiskeims (IN) voraussetzen. Zu diesen Mechanismen zählen Kontaktgefrieren, Immersionsgefrieren, Kondensationsgefrieren und Depositionsnukleation. Obwohl heterogene Eisnukleation schon ausführlich untersucht wurde, ist das Verständnis davon, welche spezifischen Eigenschaften die Effizienz eines IN bestimmen, nach wie vor lückenhaft. Oftmals können einzelne Eisnukleations-Mechanismen in einem Experiment nicht voneinander getrennt werden, und eine Vielfalt an experimentellen Methoden führt zu einer beträchtlichen Streuung der Messdaten.

In dieser Arbeit wurde ein neues Gerät entwickelt, um das Immersionsgefrieren von Wolkentröpfchen mit je einem Aerosolpartikel pro Tröpfchen zu untersuchen. Die "immersion mode cooling chamber" (IMCA) basiert auf dem Prinzip einer Diffusionskammer mit kontinuierlichem Durchfluss. Sie generiert Wolkentröpfchen mit einzelnen Partikeln mittels Wolkentröpfchen-Aktivierung der Partikel, und kühlt die Tröpfchen graduell zu einer Temperatur, bei der der gefrorene Anteil der Tröpfchen gemessen wird. Die IMCA-Kammer ist vertikal an die "Zurich ice nucleation chamber" (ZINC) gekoppelt, welche diese Temperatur bei einer relativen Feuchte nahe der Wassersättigung konstant hält. Diese Feuchte ist notwendig, um zu verhindern, dass die Tröpfchen verdunsten, bevor sie den Detektor erreichen. Der gefrorene Anteil der Tröpfchen wird am unteren Ende von ZINC mittels dem kürzlich entwickelten Depolarisations-Detektor IODE (ice optical detector device) ermittelt. Tröpfchen-Aktivierung der Aerosol-Partikel geschieht im oberen, warmen Teil von IMCA, wobei Übersättigung in Bezug auf flüssiges Wasser durch Befeuchtung der Wände und Einstellen verschiedener Wandtemperaturen erreicht wird. Mittels numerischer Strömungssimulationen wurden geeignete Kammerdimensionen und experimentelle Parameter ermittelt, damit die aktivierten Tröpfchen zu ausreichender Grösse anwachsen können, um in den untersättigten Bereichen des Experiments nicht vollständig zu verdunsten.

Erste Experimente mit IMCA zum Immersions-Gefrieren von Wolkentröpfchen konnten erfolgreich durchgeführt werden. Mit grössen-selektierten Kaolinitpartikeln zwischen 200 nm und 800 nm Durchmesser wurden mittlere Gefriertemperaturen zwischen -35°C für 200 nm Partikel und -33°C für 800 nm Partikel gemessen. Obwohl der Einfluss der Partikelgrösse auf die Gefriertemperatur nicht sehr stark ist, so ist er doch klar erkennbar. Oberhalb der mittleren Gefriertemperatur fällt der Anteil gefrorener Tröpfchen mit steigender Temperatur langsamer ab, als die Nukleationstheorie erwarten lässt. Dies gibt Anlass zur Vermutung, dass ein kleiner Teil der Eiskristalle, die vom Detektor identifiziert werden, via Depositionsnukleation entstehen. Obwohl die Berechnung der Tröpfchen-Evolution basierend auf den CFD-Simulationen kein Verdunsten der Tröpfchen voraussagt, bevor diese den Detektor erreichen, ist es doch wahrscheinlich, dass eine gewisse Anzahl unaktivierter Aerosolpartikel im System präsent sind. Dieser Widerspruch zur Berechnung ist wahrscheinlich darin begründet, dass in der Berechnung vereinfachend eine unmittelbare Wolkentröpfchen-Aktivierung angenommen wird, sobald die Partikel in den übersättigten Bereich von IMCA eintreten. Der Beitrag von Depositionsnukleation zur Anzahl gemessener Eiskristalle wurde abgeschätzt und vom Messwert abgezogen, um den Mechanismus des Immersionsgefrierens zu isolieren.

Der gemessene Anteil gefrorener Tröpfchen wurde zudem mit verschiedenen theoretischen Mod-

ellen gefittet, welche verschiedene Beschreibungen der IN-Oberfläche beinhalten. Die Annahme eines konstanten Kontaktwinkels zwischen IN und Eis-Embryo für alle IN ergibt einen mangelhaften Fit an die gemessenen Daten. Die besten Fits wurden mit Modellen erzielt, welche "aktive Stellen", d. h. bevorzugte Stellen für Eisnukleation, von verschiedener Effizienz auf der IN-Oberfläche verteilen. Die resultierenden Fits legen den Schluss nahe, dass die Abhängigkeit der IN-Effizienz von der Partikelgrösse nicht allein in der grösseren Oberfläche grösserer Partikel begründet ist, sondern auch in der erhöhten Wahrscheinlichkeit für effiziente aktive Stellen auf einer grösseren Oberfläche. Weitere Experimente zur Zeitabhängigkeit des Gefrierens von Tröpfchen sind notwendig, um zu entscheiden, ob ein Modell zur Beschreibung von Immersiongefrieren auf der klassischen Nukleationstheorie basieren sollte, oder ob ein einfacheres, deterministisches Modell ausreicht.

Contents

List of Symbols and Abbreviations

Symbol	Unit	Description
AIDA		Aerosol interaction and dynamics
AFT-IR		Aerosol flow tube infrared spectroscopy
APS		Aerodynamic particle sizer
AS		Active site
ATD		Arizona test dust
CDNC		Cloud droplet number concentration
CFD		Computational fluid dynamics
CFDC		Continuous flow diffusion chamber
CCN		Cloud condensation nucleus
CNT		Classical nucleation theory
CPC		Condensation particle counter
CU1, CU2		Cooling unit 1 and 2 (IMCA)
DC		Direct current
DMA		Differential Mobility Analyzer
FINCH		Fast ice nucleation chamber
FROST		Freezing of dust (campaign)
GS		Growth section (IMCA)
IMCA		Immersion mode cooling chamber
IN		Ice nucleus
IODE		Ice optical detector
IPCC		Intergovernmental panel on climate change
IS		Inlet section (IMCA)
LACIS		Leipzig aerosol cloud interaction simulator
MCA		Multi channel analyzer
OPC		Optical particle counter
PDF		Probability density function
PID		Proportional, integral, derivative
PMT		Photomultiplier tube
RMSE		Root mean square error
SMPS		Scanning mobility particle sizer
SS		Supercooling section (IMCA)
TDFR		Time dependent freezing rate
TOA		Top of the atmosphere
TR		Transition to ZINC (IMCA)
UDF		User defined function (FLUENT)
W-CPC		Water based condensation particle counter
ZINC		Zurich ice nucleation chamber
a	m	Droplet radius

x

p	Pa	Pressure
p_0	Pa	Standard atmospheric pressure, 1013.25 hPa
p_{frz}	-	Freezing probability of a droplet
p_{op}	Pa	Operating pressure used in FLUENT simulations
p_α	-	Freezing probability of a droplet containing one active site with contact angle α
q	J m^{-3}	Enthalpy per unit volume
r_i	m	Radius of a cluster of a condensed phase with i molecules
r_{crit}	m	Radius of a critical cluster of a condensed phase
r_N	m	Radius of IN
R	J K^{-1} mole^{-1}	Universal gas constant
Re	-	Reynolds number
RH	-	Relative humidity
RH_i, RH_w	-	Relative humidity with respect to ice and water, respectively
S	-	Saturation ratio
S_w, S_i	-	Saturation ratio with respect to water and ice, respectively
t	s	Time
t_{ZINC}	s	Residence time in ZINC
T	K	Temperature
T_0	K	Melting temperature of pure water, 273.15 K
T_a	K	Droplet temperature (radius a)
T_c, T_w	K	Temperature of the cold and warm wall of ZINC or IMCA
T_c	K	Characteristic freezing temperature of an IN
T_{in}	K	Sample temperature in the inlet of IMCA
T_m	K	Median freezing temperature
T_{top}	K	Sample temperature at the top of IMCA
T_{ZINC}	K	Temperature at sample position in ZINC
T_∞	K	Temperature far away from a droplet
U	J	Internal energy (of a droplet)
v	m s^{-1}	Flow velocity
$\bar{v}_v$	m s^{-1}	Mean molecular speed in a Maxwell-Boltzmann gas
V	m^3	Volume
w	m	Width of the aerosol layer in IMCA
x_v	-	Mole fraction of water vapour
α	-	Contact angle
α_c	-	Condensation coefficient of water vapour
α_e	-	Evaporation coefficient of water vapour
α_m	-	Mass fraction of water vapour
α_T	-	Thermal accommodation coefficient
δ	-	Depolarization ratio
ΔF_{diff}	J	Diffusion activation energy to cross the water/ice interface
ΔG	J	Energy barrier to form a critical cluster of a condensed phase
Δ_v	m	Vapour jump length
η_a, η_v	Pa s	Dynamic viscosity of air and water vapour, respectively
λ_{air}	m	Mean free path of air
μ_w, μ_i	J	Chemical potential of water and ice, respectively
μ_{BG}	pW	Average IODE background signal
ν	-	Dissociation coefficient of a salt
ρ	kg m^{-3}	Mass density

$\rho(\alpha)$	m^{-2}	Surface density of active sites within unit contact angle interval around α
ρ_a, ρ_v, ρ_w	kg m^{-3}	Mass density of air, water vapour and water, respectively
σ	J m^{-2}	Surface tension
$\sigma_{w,v}$, $\sigma_{i,v}$, $\sigma_{i,w}$	J m^{-2}	Surface tension of a water/vapour, ice/vapour, and ice/water interface
σ_{BG}	pW	Standard deviation of IODE background signal
$\sigma_\parallel$	pW	Standard deviation of parallel channel signal (IODE)
$\sigma_\perp$	pW	Standard deviation of perpendicular channel signal (IODE)
τ	pW	Peak detection threshold (IODE)
τ_δ	-	Depolarization threshold (IODE)
Φ_s	-	Osmotic coefficient of a solution

Chapter 1

Introduction

1.1 Atmospheric Aerosol

An aerosol is technically defined as a suspension of fine solid or liquid particles in a gas. However, the term "aerosol" in common use refers to the particulate phase only (Seinfeld and Pandis, 2006). Aerosol particles can appear as primary aerosols from sources on the earth's surface, or as secondary aerosols nucleated in the atmosphere from gaseous precursors (e. g. Kulmala et al. (2000)). Aerosol particles cover a wide variety of chemical compositions and sizes between a few nanometers and tens or hundreds of micrometers. A typical size distribution of ambient aerosol particles shows three modes: The nucleation or Aitken mode includes partices between 5 nm and 100 nm in diameter. Particles in the nucleation mode can originate from gas-to-particle conversions by homogeneous nucleation in supersaturated vapours or from homogeneous nucleation by gas phase chemical reactions (Pruppacher and Klett, 1997). They can also consist of primary particles from natural or anthropogenic combustion processes. In polluted urban areas, high concentrations of nucleation mode particles can be measured. Particles can be removed from the nucleation mode by coagulation with larger particles. The accumulation mode comprises particle sizes between 100 nm and around 1 μm, whereas particles larger than 1 μm constitute the coarse mode. Particles can be transferred from the nucleation mode to the accumulation mode by coagulation or by growth of small particles by vapour condensation. They can "accumulate" in this mode because removal processes are less efficient in this size range: Neither Brownian diffusion nor inertial impaction efficiently coagulates particles, and sedimentation is not efficient due to the small particle mass. Major removal processes for this mode is wet deposition by hydrometeors. The coarse mode mainly consists of primary natural aerosol particles like mineral dust, volcanic ash, sea salt and biological particles. These particles can efficiently be removed from the atmosphere by sedimentation. The residence time of aerosol particles strongly depends on the size of the particles and the location within the atmosphere. Coarse mode particles are removed by dry or wet deposition within days. For particles which are small enough to be transported above the tropopause, residence times can be weeks or even months as they cannot be removed by scavenging in or below clouds.

The chemical composition and size distribution of aerosol particles is highly variable in time and space. The sources of aerosol particles are very inhomogeneously distributed over the planet; E. g. mineral dust particles can be emitted from desert and large agricultural regions. Organic compounds are emitted from vegetated areas or originate from human activity in populated regions. Depending on their residence time in the atmosphere, aerosol particles can undergo changes in composition by coagulation with particles of different chemical composition or by coating with soluble or partly soluble compounds (e.g. sulfates, nitrates, organics). Such processes can substantially influence the interaction of aerosol particles with clouds, which is discussed in the next section.

1.2 Influence of Aerosols in the Atmosphere

Besides their impact on human health, aerosol particles have a significant effect on global climate by influencing the earth's radiative budget and its hydrological cycle. Their ability to scatter and absorb incoming solar radiation as well as outgoing longwave radiation defines the "direct aerosol effect" (Lohmann and Feichter, 2005). The direct radiative forcing of aerosol particles depends on their optical properties and on their location. Whereas strongly scattering particles exert a negative, i. e. cooling, top-of-the-atmosphere (TOA) forcing, partially absorbing particles located over bright surfaces like snow, ice, or deserts can have a positive TOA direct radiative forcing (Forster et al., 2007).

Furthermore, aerosol-cloud interactions give rise to several indirect aerosol effects on global climate. These interactions are based on the ability of a subset of the aerosol particles to act as cloud condensation nuclei (CCN) or as ice nuclei (IN). Due to their high albedo, clouds have a cooling effect on climate which amounts to an average TOA loss of -48 Wm^{-2} in the solar spectrum (Lohmann and Feichter, 2005). A cloud-free atmosphere would have an average albedo of 15% compared to 50% for a total overcast with clouds (Twomey, 1974). Indirect effects of anthropogenic aerosol particles on clouds as important regulators of the Earth's radiation budget can therefore cause significant radiative forcings as compared to pre-industrial time.

1.2.1 Indirect Aerosol Effects

The most important indirect aerosol effects can be summarized as follows:

- **Cloud albedo effect** An increased number concentration of CCN increases the cloud droplet number concentration (Twomey and Warner, 1967) and reduces the cloud droplet size, if the cloud water content remains constant. This effect is also called first indirect aerosol effect or Twomey effect. An increased number density of cloud droplets increases the cloud optical thickness und thus the cloud albedo (Twomey, 1974) - a polluted cloud appears brighter as seen from above.

- **Cloud lifetime effect** More but smaller cloud droplets are less likely to grow to precipitation size by collisions with other droplets, because their collision efficiency is lower than if larger droplets are present. Reduced precipitation may lead to an increased lifetime of a cloud which would enhance cloud reflectivity (Albrecht, 1989). Ferek et al. (2000) have observed drizzle suppression in stratus cloud regions polluted by ship tracks, going along with an increased cloud droplet concentration and a decreased droplet radius. However, Jiang et al. (2006) could not observe the same phenomenon for shallow cumulus clouds. They did not find an increased cloud lifetime for polluted clouds. As an explanation, they have proposed a competing effect of increased droplet evaporation of the smaller droplets in a polluted cloud.

- **Glaciation indirect effect** The subset of aerosol particles acting as IN can have an additional indirect effect. An increased concentration of anthropogenic IN leads to an increased freezing of supercooled cloud droplets. As ice crystals can efficiently grow to precipitation size (see next section), precipitation increases reducing the cloud lifetime and optical thickness (Lohmann, 2002).

- **Thermodynamic effect** With a two-dimensional cloud model, Khain et al. (2005) have found an increase of precipitation in polluted deep convective clouds. Suppression of raindrop formation and latent heat release from diffusional growth of small cloud droplets intensifies updraught velocities, leading to an increased amount of water available for freezing at higher altitudes. This again leads to an intensification of the updraught and can eventually lead to higher precipitation rates than in the clean case.

The interaction of all these indirect effects is complex since they partly counteract each other. Figure 1.1 visualizes this for the indirect aerosol effects on warm clouds (i. e. cloud albedo and cloud lifetime effect) and the glaciation indirect effect.
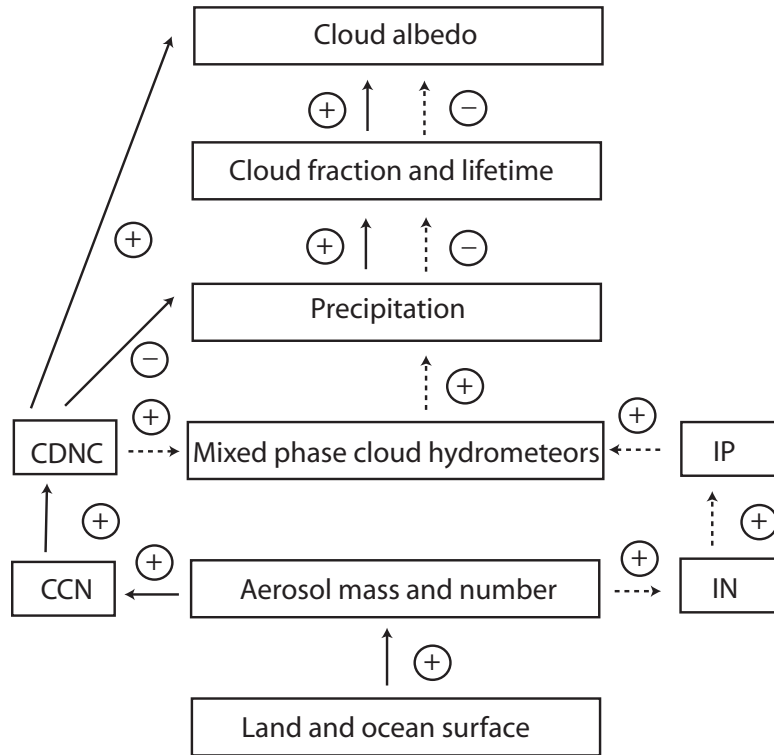
Figure 1.1: *Schematic diagram showing the interaction of the warm indirect aerosol effects (cloud albedo effect and cloud lifetime effect) and the glaciation indirect effect. Adapted from Lohmann (2002).*

An increased number of aerosol particles due to human activity both increases the number concentration of CCN and IN. Whereas an increased number of CCN has a negative effect on precipitation, an increased number of IN increases precipitation. Therefore, the glaciation indirect effect partly offsets the warm indirect aerosol effects. However, the level of scientific understanding of the total aerosol indirect effect is still very low, according to the IPCC Fourth Assessment Report (Denman et al., 2007). Due to insufficient knowledge about most indirect effects, only the cloud albedo effect has been taken into account by the IPCC Fourth Assessment Report in order to calculate the radiative forcing caused by the aerosol indirect effect between 1750 and 2005. A large errorbar still remains on both the direct and the indirect aerosol effects, as can be seen in Fig. 1.2.

The direct radiative forcing of anthropogenic aerosol has been estimated to be -0.5 ± 0.4 Wm^{-2}, whereas the indirect radiative forcing has been reported as -0.7 Wm^{-2}, with a 5 to 95% range of -0.3 to -1.8 Wm^{-2} (Forster et al., 2007).

1.3   Nucleation of Water Droplets and Ice Crystals

As discussed previously, the formation of ice in clouds influences cloud radiative properties and the formation of precipitation. Ice can nucleate in the presence of IN by heterogeneous nucleation, or without IN by homogeneous nucleation. In contrast, the formation of liquid cloud droplets always involves the presence of aerosol particles acting as CCN. In the following, the mechanisms of homogeneous and heterogeneous nucleation are discussed.

Radiative forcing of climate between 1750 and 2005
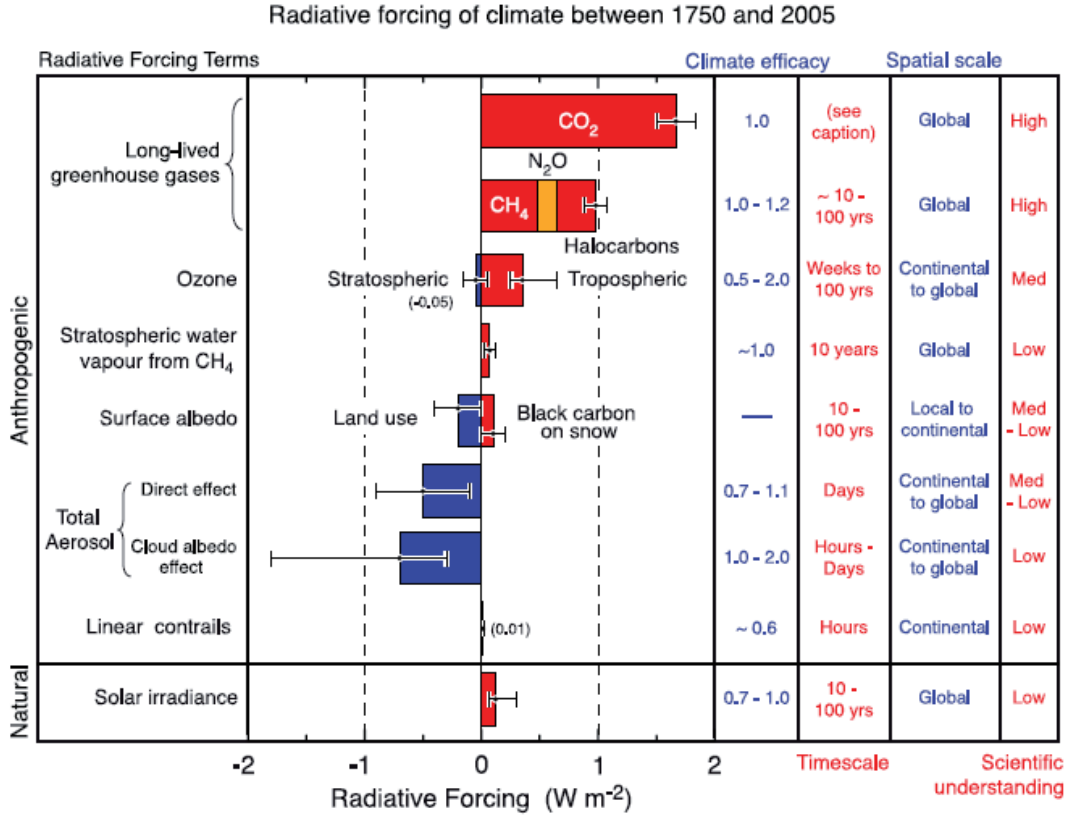
Figure 1.2: *Global radiative forcings between pre-industrial (1750) and present time, calculated by the IPCC Fourth Assessment Report. Adapted from Forster et al. (2007).*

1.3.1 Homogeneous Nucleation

Any nucleation process involves the formation of a new phase (e. g. solid ice) in the parent phase (e. g. liquid water). The new phase starts with a cluster of several molecules and can, under given circumstances, grow to macroscopic size or until the parent phase is completely transformed into the new phase. If the new phase is thermodynamically more stable than the parent phase, the transition to the new phase is energetically favourable. However, the formation of the new phase involves the formation of a new surface between the phases, which costs energy. This energy balance is schematically depicted in Fig. 1.3.

For homogeneous nucleation of ice in liquid water, the change in the Gibbs free energy due to the formation of a cluster with i molecules can be written as

$$\Delta G_i = (\mu_w(T) - \mu_i(T)) \cdot i + 4\pi r_i^2 \sigma_{i,w}(T), \tag{1.1}$$

where μ_w and μ_i are the chemical potentials of the water and the ice phase, r_i is the radius of the cluster, and $\sigma_{i,w}$ is the surface tension between the water and the ice phase (note that classical nucleation theory (CNT) assumes the surface tension of a small cluster to be the same as the one of the corresponding bulk material, which is actually a weakness of CNT). The difference in chemical potential between the two phases can be expressed as

$$\mu_w(T) - \mu_i(T) = -kT \ln\left(\frac{e_{sat,w}(T)}{e_{sat,i}(T)}\right), \tag{1.2}$$

where $e_{sat,w}(T)$ and $e_{sat,i}(T)$ are the vapour pressures over supercooled liquid water and over ice, re-
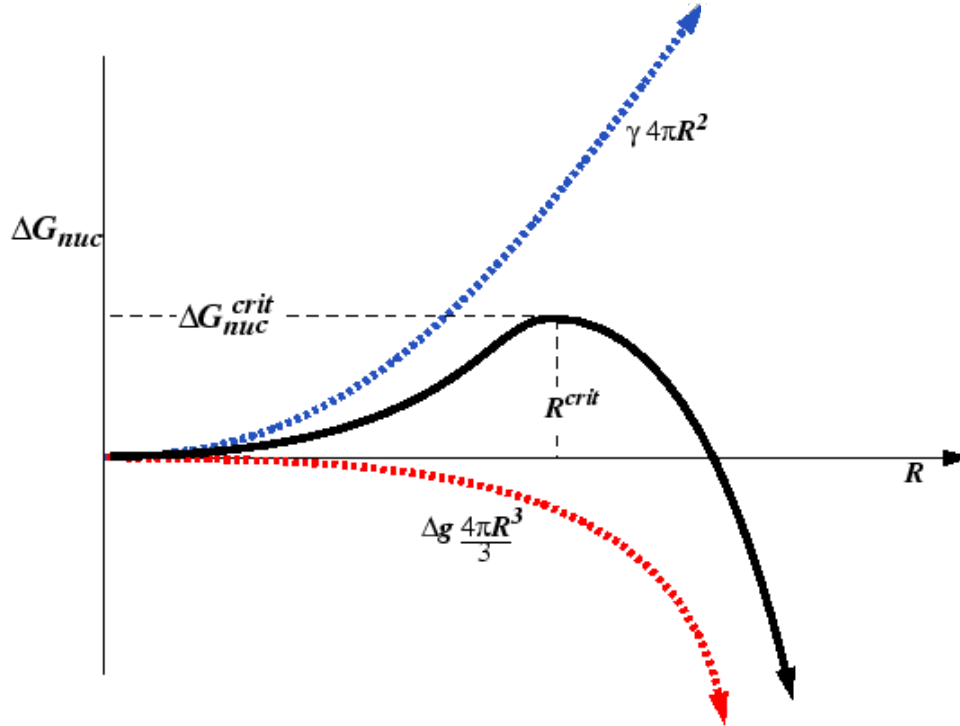
Figure 1.3: *Gibbs free energy for the formation of an embryo of the new phase within the parent phase as a function of embryo size. The blue curve represents the (positive) surface energy. The red curve represents the volume energy which is negative if the new phase is thermodynamically more stable than the parent phase. The sum of the two contributions shows the energy barrier of the nucleation process (black curve).*

spectively. The ratio between the two vapour pressures can be seen as a proxy for supercooling, since it increases linearly with decreasing temperature. Thus, the difference between the chemical potentials increases with decreasing temperature, which makes the phase transition more "attractive", i. e. more energetically favourable.

For small clusters, the surface energy term $4\pi r_i^2 \sigma$ dominates the energy balance. As the surface to volume ratio of the cluster decreases for increasing embryo size, the volume term dominates for larger embryo sizes. The result is an energy barrier ΔG which has to be overcome in each nucleation process. Fluctuations provide the energy required to grow the embryo to the critical radius r_{crit}. As these fluctuations are stochastic, they define nucleation as a stochastic process. Beyond r_{crit}, growth of the embryo is energetically favourable, and the embryo can grow spontaneously.

The rate at which nucleations, i. e. the formation of critical embryos, occur in the parent phase, depends on the height of the energy barrier, since

$$J \propto \exp\left(-\frac{\Delta G}{kT}\right), \tag{1.3}$$

where J is the nucleation rate, T is the temperature, and k Boltzmann's constant (Pruppacher and Klett, 1997). The height of the energy barrier depends on one hand on substance related quantities like the surface tension between the two phases, on the other hand it depends on the conditions in the parent phase, such as temperature and supersaturation. The higher the supersaturation in e. g. a vapour phase, the lower the energy barrier, and therefore the more likely the formation of a critical cluster of the liquid phase. Relating the critical radius r_{crit} to the supersaturation yields the Kelvin effect, which states that a larger saturation ratio is required for a smaller droplet or ice crystal to exist in equilibrium with the vapour phase (see section 2.4.5).

Whereas no further energy barrier has to be taken into account in the case of nucleation of an ice

crystal from the vapour phase, the formation of a critical ice embryo in liquid water is also limited by the diffusion energy across the water/ice interface. A formulation for the nucleation rate of critical ice embryos in liquid water taking both energy barriers into account can be found in Zobrist (2006).

Homogeneous nucleation can be important in the atmosphere, but only in the case of homogeneous nucleation of ice in water or solution droplets. For homogeneous nucleation of liquid water droplets or ice crystals from the vapour phase, the nucleation rate is far too small under atmospherically relevant conditions. At -12°C, a nucleation rate of $7 \times 10^{-2}\,\mathrm{cm}^{-3}\mathrm{s}^{-1}$ (still below $1\,\mathrm{cm}^{-3}\mathrm{s}^{-1}$, which is often used to define the onset of nucleation) would require a relative humidity around 500% (Pruppacher and Klett, 1997), whereas only a few percent above 100% are realistic in strong updraughts. Around 38°C of supercooling are required to obtain a significant amount of ice nucleation events in liquid water droplets on a time scale relevant to the atmosphere. This homogeneous freezing threshold has been confirmed by measurements (e. g. Rosenfeld and Woodley, 2000). In fact, it is not only determined by the atmospheric time scale, but also by the cloud droplet sizes in the atmosphere. As one can consider one nucleation event per droplet to be sufficient to freeze the entire droplet, and homogeneous nucleation is a stochastic process that can happen anywhere within the droplet, the freezing probability of a droplet is proportional to its volume. The freezing threshold of $-38\,°\mathrm{C}$ is therefore characteristic for cloud droplets which are in a size range from a few μm to a few hundred μm (e. g. Ferek et al., 2000). Homogeneous freezing of solution droplets is considered as an important ice nucleation mechanism primarily for initial ice formation in cirrus clouds in the upper troposphere (Heymsfield and Miloshevich, 1993).

1.3.2 Heterogeneous Nucleation

CCN Activation

Heterogeneous nucleation of cloud droplets is the only way of forming a liquid cloud, since nucleation rates for homogeneously condensing liquid droplets from the vapour phase are far too small to be relevant under atmospheric conditions. The term "cloud condensation nucleus" (CCN) is used for the fraction of an aerosol population that nucleates cloud droplets under atmospherically relevant conditions. These include supersaturations with respect to water below 10%, most often even below 1%. Fog mainly forms at supersaturations between 0.02% and 0.2% (Pruppacher and Klett, 1997). In the atmosphere, CCN concentrations vary from fewer than 100 cm^{-3} in remote marine regions to many thousand cm^{-3} in polluted urban areas (Seinfeld and Pandis, 2006). A simple way to obtain an estimate of the concentration N_{CCN} can be obtained with an empirical relation depending on the supersaturation S in %:

$$N_{\mathrm{CCN}} = C \cdot S^k, \tag{1.4}$$

where C and k are empirical constants depending on the air mass (Pruppacher and Klett, 1997).

The presence of soluble compounds in an aerosol particle is crucial for its activity as CCN. Since the equilibrium vapour pressure over an aqueous solution is lower than the one over pure water, the presence of a soluble compound in a droplet counteracts the Kelvin effect. Therefore, small solution droplets can exist in stable equilibrium with the vapour phase even at relative humidities below 100%. This equilibrium is described by Köhler theory and can be summarized by the relation

$$S = a_w \cdot \exp\left(\frac{2M_w \sigma_{s,v}}{RT \rho_w a}\right), \tag{1.5}$$

where S denotes the equilibrium saturation ratio for a solution droplet with radius a, M_w and ρ_w are the molar mass and the density of water, and $\sigma_{s,v}$ is the surface tension between the solution drop and the vapour phase (Pruppacher and Klett, 1997). The exponential term incorporates the Kelvin effect, whereas the water activity a_w accounts for the effect of the solute. a_w can qualitatively be regarded as a measure for the solute concentration in the drop, although it also accounts for non-ideality of the solution and therefore depends on the type of solute. For pure water, a_w takes the value 1, and decreases towards 0 for increasing solute concentration. Figure 1.4 shows the Köhler curve and the separate Kelvin and

solute effects for a solution drop containing a dry mass of 1×10^{-17} g of NaCl (corresponding to a NaCl particle with a dry radius of 10 nm).
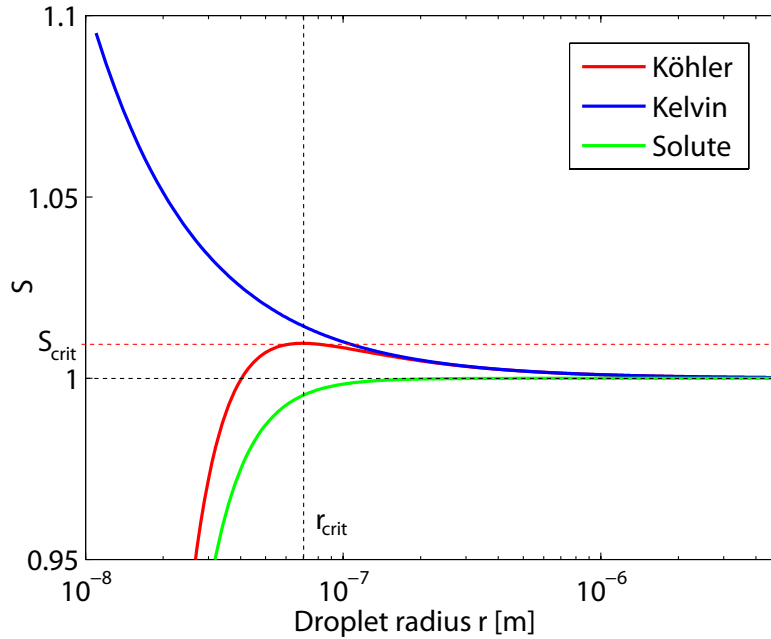
Figure 1.4: *Köhler curve for a NaCl particle of 10 nm radius (red curve). The green curve represents the solute effect reducing the equilibrium vapour pressure for increasing solute concentration, i. e. decreasing droplet radius. The blue curve represents the Kelvin effect increasing the equilibrium vapour pressure for decreasing droplet radius.*

The product of the Kelvin term and the solute term yields the Köhler curve which exhibits a maximum supersaturation S_{crit} at a droplet radius r_{crit}. S_{crit} and r_{crit} are determined by mass and type of the solute in the droplet. If $S > S_{crit}$ for a particle with a given soluble mass, the solution droplet can grow to its critical radius r_{crit}, and from there on spontaneously to macroscopic size, given enough water vapour is provided. In that case, the particle is activated as CCN. If $S < S_{crit}$, the particle cannot be activated as CCN, but remains as a small, concentrated haze particle on the ascending branch of the Köhler curve. Whereas a very small solute mass has been chosen in Fig. 1.4 to illustrate the Köhler curve, a typical solute mass of an atmospheric CCN leads to a value of S_{crit} below 1.01, i. e. internally mixed aerosol particles containing a certain amount of soluble mass are easily activated as CCN already at low updraught velocities.

If an aerosol particle does not contain any soluble mass, CCN activation is still possible, but requires more supersaturation. In this case, no S_{crit} can be defined above which a particle will definitely be activated as CCN, as there is no solute effect. For a given supersaturation, the Kelvin effect determines a critical radius that a water droplet condensing around the particle has to reach in order to exist in equilibrium with the vapour. This involves the transgression of an energy barrier (see section 1.3.1), a process which also depends on the time the particle is exposed to the supersaturation. Although the surface of an insoluble aerosol particle can considerably reduce this energy barrier compared to homogeneous nucleation of a water droplet (by the same mechanism as for ice nucleation, see below), the probability for CCN activation of a purely insoluble particle becomes significant only at considerably larger supersaturations than for internally mixed particles. Herich et al. (2009) and Koehler et al. (2009) have found significantly larger supersaturations required for CCN activation of particles with low hygroscopicity (i. e. containing a small amount of soluble mass) than for those with high hygroscopicity. Herich et al. (2009) have found that pure, dry-generated kaolinite clay particles with a diameter of 200 nm require a supersaturation around 0.7%, which is large compared to around 0.1% for pure $(NH_4)_2SO_4$ particles of the same size (Koehler et al., 2009).

Heterogeneous Ice Nucleation

Field measurements have shown that ice formation in clouds can occur at temperatures well above the onset of homogeneous freezing (e. g. Hobbs and Rangno, 1985) by heterogeneous nucleation on the surface of an insoluble IN. This means that for a given temperature, the nuleation rate J is increased by the presence of the IN via a reduction of the energy barrier ΔG. We illustrate this for the case of an ice embryo forming on a solid IN surrounded by liquid water. In CNT, the ice embryo is assumed to sit on the IN surface as a spherical cap, which is schematically shown in Fig. 1.5, assuming a planar IN surface.
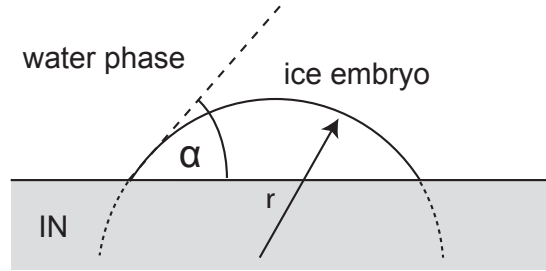
Figure 1.5: *Schematic illustration of an ice embryo forming on the surface of an IN. In classical nuceation theory, it is assumed to be a spherical cap with a contact angle α to the IN.*

The contact angle α between the IN and the ice embryo is defined by the three surface tensions of the ice-water interface, the ice-IN interface and the water-IN interface, respectively. In simple terms, it is an indicator how well the ice lattice matches the lattice of the solid IN. A good "compatibility" between the ice structure and the IN structure is reflected in a low contact angle α. The critical radius r_{crit} at which the embryo crosses the energy barrier does not depend on α, i. e. r_{crit} is the same for heterogeneous and homogeneous ice nucleation. This is not surprising as the curved surface of the ice embryo has to be in equilibrium with the liquid phase, like in the homogeneous case. However, the height of the energy barrier strongly depends on α. The smaller the contact angle, the less ice mass is required to form a cap with radius r_{crit}. It is important to note that r_{crit} defines the curvature of the ice-water interface, and not the volume of the ice embryo (which would be equivalent in the homogeneous case).

Both the surface energy term and the volume energy term in equation 1.1 are reduced compared to the homogeneous case. But since the surface term still dominates the energy balance for embryo sizes around r_{crit}, the reduction of the surface term is more important than the reduction of the volume term, and the height of the energy barrier decreases with decreasing α. In Fig. 1.6, the energy barrier has been calculated for the homogeneous case and for the heterogeneous case with $\alpha = 90°$C and $\alpha = 45°$C.

A contact angle of 45°C reduces the energy barrier by an order of magnitude, compared to the homogeneous case. In the framework of CNT, the heterogeneous energy barrier can be calculated from the homogeneous energy barrier by multiplication with a factor f:

$$\Delta G_{\text{het}} = \Delta G_{\text{hom}} \cdot f(m), \tag{1.6}$$

where $m = \cos(\alpha)$, and $f(m) = (2+m)(1-m)^2/4$ for a planar IN surface. If (more accurately) a curved IN substrate is assumed, geometrical considerations lead to a more complicated function $f(m)$ (Pruppacher and Klett, 1997).

1.3.3   Stochastic and Singular Hypothesis

Whereas these considerations visualize the effect of the presence of an IN on ice nucleation, one can raise the question how well an IN with a complex shape and surface structure can be represented by a
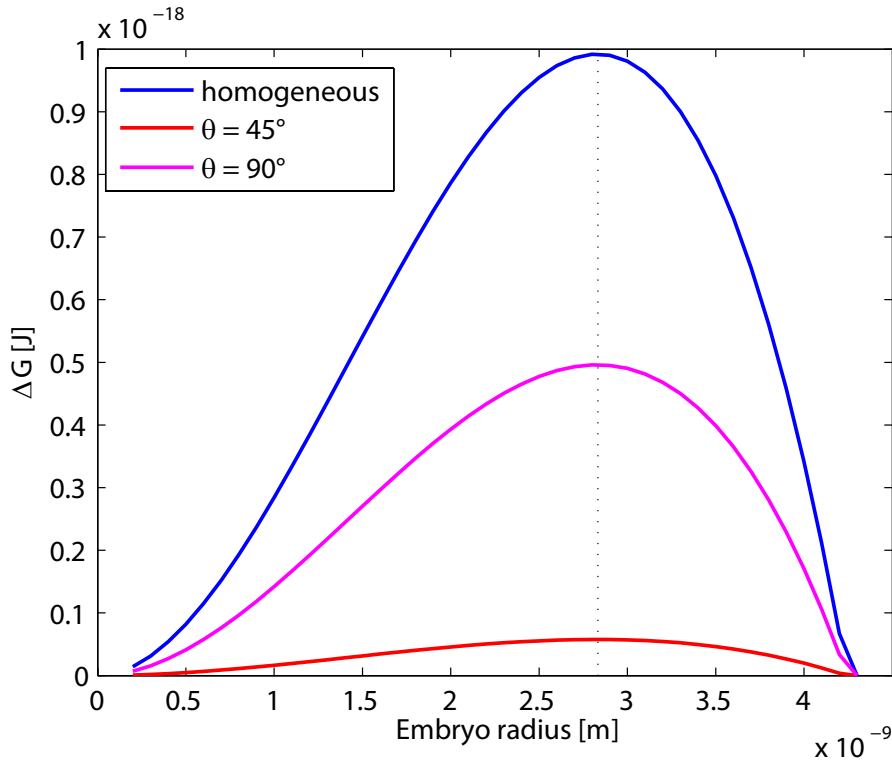
Figure 1.6: *Energy barrier to nucleation of ice in water at -20°C for the homogeneous and the heterogeneous case. The dashed vertical line indicates the critical radius r_{crit}.*

simple contact angle α. The question in what detail the IN surface has to enter a formulation of heterogeneous ice nucleation depends on the nature of the heterogeneous ice nucleation process. In fact, two controversial hypotheses were established about the nature of heterogeneous ice nucleation: The "stochastic hypothesis" assumes that in a sample of IN of the same kind, all IN have the same effect on ice nucleation, and therefore heterogeneous ice nucleation is a stochastic process like homogeneous ice nucleation, with an increased probability for the formation of a critical embryo compared to the homogeneous case. In other words, according to stochastic hypothesis, all embryos have an equal probability to reach critical size by random fluctuations, and individual differences between IN introduce negligible variations (Vali and Stansbury, 1966). This is schematically visualized in Fig. 1.7a for four hypothetical ice embryos: The average embryo sizes $\bar{r}_1$ to $\bar{r}_4$ are almost equal, and an embryo can reach the critical radius r_c by stochastic fluctuations.

On the other hand, the "singular hypothesis" states that each IN has a characteristic temperature T_c (or supersaturation) at which it causes nucleation. This is equivalent to the statement that the size of embryos (for a given temperature or supersaturation) is determined by the nucleating site on which they grow, whereas random fluctuations in their size are negligible (Vali and Stansbury, 1966). This is visualized in Fig. 1.7b: The average embryo size is defined by the corresponding nucleating site, and largely differs among the embryos. Compared to these differences, stochastic fluctuations are small. Thus, in the framework of the singular hypothesis, an IN inevitably nucleates ice if it carries at least one site that defines an ice embryo size larger than the critical radius at the specified temperature (or supersaturation). The singular hypothesis involves the assumption that ice embryos form on sites predestinated for ice nucleation. Such sites can be cracks, cavities, egdes and similar structures on the surface of an IN, which is rarely smooth and homogeneous (Pruppacher and Klett, 1997). In the past, several studies have adressed the question which hypothesis is suitable to describe heterogeneous ice nucleation (e. g. Vali and Stansbury, 1966; Vonnegut and Baldwin, 1984; Vali, 1994). According to Vali (1994), neither hy-
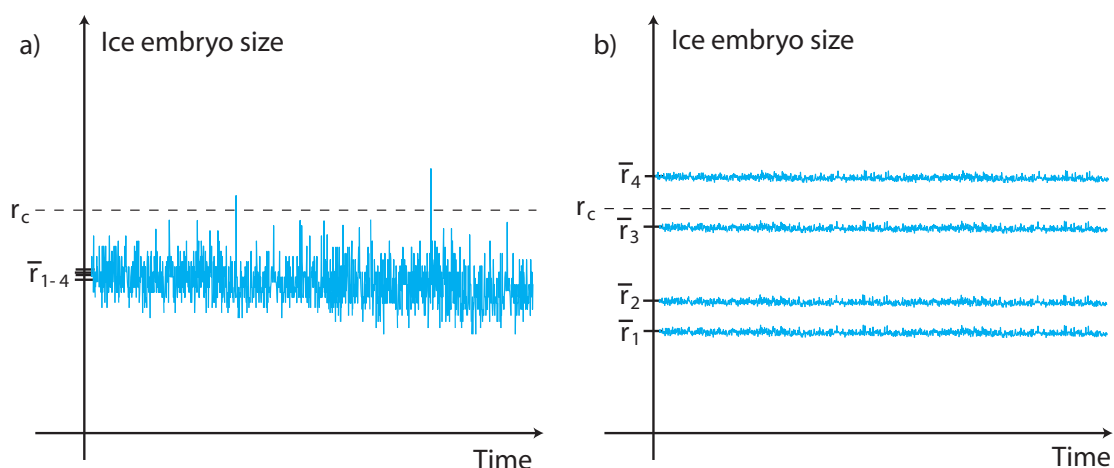
Figure 1.7: *Schematic visualization of the size of four hypothetic ice embryos as a function of time according to a) stochastic hypothesis, and b) singular hypothesis. The dashed lines indicate the critical radius for the given conditions (temperature or supersaturation).*

pothesis can describe heterogeneous ice nucleation alone. In his study, the relative freezing rate of water droplets (i. e. the number of freezing droplets per time interval divided by the total number of unfrozen droplets) with immersed impurities was observed to decrease approximately exponentially with time if the temperature was held constant. This contradicts the stochastic hypothesis which predicts the relative freezing rate to be constant with time, but it also contradicts the singular hypothesis predicting no freezing event without any change in temperature. Whereas the singular hypothesis can be taken as a good first approximation, small fluctuations in the freezing temperature of single droplets repeatedly brought to sufficiently large supercoolings have revealed the influence of stochastic fluctuations in embryo size (Vali, 2008).

A formulation of heterogeneous ice nucleation representing the stochastic hypothesis can be obtained with CNT (involving the concept of a nucleation rate J) in combination with a constant contact angle α for all IN in a sample. On the other hand, a deterministic approach as used in Connolly et al. (2009) can represent the singular hypothesis. A combination of the two hypotheses can be realized with CNT in combination with an appropriate function that distributes active sites of different quality over the IN surface, which can produce significant differences between individual IN (see Marcolli et al. (2007) and section 3.4 of the present work). In the terminology of CNT, active sites can be characterized by a local contact angle which is considerably lower than the average on the IN surface.

1.3.4 Mechanisms of Heterogeneous Ice Nucleation

Whereas a good knowledge exists about the properties of aerosol particles leading to a high efficiency of the particles to act as CCN, there is still a lack of understanding which properties determine the IN efficiency of aerosol particles (Szyrmer and Zawadzki, 1997). The fact that different modes of heterogeneous ice nucleation exist makes IN characterization difficult (Lohmann and Feichter, 2005; Deshler and Vali, 1992). Four modes are usually distinguished (Vali, 1985), which are schematically depicted in Fig. 1.8.

Deposition nucleation refers to ice nucleation by deposition of water molecules directly from the vapour phase which requires the vapour phase to be supersaturated with respect to ice, i. e. $S_i > 1$. For immersion freezing, a droplet with an immersed IN is cooled to a certain supercooling at which the IN initiates freezing of the droplet. The mechanism of condensation freezing refers to the case where at some supercooling, a cloud droplet nucleates on the IN and immediately freezes. This requires not only
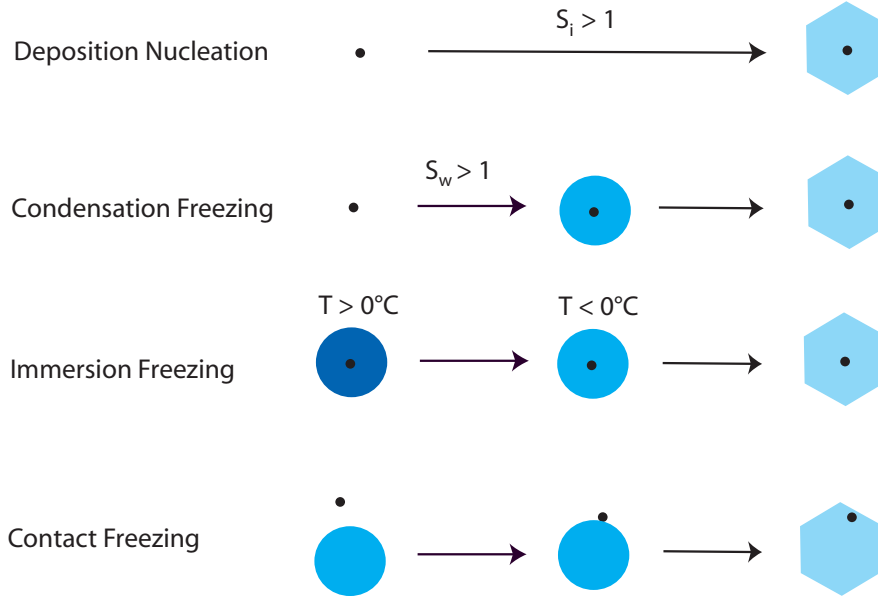
Figure 1.8: *Heterogeneous ice nucleation modes.*

sufficient supercooling, but also a relative humidity above water saturation, i. e. $S_w > 1$. This mechanism might be relevant in cases where a cloud-free air parcel at a temperature below 0°C starts to ascend and reaches the condensation level at a temperature where the IN are active. Immersion freezing, on the other hand, occurs in the case of a pre-existing cloud rising to a level at which the immersed IN freeze the droplets. It is still an open question if condensation nucleation is just a process combining CCN activation and subsequent immersion freezing, or not. If this is the case, then freezing temperatures are not expected to differ substantially for the two mechanisms. The fourth heterogeneous ice nucleation mechanism is termed contact nucleation and refers to the collision of a dry aerosol particle with a super-cooled cloud droplet which initiates droplet freezing.

Deposition nucleation is expected to be less efficient than freezing mechanisms for $S_w > 1$, since the critical radius and the energy barrier are larger for ice nucleation from the vapour than from the liquid phase (Cooper, 1974). However, experiments have shown that deposition nucleation is active at conditions relevant for the formation of cirrus clouds (e. g. DeMott et al., 2003b; Welti et al., 2009; Archuleta et al., 2005). Immersion and contact freezing can be considered as the dominant mechanisms for ice nucleation in mixed-phase clouds, as they involve preexisting liquid droplets. Laboratory experiments have revealed the contact mode to be active at substantially higher temperatures than the immersion mode (e. g. Pitter and Pruppacher, 1973; Diehl et al., 2002). Different reasons have been proposed for this: Fletcher (1970) suggested that nucleating sites on IN might be changed when the IN is immersed in water. Cooper (1974) proposed a mechanism for contact nucleation which involves the presence of a subcritical ice embryo (i. e. smaller than the critical radius) on the IN prior to the collision with a supercooled droplet. Although subcritical with respect to the vapour phase, this embryo can be super-critical with respect to the liquid phase, and therefore initiate freezing of the droplet. If this embryo consists of less ice mass than a critical embryo formed within the liquid phase from the beginning, then the probability for the droplet to freeze is larger in the contact mode than in the immersion mode for a given temperature. Although contact freezing is active at higher temperatures than immersion freezing, immersion freezing can be more prevalent at lower temperatures, since contact nucleation is limited by the collision efficiency between IN and cloud droplets (Lohmann and Feichter, 2005). As contact freezing requires the presence of a dry IN, it is most likely to take place in cloud regions associated with evaporation, e. g. due to downdraughts or mixing (Young, 1974).

Aging or cloud processing can change the activity of IN in the individual mechanisms. For example, soluble material condensed on the surface of an IN can make the IN unavailable for deposition nucleation

or contact freezing where a dry aerosol particle is required. On the other hand, the particle is then more readily activated as CCN and can act as an IN in the immersion mode.

1.3.5 Atmospheric IN

While a considerable fraction of atmospheric aerosol particles can act as CCN (cf. section 1.3.2), only a small fraction of them act as IN. Richardson et al. (2007) found IN concentrations between $1 \times 10^{-3}\,\mathrm{cm}^{-3}$ and $1 \times 10^{-2}\,\mathrm{cm}^{-3}$ in springtime aerosol at Storm Peak Laboratory, which is around 5 orders of magnitude less than the total aerosol concentration. Despite their scarcity, IN have a large influence on the formation of precipitation and the lifetime of clouds. Once ice crystals nucleate in a mixed-phase cloud, they grow at the expense of the surrounding water droplets via the Bergeron-Findeisen process, due to the difference in vapour pressure over water and ice. This diffusional growth leads to an increased terminal velocity of the ice crystals compared to the cloud droplets. Collisions with supercooled cloud droplets lead to further growth of the ice crystals until they eventually reach precipitation size and sediment out of the cloud. Chemical analysis of particles at the center of snow or ice crystals from inside a cloud gives information about what substances are important for atmospheric ice nucleation. Kumai (1961) found clay mineral particles at the center of 87% of around 300 investigated snow crystals. More recent studies by DeMott et al. (2003a) and Richardson et al. (2007) have confirmed the prevalence of mineral dust and metallic particles inside ice crystals, whereas the total aerosol mass was dominated by sulfates and organics in these studies. DeMott et al. (2003b) pointed out the importance of Saharan dust as ice nuclei in air masses over Florida, where very high IN concentrations exceeding $1\,\mathrm{cm}^{-3}$ were measured in a special situation. From laboratory experiments, biogenic particles such as bacteria (Levin and Yankofsky, 1983) or pollen (Diehl et al., 2002) are known to act as IN at temperatures only a few degrees below 0°C. Although biogenic particles are generally more efficient IN than e. g. mineral dust, their role in atmospheric ice formation is not fully understood. Due to their relatively large size (around 1 to 100 μm), their residence time in the atmosphere is limited, and their concentration strongly decreases with increasing altitude. In general, the size of aerosol particles has two counteracting effects on their relevance as atmospheric IN: On one hand, a large size goes along with a short residence time and a low probability for long-range transport. On the other hand, a larger surface area increases the probability for efficient nucleating sites present on the IN surface.

   Whereas mineral dust is a major natural contributor to atmospheric IN, its abundance can be increased by anthropogenic activity such as agriculture, which can lead to enhanced soil erosion. Further important anthropogenic IN can be metallic particles (Cziczo et al., 2009), and according to Gorbunov et al. (2001), soot from natural or anthropogenic origin can be a potent source of IN.

1.4   Laboratory Experiments on Ice Nucleation with Mineral Dust

Numerous laboratory studies have been performed to assess the ice nucleation properties of aerosol particles, in particular of mineral dust particles because of their dominant role in heterogeneous ice nucleation in the atmosphere. A variety of experimental techniques have been used to explore IN efficiencies of aerosol particles in the different heterogeneous nucleation mechanisms. A table summarizing the findings of numerous studies exploring a variety of different mineral dust species can be found in Zimmermann et al. (2008). In the following, the most widely used techniques are summarized along with examples.

- **Cold stage experiments** Both immersion freezing and deposition nucleation ability of IN have been investigated with this type of setup. The IN or water droplets with immersed IN are distributed on a hydrophobic surface in a chamber with a controlled atmosphere. Such chambers are often called static diffusion chambers. Kanji et al. (2008) successively increased RH_i in the chamber by reducing the cold stage temperature while the partial pressure of water vapour in the chamber

remained constant, and observed the onset of ice nucleation on the particles. Knopf and Koop (2006) regulated the partial pressure of water vapour by regulating the temperature of a water reservoir providing the water vapour. For ATD particles between 0.7 and 10 μm diameter, they found deposition nucleation to be the favoured pathway for ice formation below 240 K. Hoffer (1961) produced suspensions of mineral dust particles in pure water or a solution of mixed salts. Droplets around 100 μm diameter were placed in a silicone oil matrix, and freezing temperatures were recorded upon cooling the chamber. Median freezing temperatures of -32°C were reported for kaolinite in pure water, and around -24°C for illite and montmorillonite. Zuberi et al. (2002) investigated heterogeneous freezing of aqueous ammonium sulfate solution droplets with mineral dust immersions. 10 - 55 μm solution droplets with numerous mineral dust particles immersed in each droplets froze at around 10°C warmer temperatures than without mineral dust immersions. This result was found to be similar for kaolinite and montmorillonite.

- **CFDC Experiments** With continuous flow diffusion chambers (CFDC, see section 2.2), heterogeneous ice nucleation on airborne particles can be detected. This makes detection more elaborate compared to cold stage experiments, but the situation of airborne particles in the atmosphere is more closely represented. Particles travel through a zone which is supersaturated with respect to ice. At the end of the chamber, the fraction of particles that have nucleated ice is measured with an optical particle counter (OPC). Archuleta et al. (2005) found mineral dust surrogates of sizes between 50 nm and 200 nm to be strong potential contributors to the atmospheric IN population at temperatures relevant for cirrus formation. Welti et al. (2009) have investigated kaolinite, montmorillonite, illite and ATD particles between 100 nm and 800 nm at temperatures between -20°C and -55°C. They found deposition nucleation to be active below -35°C above saturations between $RH_i = 105\%$ and 110%, depending on the dust species and particle size. For warmer temperatures, ice nucleation only occurred above water saturation, suggesting that ice formed by condensation freezing rather than deposition nucleation. In general, RH_i required to activate particles decreased with increasing particle size, which is in agreement with the findings of Archuleta et al. (2005).

- **Expansion type chambers** A realistic simulation of a lifting air parcel forming a cloud can be achieved in expansion chambers by adiabatic expansion of the air volume. Supersaturation with respect to ice or water is a consequence of the adiabatic cooling and depends on the expansion rate. With the AIDA (Aerosol Interaction and Dynamics) facility, Möhler et al. (2006) investigated deposition nucleation of various natural dust species at cirrus cloud temperatures. Particle sizes were approximately lognormally distributed with mode diameters between 0.3 and 0.5 μm and standard deviations between 1.6 and 1.9. ATD particles were found to nucleate ice efficiently below $RH_i = 115\%$ between 209 K and 223 K, whereas Asian dust and Saharan dust showed a significantly lower fraction of active deposition nuclei. Connolly et al. (2009) performed AIDA experiments with the same dust samples as Möhler et al. (2006) above water saturation, in order to investigate immersion/condensation freezing of these particles. ATD was reported to be active in the freezing mode at temperatures below -24°C, whereas Asian and Saharan dust showed a lower freezing activity.

- **Flow tube experiments** Hung et al. (2003) studied immersion freezing of aqueous ammonium sulfate particles containing hematite or corundum mineral dust cores by aerosol flow tube infrared spectroscopy (AFT-IR). In a conditioning cell, the relative humidity of the sample air and thus the water activity of the solution droplets is defined. Upon entering the freezing cell, the temperature drops to a candidate freezing temperature, and the phase of a particle (i. e. liquid or ice) is recorded by infrared spectroscopy. Hung et al. (2003) reported more rapid ice nucleation with the presence of mineral cores, if their size exceeded a threshold diameter of ca. 50 nm. They observed an increasing nucleation rate for decreasing temperature, decreasing solute concentration and increasing particle diameter. During the measurement campaign FROST (FReezing Of duST), Niedermeier et al. (2009) performed freezing experiments with coated and uncoated ATD particles

with LACIS (Leipzig Aerosol Cloud Interaction Simulator). LACIS is a laminar flow tube consisting of seven sections with individual temperature control. The relative humidity profile inside LACIS is determined by the inlet dewpoint temperatures of sample and sheath air and by the wall temperatures. A temperature drop between two sections of LACIS leads to a water supersaturated region where aerosol particles form cloud droplets and can freeze upon further cooling. This method of activating particles as CCN and subsequent droplet freezing provides the possibility to investigate droplet freezing with single immersed particles. Niedermeier et al. (2009) concluded that immersion freezing was the predominant ice nucleation mechanism for the performed experiments. Deposition nucleation, although possible, proved to yield negligible amounts of ice crystals. For pure ATD particles with a diameter of 300 nm, ice fractions exceeding 1% were measured for temperatures below -32°C. Coating of the particles with various substances proved to decrease the IN activity of the ATD particles. As an explanation, possible surface modifications due to the coating was suggested.

A similar concept of generating a supersaturated region inside a chamber is used in FINCH (Fast Ice Nucleus CHamber, Bundke et al. (2008)), where particle-free, warm, humidified air is mixed with cold dry air in the inlet region. First measurements published by Bundke et al. (2008) with kaolinite test dust show a significant increase in the activated fraction of particles below -16.5°C and above 20% of ice supersaturation. No further indications are made about the particle size distribution and the mechanism by which the ice crystals nucleated.

- **Differential scanning calorimetry** Latent heat released from freezing droplets is used to detect ice nucleation in experiments with differential scanning calorimetry. An emulsion of small water droplets in an oil matrix is cooled down, and the required heat flow from the sample is measured and compared with the reference value for an oil matrix without droplets. Differences in the heat flows indicate latent heat release associated with freezing of droplets in the sample (Zuberi et al., 2001). Marcolli et al. (2007) used aqueous suspensions of ATD particles between 0 and 7 μm in diameter. The droplet size distributions could be fit with a normal distribution with a median diameter of 10 μm and a standard deviation of 14.8. Droplets with ATD immersions were found to freeze at temperatures higher than the homogeneous freezing temperature. Depending on the concentration of ATD in the droplets, freezing temperatures ranged from the homogeneous threshold to temperatures as high as 256 K.

- **Wind tunnel experiments** Pitter and Pruppacher (1973) performed experiments on immersion and contact freezing with aqueous suspensions of kaolinite and montmorillonite particles. Droplets as large as 300 μm in radius were stably suspended in a vertical airstream of controlled temperature and relative humidity. The size of the immersed mineral dust particles varied between 0.1 and 30 μm with a mode between 1 and 2 μm. An abrupt change in terminal velocity indicated the phase change of the droplets upon freezing. In the immersion mode, a median freezing temperature around -26°C was reported for kaolinite, and around -22°C for montmorillonite. Freezing temperatures were substantially higher in the contact mode: -12°C for kaolinite and -8°C for montmorillonite. More recently, the vertical wind tunnel technique was used e. g. by Diehl et al. (2002) to measure the ice nucleation ability of pollen.

1.5 Objectives of the Present Thesis

Knowledge about heterogeneous nucleation of ice in the atmosphere is crucial for our understanding of aerosol-cloud interactions and their impact on climate. Due to its complexity, a straightforward theoretical description of heterogeneous ice nucleation is not possible. To be able to describe heterogeneous ice nucleation adequately in modeling studies, laboratory experiments are required to investigate the ice nucleation capabilities of a large variety of potential IN species with various sizes, coatings etc. Ice nucleation properties of aerosol particles have been extensively studied with different experimental tech-

niques (see section 1.4). However, there is still a lack of understanding the properties of aerosol particles affecting their activity as IN. Results obtained with the same IN species often show considerable diversity among different experimental techniques. Often, results from different studies are difficult to compare due to differing experimental conditions (e. g. different particle or droplet sizes). It is also questionable if all conditions under which experiments have been carried out are atmospherically relevant. For example, as the droplet freezing temperature increases with increasing droplet volume for aqueous suspensions of particles, freezing temperatures obtained in wind tunnel studies might not fully represent atmospheric freezing temperatures. Also, a comprehensive study adressing the relative importance of the different heterogeneous ice nucleation mechanisms is still missing.

The aim of the present thesis has been the development of a new experimental apparatus capable of nucleating cloud droplets with single immersed aerosol particles and continuously cooling them to a potential freezing temperature prevailing in the Zurich Ice Nucleation Chamber (ZINC). The new IMCA chamber (Immersion Mode Cooling ChAmber) has been designed to investigate the ice nucleating activity of aerosol particles in the immersion mode under conditions relevant for mixed-phase clouds. As its way of immersing aerosol particles into droplets is similar to the atmospheric pathway of CCN activation prior to freezing, we expect to obtain freezing temperatures that are realistic for mixed-phase clouds. Among the experimental techniques discussed in section 1.4, the one used in LACIS has the most similarities to the concept of IMCA. IMCA and LACIS have been designed and constructed simultaneously. The motivation for the concept of IMCA as an extension to the existing ZINC chamber is to benefit from the advantage of a CFDC maintaining independently constant temperature and relative humidity. Freezing of droplets under constant conditions also provides the possibility to measure a time dependency of the freezing process.

Measurements of the frozen fraction of cloud droplets as a function of temperature for a certain IN species can be used to parameterize immersion freezing in modeling studies (e. g. Lohmann and Diehl, 2006; Diehl and Wurzler, 2004), e. g. to numerically investigate glaciation of mixed-phase clouds. Although it is known that particle size can play a role for the IN activity (e. g. Archuleta et al., 2005; Welti et al., 2009), models have not included size dependencies so far, due to a lack in experimental data sensitive to IN size (Lohmann and Diehl, 2006). With the measurement of size dependent IN efficiencies of aerosol particles in the immersion mode, experiments with IMCA, especially with mineral dust aerosols, aim at contributing to eliminate this lack of available data. An intermediate-term goal of our research group involving the present work is to compare IN efficiencies of the same aerosol species under equal conditions in different heterogeneous ice nucleation mechanisms and to obtain information on the relative importance of the different mechanisms.

Chapter 2 of this thesis discusses the theory of operation of the IMCA chamber, including computational fluid dynamics (CFD) simulations of the conditions inside the chamber and calculations of droplet evolution under these conditions. Chapter 3 presents the first experiments performed with IMCA on size selected mineral dust (kaolinite) particles, chapter 4 deals with the experimental setup in more detail, and chapter 5 summarizes the main findings of the present thesis.

Chapter 2

The IMCA Chamber - Theory of Operation

2.1   Overview of the Experimental Setup

The present experiments aim at investigating the ice nucleating ability of size selected mineral dust particles in the immersion mode. The experimental setup therefore generates a size selected aerosol, activates the aerosol particles into cloud droplets and subsequently cools the droplets down to freezing temperatures. This process of CCN activation and subsequent freezing of the droplet simulates the process that an IN acting in the immersion mode can experience in the atmosphere. A schematic of the experimental setup is shown in Fig. 2.1.

The main part of the experimental setup consists of the newly developed Immersion Mode Cooling Chamber (IMCA) and the Zurich Ice Nucleation Chamber (ZINC). The IMCA chamber has been built to
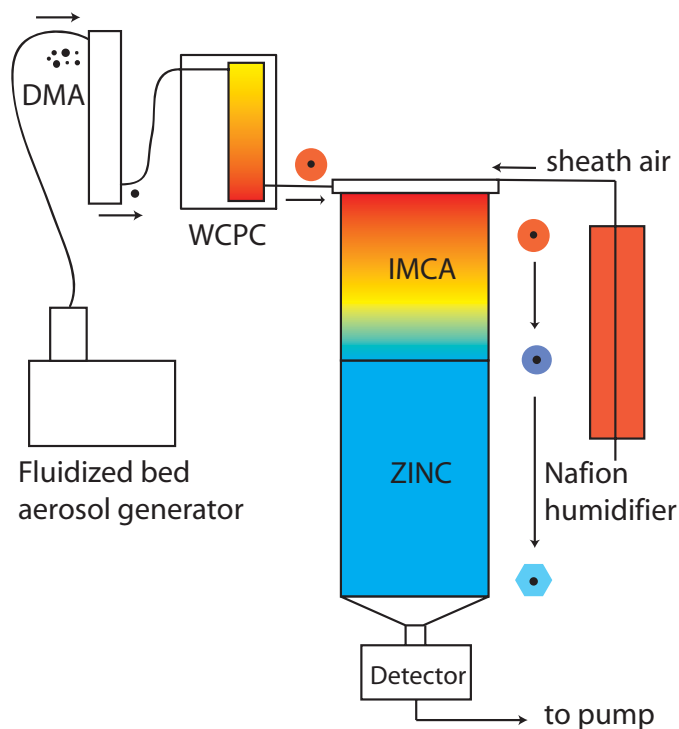
Figure 2.1: *Schematic of the experimental setup. Colours qualitatively indicate temperature from warm (red) to cold (blue)*

cool cloud droplets from room temperature to temperatures at which freezing of the droplets can occur. These temperatures are maintained within the ZINC chamber. CCN activation of the aerosol particles can be done in two different ways: Either with a modified water based condensation particle counter (WCPC), or directly in the IMCA chamber. The frozen fraction of the droplets can be measured with a depolarisation detector (IODE, Nicolet et al. (2007)) at the bottom of ZINC. Whereas ZINC is described in detail in Stetzer et al. (2008), the current chapter describes the theory of operation of the IMCA chamber in detail.

2.1.1 The IMCA Chamber

The IMCA chamber has been built as a vertical extension to the ZINC chamber which is a parallel plate continuous flow diffusion chamber (CFDC) based on the principle of Rogers (1988). IMCA has the same parallel plate geometry as ZINC and extends its length by 66 cm with the same chamber width of 30 cm. The plate distance, however, has been chosen to be 5 mm instead of 1 cm for reasons that will be discussed in section 2.5.3. A schematic of the IMCA chamber is shown in Fig. 2.2.
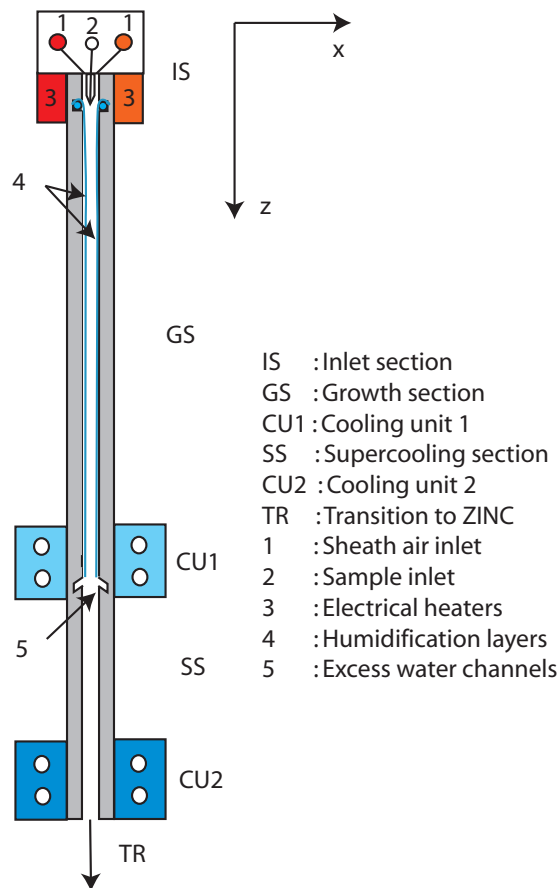
Figure 2.2: *Schematic side view of the IMCA chamber with the main sections and units for temperature and humidity control. Colours qualitatively represent temperatures.*

Continuous cooling of water droplets is achieved with a streamwise, vertical temperature gradient along the IMCA chamber walls. This temperature gradient is defined by three temperature control units: At the top of the chamber, two heating blocks with individual controls are implemented. The temperatures of the two cooling blocks at the lowest end of IMCA are defined by the wall temperatures of the ZINC chamber which allows for continuous cooling of the droplets to the experimental temperature. Maintenance of an appropriate humidity in the chamber requires water supply from a layer of humidified

filter paper on each of the walls. Humidity requirements are discussed in detail in section 2.5.3. In the lower part of IMCA, humidification of the walls is achieved with an ice layer. A third intermediate cooling unit is required to define the transition between the upper part with liquid water humidification from the lower part with ice coated walls. Accordingly, this intermediate cooling unit is kept at a temperature close to 273 K. Excess water channels prevent liquid water from reaching and freezing in the cold part of IMCA. The position of the intermediate cooling unit between top and bottom of IMCA leading to a steeper temperature gradient in the lower part has been chosen such that the supersaturated upper part is long enough to allow for sufficient droplet growth (see section 2.5.3). The aerosol flow of 0.6 lpm is combined with two humidified sheath air flows of 2.2 lpm each, leading to a total flow of 5 lpm. The inlet part is taken from the ZINC chamber and distributes the aerosol and sheath air flows over the chamber width with a blade. In the experiment, the lowest part of IMCA is directly mounted upstream of ZINC.

2.1.2 CCN Activation

As discussed in section 1.3.4, ice crystals can form via four different heterogeneous nucleation modes which in principle can all take place in an ice nucleation chamber at given temperature and relative humidity. Unambiguous separation of the immersion freezing mode from condensation freezing and deposition nucleation can only be achieved if no additional cloud droplets can nucleate at the experimental temperature, and if no dry, unactivated aerosol particles are exposed to conditions where deposition nucleation is active. The first requirement is relatively easy to meet. As long as the ZINC chamber is operated at a relative humidity slightly below water saturation, no cloud droplets can condense on insoluble, uncoated aerosol particles. Isolating the immersion mode from deposition nucleation, however, requires reliable CCN activation of the sample aerosol. The term "CCN activation" normally refers to activation under conditions prevailing in atmospheric clouds, where only a part of the aerosol particles really act as CCN. Activation of all aerosol particles, however, requires supersaturations considerably larger than the ones reached e. g. in CCN counters (Kumar et al., 2003). As water-based condensation particle counters (WCPC, Hering et al. (2005)) apply supersaturations sufficient to activate all aerosol particles within their specified size range, the present experimental setup includes a modified WCPC (TSI 3782) from which activated cloud droplets are injected into the IMCA chamber. Alternatively, the WCPC can be bypassed, and dry aerosol particles can directly be activated in the IMCA chamber if sufficient supersaturation is applied in the upper part of IMCA.

2.2 Saturation and Flow Profiles in CFDCs

2.2.1 Supersaturation Concepts

Various approaches have been followed in order to achieve supersaturation (with respect to water or ice) in cloud chambers (cf. section 1.4). In expansion type chambers like the Aerosol Interactions and Dynamics in the Atmosphere (AIDA) facility in Karlsruhe (Möhler et al., 2003), supersaturation is achieved by adiabatic expansion of an air volume. In mixing type chambers, merging of air flows with different temperatures and water mixing ratios leads to supersaturation (Bundke et al., 2008). In static diffusion chambers, a heated ice surface is used to provide the water vapour for supersaturation with respect to ice (Hussain and Saunders, 1984), whereas in continuous flow diffusion chambers (CFDCs), a supersaturation profile establishes between two ice layers at different temperatures (Rogers, 1988; Stetzer et al., 2008). The ZINC chamber has been constructed according to the CFDC principle in parallel-plate geometry. Keeping two parallel, ice coated walls with a distance d at different temperatures, T_w and T_c, leads to gradients in temperature and partial pressure of water vapour between the walls. Those gradients and the resulting profiles of temperature and supersaturation are derived in the following sections. The principle of generating supersaturation in IMCA is similar to the CFDC principle. Instead of an ice coating, the IMCA walls are humidified by wetted filter papers and set to different temperatures.

2.2.2 The CFDC Temperature Profile

For the temperature profile between the two walls, we invoke the continuity equation for the enthalpy of air,

$$\frac{\partial q}{\partial t} + \nabla \cdot \vec{j}_h = 0, \tag{2.1}$$

where q denotes the enthalpy of air per unit volume and $\vec{j}_h$ is the flux density vector for heat transport. In analogy to mass diffusion $\vec{j}_h$ is driven by a temperature gradient, i.e. $\vec{j}_h = -K\vec{\nabla}T$, where K is the thermal conductivity of humid air. Inserting $\vec{j}_h$ in equation (2.1) and reducing the problem to one dimension (i.e. the position between the walls x) leads to

$$\rho c_p \frac{\partial T}{\partial t} - \frac{\partial}{\partial x}\left(K(T(x))\frac{\partial T}{\partial x}\right) = 0, \tag{2.2}$$

where the identity $q = \rho c_p T$ has been used. For steady state operation of the CFDC with $\frac{\partial T}{\partial t} = 0$, this reduces to an ordinary differential equation,

$$K(T(x)) \cdot \frac{dT}{dx} = A, \tag{2.3}$$

where A is a constant that is determined by the boundary conditions. If the cold wall is at $x = 0$, and the warm wall at $x = d$, the boundary conditions are $T(x = 0) = T_c$ and $T(x = d) = T_w$. If the dependence of the heat conductivity K on temperature is negligible, then the solution of equation (2.3) is simply a linear temperature profile,

$$T(x) = T_c + C \cdot x, \tag{2.4}$$

where $C = \frac{T_w - T_c}{d}$. The temperature dependence of K infers negligible change to the linearity of the temperature profile: According to Pruppacher and Klett (1997), K can be parameterized as

$$K = B \cdot T(x) + C, \tag{2.5}$$

with $B = 7.11 \cdot 10^{-5}\,\mathrm{J\,m^{-1}\,s^{-1}\,K^{-2}}$ and $C = 2.38 \cdot 10^{-2}\,\mathrm{J\,m^{-1}\,s^{-1}\,K^{-1}}$. Substitution in equation (2.3) and integration leads to a temperature profile of the form

$$T(x) = \frac{1}{B}\left(\sqrt{2AB(x+D)} - C\right), \tag{2.6}$$

where B and C are determined by equation (2.5), and A and D are determined by the boundary conditions. For temperatures T_w and T_c of interest, the temperature profile according to equation (2.6) differs by less than 0.1% from the linear profile. Thus, K can be considered as independent from T, and the temperature profile is given by equation (2.4) in the following.

2.2.3 The CFDC Supersaturation Profile

On each of the ice coated walls, the partial pressure of water vapour e in the air is equal to the saturation vapour pressure with respect to ice, $e_{sat,i}$, at the corresponding temperature. Since $e_{sat,i}$ increases with increasing temperature, the concentration of water molecules in the air close to the warm wall is higher than the one close to the cold wall. In order to find the steady state supersaturation profile in the CFDC, the diffusion equation for the mass density of water molecules ρ has to be solved for appropriate boundary conditions. Although the relative humidity RH is calculated from e according to

$$RH_i = \frac{e(T)}{e_{sat,i}(T)} \tag{2.7}$$

rather than from ρ, the diffusion equation cannot be directly applied to e since it is only applicable to mass or number densities. The water vapour pressure e, however, depends on temperature and therefore

does not necessarily obey the continuity equation which is the basic principle of the diffusion equation. Nevertheless, the method of applying the diffusion equation to e has been used in the characterization of CFDCs and is explicitly described in Rogers (1988). The calculation of e from ρ can be done via the ideal gas law

$$eV = NRT, \tag{2.8}$$

where in the present case N is the number of moles of water molecules in volume V, R is the universal gas constant, and T denotes the temperature. The mass density of water vapour ρ can be introduced via $N = \frac{\rho V}{M_w}$, where M_w stands for the molar mass of water. Replacing N in equation (2.8) leads to the desired conversion between ρ and e,

$$e(x) = \frac{\rho(x)RT(x)}{M_w}. \tag{2.9}$$

The diffusion equation for ρ can be written as

$$\frac{\partial \rho}{\partial t} = \frac{\partial}{\partial x}\left(D(T(x))\frac{\partial \rho}{\partial x}\right), \tag{2.10}$$

where D is the diffusivity of water vapour in air. For steady state conditions, this reduces to

$$D(T(x))\frac{\partial \rho}{\partial x} = \widetilde{A} \tag{2.11}$$

where the constant $\widetilde{A}$ has to be determined from the boundary conditions. Considering D as independent from temperature would lead to a linear water vapour density profile in the CFDC similar to the temperature profile. In contrast to the weak temperature dependency of the thermal conductivity K, however, the temperature dependency of D is close to quadratic. According to Pruppacher and Klett (1997), D (in $m^2\,s^{-1}$) can be parameterised as

$$D = 2.11 \times 10^{-5}\left(\frac{T}{T_0}\right)^{1.94}\left(\frac{p_0}{p}\right), \tag{2.12}$$

where p is the total pressure, $T_0 = 273.15$ K and $p_0 = 1013.25$ hPa. As p is constant and does not significantly differ from p_0 in a the present experiments, the second bracket in equation (2.12) can be omitted. Also, for simplicity the exponent is assumed to be 2 instead of 1.94 at first, i.e.

$$D = \widetilde{D_0}\cdot\left(\frac{T}{T_0}\right)^2 =: D_0 \cdot T^2, \tag{2.13}$$

where $\widetilde{D_0} = 2.11 \cdot 10^{-5}\,m^2\,s^{-1}$ and $D_0 = \frac{\widetilde{D_0}}{T_0}$. Substituting equations (2.13) and (2.4) into (2.11) leads to an ordinary differential equation for ρ:

$$\frac{d\rho}{dx} = \frac{\widetilde{A}}{D_0(T_c + Cx)^2} \tag{2.14}$$

which can be solved by separation of variables, leading to

$$\rho(x) = \rho_0 - \frac{\widetilde{A}}{D_0 C}\left(\frac{1}{T_c + Cx} - \frac{1}{T_c}\right). \tag{2.15}$$

$\widetilde{A}$ and ρ_0 can be determined with the boundary conditions $\rho(x = 0) = \rho_c$ and $\rho(x = d) = \rho_w$, where $\rho_c = \frac{e_{sat,i}(T_c)M_w}{RT_c}$ and $\rho_w = \frac{e_{sat,i}(T_w)M_w}{RT_w}$. The result is

$$\rho(x) = \rho_c + \frac{T_c T_w}{Cd}(\rho_c - \rho_w)\left(\frac{1}{T_c + Cx} - \frac{1}{T_c}\right). \tag{2.16}$$

21

Substituting this expression into equation (2.9) to find the profile of water vapour pressure across the CFDC leads to the simple result of a linear profile after some algebraic rearrangement,

$$e(x) = e_{sat,i}(T_c) + \frac{e_{sat,i}(T_w) - e_{sat,i}(T_c)}{d} \cdot x. \tag{2.17}$$

The fact that this is analytically the same result that one obtains by simultaneously applying the diffusion equation to e and neglecting any temperature dependence of the diffusion coefficient D is a coincidence due to the assumption of steady state conditions and to the simplification of a quadratic temperature dependence of D. Setting this simplification aside and solving the problem with an exponent of 1.94 in equation (2.13) leads to a negligible change in the profile of e. The linear profile can therefore be considered a good approximation for steady state conditions in a CFDC. Results for the water vapour pressure and supersaturation profiles obtained with equation (2.17) are shown in Fig. 2.3.
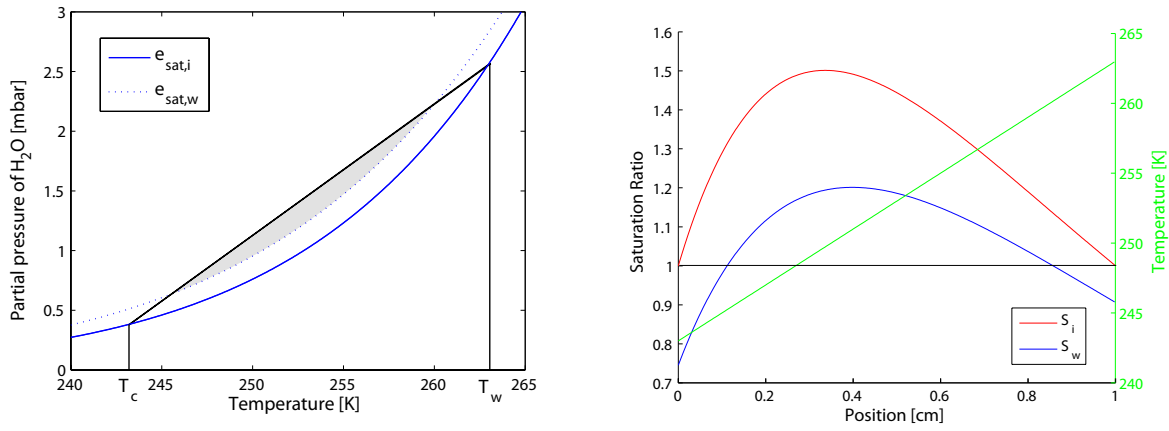
Figure 2.3: *a) Linear water vapour pressure profile for steady state in a CFDC. The black line denotes the actual partial pressure $e(T)$ of H_2O between two ice coated walls at $T_c = 243$ K and $T_w = 263$ K with a distance of 1 cm. The blue lines show the saturation vapour pressure with respect to ice and water. The grey shaded area indicates supersaturation with respect to liquid water. b) Profiles of saturation ratio with respect to water and ice based on the profile of $e(T)$ in a). The colder wall is at position 0 cm, the warmer wall at 1 cm.*

The entire chamber is supersaturated with respect to ice as soon as there is any temperature difference. For the chosen wall temperatures of $T_c = 243$ K and $T_w = 263$ K, a considerable part of the chamber is also supersaturated with respect to water. The temperature dependent saturation vapour pressures with respect to water and ice have been calculated according to Murphy and Koop (2005).

2.2.4 Flow Profiles and Sample Position

While the steady state flow establishing between two isothermal parallel walls can be described with a laminar profile, the flow profile between two parallel walls at different temperatures is a superposition between the laminar profile and a buoyant flow profile as described by Rogers (1988) and Sinnarwalla and Alofs (1973). The buoyant flow originates from the gradient in air density between the warmer and the colder wall and can have a considerable effect on the total flow profile, depending on the temperature difference ΔT and the distance d of the walls. An example flow profile realistic for the ZINC chamber with $T_w = 263$ K, $T_c = 243$ K and $d = 1$ cm is shown in Fig. 2.4 for a total flow of 10 lpm as used in a standard ZINC experiment, and 5 lpm as used in experiments with IMCA coupled to ZINC.

It is obvious that a wall temperature difference of $dT = 20$ K infers a significant deviation from the purely laminar flow profile. The main part of the flow down the CFDC is shifted towards the colder wall,
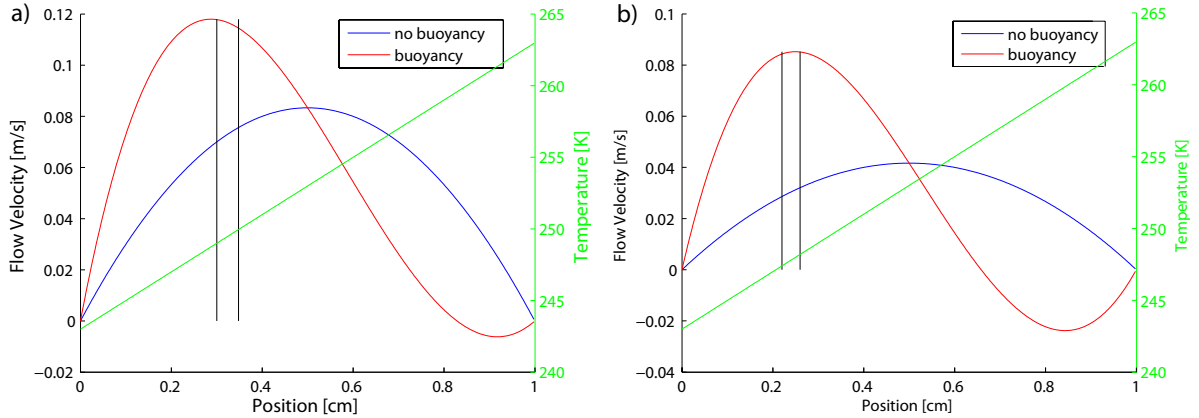
Figure 2.4: *Calculated flow profiles with and without the effect of buoyancy in a CFDC configuration realistic for the ZINC chamber at a total flow rate of a) 10 lpm, and b) 5 lpm as used in experiments with IMCA coupled to ZINC. The black vertical lines delimit the sample area which is embedded in two sheath air flows. The sample flow rate is 1 lpm in a), and 0.6 lpm in b).*

whereas a backflow layer establishes at the warmer wall. This effect is stronger for a lower total flow rate. The black vertical lines in Fig. 2.4 delimit the area over which the sample air extends between the two sheath air flows for a configuration with 1 lpm of sample air in the case of 10 lpm total flow, and 0.6 lpm of sample air in the case of 5 lpm total flow. Figures 2.3b and 2.4 show that the sample flow is close to the position where the maximum ice supersaturation is reached in the chamber.

2.2.5 IMCA - A Special Case of CFDC

Whereas CFDCs are used to nucleate ice crystals at constant temperature and supersaturation, the IMCA chamber is actually a mixture between a CCN counter and a CFDC. Cloud droplet nucleation or droplet growth (in the case of CCN activation by the WCPC) in the top of IMCA and subsequent cooling of the droplets without excessive evaporation requires both a temperature gradient in $x-$direction and a streamwise temperature gradient in $z-$direction (cf. Fig. 2.2). The saturation conditions establishing in the IMCA chamber are complicated and will be adressed in section 2.5. The flow profile also varies along the $z-$direction. The influence of buoyancy is strongest at the top of IMCA where the temperature difference between the walls dT usually is largest (see section 2.5). An example flow profile for the top part for $d = 0.5$ cm, $T_w = 323$ K and $T_c = 303$ K is shown in Fig. 2.5a.

Instead of a total flow rate of 10 lpm, IMCA only uses 5 lpm made up of twice 2.2 lpm sheath flow and 0.6 lpm sample flow. The reason for a lower total flow rate in IMCA is discussed in section 2.5.3. Although the temperature difference ΔT is equal to the one in Fig. 2.4, the laminar flow is influenced by the buoyant flow to a much lower extent in the IMCA chamber. This is primarily due to the smaller distance d of the walls. The sample flow layer is only shifted slightly towards the colder wall such that it is a good approximation to assume that it is in the center between the walls. Figure 2.5b shows the corresponding supersaturation profile for the top part of IMCA. For IMCA, not all of the sample flow can be expected to be precisely at the position of maximum supersaturation, and the variability in supersaturation within the sample flow is between 0.5% and 1% *RH* typically. This can be considered an upper limit estimate since temperature difference and thus also supersaturation and buoyant flow are maximum in the top part of IMCA.
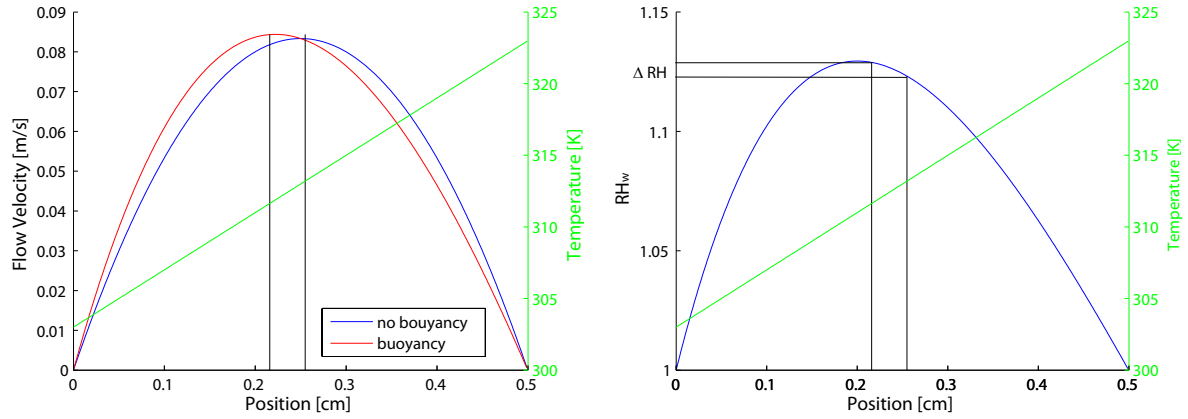
Figure 2.5: *a) Calculated laminar (blue) and total (red) flow profile in the top part of the IMCA chamber for a wall distance of $d = 0.5$ cm and top wall temperatures of $T_w = 323$ K and $T_c = 303$ K. The sample flow of 0.6 lpm is embedded in two sheath air flows of 2.2 lpm each. The black vertical lines delimit the area of the sample flow. b) Profile of saturation ratio with respect to water in the top part of IMCA.*

2.3 CFD Simulations with FLUENT

2.3.1 The Purpose of Simulations

Designing a chamber to nucleate and grow cloud droplets and to cool them continuously by more than 60 K without losing them due to evaporation requires precise knowledge of the temperature and relative humidity conditions in the chamber. In order to test the suitability of the IMCA geometry, computational fluid dynamics (CFD) simulations were carried out with the commercially available software FLUENT (FLUENT, 2005). The main requirements for the IMCA design are:

- In order to have a controlled cooling of the sample in IMCA, the streamwise temperature gradient in $z-$direction and the flow velocity should be adjusted such that the central sample air temperature at one vertical position z corresponds to the average of the wall temperatures at the same position.

- The length of the lower part of IMCA (below 273 K, cf. section 2.1.1) has to allow for controlled cooling of the sample to the ZINC temperature on one hand. On the other hand, the lower relative humidity in the iced part is a limiting factor for the length of this part of IMCA due to droplet evaporation.

- The relative humidity and the length of the upper part of IMCA (above 273 K) have to be sufficient to nucleate and/or grow cloud droplets large enough that they are not lost due to evaporation in the lower part of IMCA or in ZINC.

Besides geometry considerations, CFD simulations help to find an appropriate set of experimental parameters (e. g. temperature and flow settings) and to understand the effect of a change of these parameters. Especially a change in the profile of relative humidity can significantly change the droplet evolution in the chamber. Furthermore, erroneous use of the setup can be prevented by prior simulation. Diffusional growth and evaporation of droplets are calculated separately based on temperature and relative humidity profiles from FLUENT simulations, but droplets are not included in the FLUENT model. The calculation of droplet evolution will be explained in detail in section 2.5.3. In the following, the FLUENT model used for these simulations is described, whereas simulation results are presented in section 2.5.

2.3.2 Reduction to 2 Dimensions

Both 3D and 2D simulations have been performed. The cross section of the IMCA geometry (as seen in Fig. 2.2) is invariant under translation in y-direction in the model. In reality, the sample flow does not enter into the chamber over the entire y-range of 30 cm, but only over 27 cm to prevent aerosol particles from getting close to the sidewalls of the chamber where the flow velocity is lower. It is assumed that the simplification of translational symmetry of the $x - z$ cross section leads to negligible errors in the simulation results. Furthermore, the volume of fluid in IMCA extends over 30 cm in y-direction, but only 0.5 cm in x-direction. Thus, the influence of the sidewalls located at $y = -15$ cm and $y = 15$ cm on the flow pattern in the center of the chamber is only minor. This together with the aforementioned symmetry consideration justifies the attempt to reduce the model from 3D to 2D. Comparison of the 3D and the 2D models shows no significant differences except from the flow velocity which is systematically higher by around 4% in the 3D model. This is expected since the no-slip condition at the IMCA sidewalls decelerates the flow close to the sidewalls in the 3D model. Since no sidewalls exist in the 2D model, an equal total flow rate leads to a slightly increased flow velocity far from the sidewalls in the 3D model. However, the effect of this difference on the droplet evolution is smaller than errors inferred by some inevitable idealizations in the models compared to reality. Hence, it is reasonable to use a 2D FLUENT model for the IMCA geometry.

2.3.3 Model Description

All simulations have been carried out with version 6.2.16 of FLUENT. The segregated solver, which solves the equations for the three spatial impulse components separately, is used. The coupled solver which solves coupled impulse equations is not required for the present low-velocity flow. In order to account for potential turbulence, a standard, widely-used $k - \varepsilon$ scheme is applied. This scheme has some limitations for flows with strong separation, large streamline curvature and large pressure gradients (FLUENT, 2005). As the flow in IMCA does not exhibit any of these characteristics, use of the $k - \varepsilon$ scheme is reasonable. Also, turbulence is not expected to be of considerable importance as the Reynolds number for the flow in IMCA can be estimated as

$$Re = \frac{\rho v d}{\eta} = 27.5$$

with a flow velocity $v = 0.1 \mathrm{m\,s}^{-1}$, a chamber width $d = 5 \times 10^{-3}$ m, an air density of 1 kg m^{-3} and a dynamic viscosity of 1.8×10^{-5} Pa s. In general, an internal flow is considered to be turbulent if the Reynolds number is above 2300. Furthermore, species transport is enabled in order to calculate the diffusion of water vapour in the sample air, and gravitational force in negative z-direction is enabled to account for potential buoyant flow.

Setting up a FLUENT simulation basically consists of three steps:

- Building a virtual geometry with the "Geometry And Mesh Building Intelligent Toolkit", (GAMBIT)

- Generating a mesh of finite elements for the geometry and defining boundaries (e. g. wall, velocity inlet, pressure outlet) and zones (e. g. fluid, solid),

- Importing the mesh in FLUENT, defining boundary conditions and material properties, and calculating a stationary solution for the flow with the solver.

In order to resolve the gradients in flow velocity near the walls of the fluid zone while keeping the number of grid cells as low as possible, small cell sizes have been used especially at the boundary of the fluid zone, while a coarser mesh was used in the solid zone. This zone is less sensitive as only heat
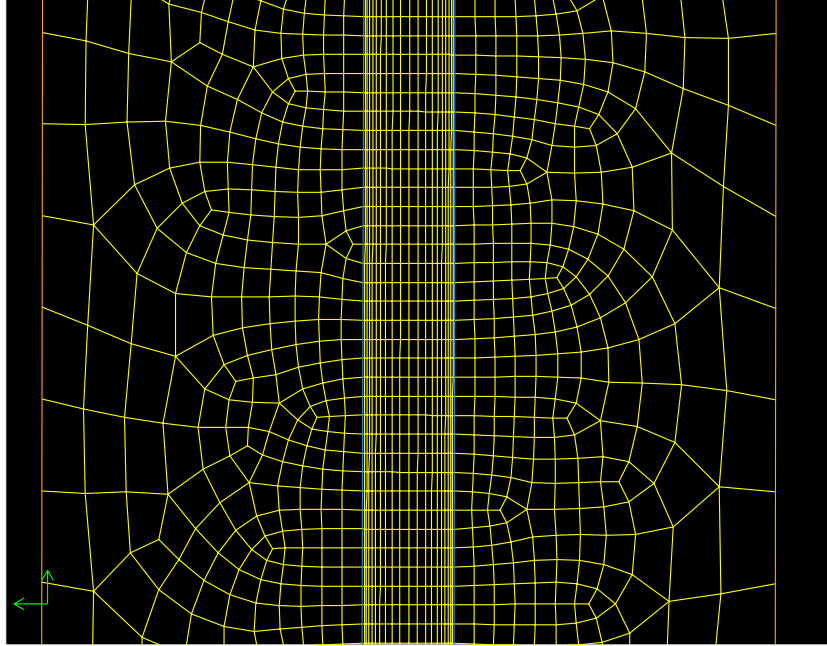
Figure 2.6: *Example section of the 2D GAMBIT mesh used for the IMCA geometry. Cell sizes in the central flow zone are small, especially close to the walls, in order to resolve the laminar (or close to laminar) flow profile. Cell sizes in the surrounding solid zones can be larger since only heat conduction takes place.*

conduction takes place which does not involve large gradients in the present case. An example of the 2D mesh is shown in Fig. 2.6.

As IMCA covers a large temperature range from around 238 K to 313 K, it is essential to define all parameters of material properties in FLUENT in a correct way. For a multicomponent flow involving more than one chemical species in the same volume, this is done in two steps. First, the way to derive a material property of the mixture from the same property of the individual species is defined. Then, the property of the individual species is defined, involving e. g. temperature dependencies. Direct temperature dependencies of properties like density ρ or viscosity η can be considerable, but also the mass fraction of water vapour in humid air depends strongly on temperature and influences the material properties.

The solid zone in the model consists of all aluminum parts delimiting the fluid zone. The fluid zone is filled with a mixture of air and water vapour. Whereas density ρ, heat capacity c_p and thermal conductivity κ of aluminum are considered constant with the default values given by FLUENT, the scheme how to calculate the physical properties of the fluid mixture has to be specified (FLUENT, 2005).

Mixture Properties

- **Density:** The density of the mixture between air and water vapour is calculated with the incompressible ideal gas law. The density is calculated according to

$$\rho = \frac{p_{op}}{RT \sum_i \frac{m_i}{M_i}}, \tag{2.18}$$

where p_{op} is the operating pressure (i. e. standard atmospheric pressure in the present case, $p_{op} = 1.013 \times 10^5$ Pa), m_i is the mass fraction of species i, and M_i is the molar mass of species i. Using the ideal gas law for a compressible fluid would replace p_{op} by $p_{op} + p$ in equation (2.18), where p is the pressure relative to the operating pressure. However, in the present case it is a good

approximation to assume an incompressible fluid since p is of the order of a few Pa maximum in the whole fluid zone for the present simulations.

- **Heat capacity:** The heat capacity of the mixture is calculated according to a mixing-law which computes the mixture's heat capacity as a mass fraction average of the pure species heat capacities:

$$c_p = \sum_i m_i c_{p,i} \tag{2.19}$$

The individual heat capacities of air and water vapour are defined as polynomial functions of temperature: A polynomial fit to data on the heat capacity of water vapour (Toolbox, 2005b) yields $c_{p,v}(T) = 1883.78 - 0.4424\,T + 1.469 \times 10^{-3}\,T^2 - 6.264 \times 10^{-7}\,T^3$ in $\mathrm{Jkg^{-1}\,K^{-1}}$ for T between 175 K and 1000 K. For air, the corresponding polynomial fit is $c_{p,a}(T) = 1027.3 - 0.1364\,T + 9.073 \times 10^{-5}\,T^2 + 4.007 \times 10^{-7}\,T^3$ in $\mathrm{Jkg^{-1}\,K^{-1}}$ for T between 173 K and 473 K (data from Toolbox (2005a)).

- **Thermal conductivity:** For the thermal conductivity K of the mixture an external user-defined function (UDF) is used based on the formulation in Pruppacher and Klett (1997):

$$K = K_a \left[1 - (\gamma_1 - \gamma_2 K_v/K_a) x_v \right], \tag{2.20}$$

where the temperature dependent thermal conductivities of air and water vapour are $K_a = 0.0238 + 7.11 \times 10^{-5}\,T$ and $K_v = 0.0158 + 8.36 \times 10^{-5}\,T$ in $\mathrm{Jm^{-1}\,s^{-1}\,K^{-1}}$ and the constants $\gamma_1 = 1.17$ and $\gamma_2 = 1.02$. x_v is the mole fraction of water vapour in the mixture which can be computed from the water vapour mass fraction α_m by

$$x_v = -\frac{\alpha_m M_a}{M_w \alpha_m - M_w - \alpha_m M_a}, \tag{2.21}$$

where $M_a \simeq 0.029\ \mathrm{kg\,mole^{-1}}$ is the molar mass of air, and M_w is the molar mass of water. Equation (2.21) is practical since the mass fraction of a species is directly accessible in a FLUENT case.

- **Viscosity:** A mass-weighted mixing-law similar to equation (2.19) is used for the viscosity η of the mixture. A polynomial fit to data on the viscosity of air (Toolbox, 2005a) yields $\eta_a(T) = 0.888 \times 10^{-6} + 6.926 \times 10^{-8}\,T - 3.492 \times 10^{-11}\,T^2$ in Pa s for T between 173 K and 473 K. Data on the viscosity of water vapour are available in Lide (2008) for Temperatures between 373 K and 673 K. The temperature dependence is close to linear in this range, and the same linear dependence is assumed for the temperatures of interest. The corresponding polynomial fit is $\eta_v(T) = -1.887 \times 10^{-6} + 3.861 \times 10^{-8}\,T$ in Pa s.

- **Diffusivity:** In the dilute approximation scheme, the mass diffusion flux of a chemical species in a mixture is calculated according to Fick's law,

$$J_i = -\rho D_{i,m} \frac{\partial m_i}{\partial x_i}, \tag{2.22}$$

where m_i is the mass fraction of species i, and $D_{i,m}$ is the diffusion coefficient of species i in the mixture. This relation is strictly valid when $D_{i,m}$ is independent of composition, i. e. the mixture composition does not change. This is a good approximation if the mass fraction m_i of a species is much smaller than 1. As the mass fraction of H_2O in air does not exceed values around 6×10^{-2} in the IMCA chamber, it is reasonable to use the dilute approximation for the diffusion of water vapour in air. The temperature dependence of the corresponding diffusion coefficient is given in equation 2.12 for $p = p_0$, which can be written in polynomial form, $D_v(T) = -6.25 \times 10^{-7} + 9.232 \times 10^{-9}\,T + 2.574 \times 10^{-10}\,T^2$ in $\mathrm{m^2\,s^{-1}}$ for temperatures between 233 K and 313 K.

The humidification of the chamber walls is modeled by setting the mass fraction α_m of H_2O in the air to the value corresponding to the saturation vapour pressure $e_{sat,w}$ or $e_{sat,i}$ at the chamber walls. As α_m depends on temperature and has to be calculated for every grid cell, a user-defined function relating $e_{sat,w}$ and $e_{sat,i}$ to the temperature has to be defined on the chamber walls. This UDF is based on the formulas by Murphy and Koop (2005).

2.4   Diffusional Growth and Evaporation of Water Droplets

As mentioned in section 2.3, the main requirement that the IMCA chamber has to meet is to cool cloud droplets without losing them due to evaporation. It is therefore important to know how the temperature and relative humidity conditions in the chamber affect the cloud droplet radius as the droplet travels through the chamber. In this section, the mathematical treatment of diffusional growth and evaporation and its implementation based on humidity and temperature profiles obtained with the FLUENT model are adressed. For the derivation of the governing equations, we follow the approach presented in Pruppacher and Klett (1997).

2.4.1   Governing Equations

Diffusion of water molecules is driven by their spatial gradient in mass or number density, according to Fick's law (see equation (2.22)). For diffusional growth or evaporation of a water droplet, the gradient in water vapour mass density right at the droplet surface is crucial. In order to be able to calculate this gradient, the field of water vapour mass density (in the following referred to as vapour density) in the air surrounding the droplet has to be found. This problem is similar to the one of an electrostatic potential in the presence of a charge distribution and can be described by the Laplace equation,

$$\nabla^2 \rho_v = 0, \tag{2.23}$$

where ρ_v is the water vapour density. For a single spherical droplet with radius a, the problem has radial symmetry and equation (2.23) can be written in spherical coordinates, where $r = 0$ is the center of the droplet:

$$\frac{d^2\rho_v}{dr^2} + \frac{2}{r}\frac{d\rho_v}{dr} = 0. \tag{2.24}$$

Two boundary conditions have to be formulated: Right at the droplet surface, ρ_v is determined by the saturation vapour pressure $e_{a,w}$ over a water surface with curvature a, i. e. $\rho_v(r = a) = \rho_a$ where $\rho_a = \frac{e_{a,w}M_w}{RT}$ (cf. equation (2.9)). For large droplets, the vapour pressure over the curved droplet surface can be approximated by the one over a flat surface, i. e. $e_{a,w} \simeq e_{sat,w}$, whereas for small radii a the Kelvin effect has to be taken into account. Far away from the droplet, ρ_v corresponds to the relative humidity S of the surrounding air, i. e. $\rho_v(r \to \infty) = \rho_\infty$ where $\rho_\infty = S \cdot \frac{e_{sat,w}M_w}{RT}$. With these boundary conditions, the solution for equation (2.24) is

$$\rho_v(r) = \rho_\infty + (\rho_a - \rho_\infty)\frac{a}{r}. \tag{2.25}$$

The mass flux $(j_v)_{r=a}$ of water molecules to or from the droplet surface can then be written as

$$(j_v)_{r=a} = -D_v\left(\frac{d\rho_v}{dr}\right)_{r=a} = \frac{D_v(\rho_a - \rho_\infty)}{a}. \tag{2.26}$$

The interesting quantity for the calculation of the droplet evolution is the increase or decrease of mass or radius of the droplet per unit time. This can easily be obtained by integrating j_v over the droplet surface, i.e.

$$\frac{dm}{dt} = -\int_S (j_v)_{r=a}\,dS = 4\pi a D_v(\rho_\infty - \rho_a). \tag{2.27}$$

With the ideal gas law, vapour mass concentrations can be substituted by the corresponding vapour pressure (cf. equation (2.9)), i.e.

$$\frac{dm}{dt} = \frac{4\pi a D_v M_w}{R}\left(\frac{e_\infty}{T_\infty} - \frac{e_a}{T_a}\right), \tag{2.28}$$

where M_w is the molar mass of water and R is the universal gas constant. With $\frac{dm}{dt} = 4\pi\rho_w a^2 \frac{da}{dt}$ with the liquid water density ρ_w, this can be formulated as a differential equation for the droplet radius a,

$$a\frac{da}{dt} = \frac{D_v M_w}{R\rho_w}\left(\frac{e_\infty}{T_\infty} - \frac{e_a}{T_a}\right). \tag{2.29}$$

As the droplet temperature T_a depends on the evaporation rate of the droplet and on the exchange of heat with the surrounding air, the transport of heat from or to the droplet has to be calculated simultaneously, giving two coupled differential equations for a and T_a. This can be illustrated by assuming a growing droplet: The larger dm/dt in equation (2.28) is, the higher T_a gets due to latent heat release upon condensation. A higher T_a increases the term in brackets which increases dm/dt further. Without considering the exchange of heat with the surrounding air, the rate of mass increase dm/dt would therefore not be determined by the droplet radius a alone, but would have an explicit time dependence which would be a contradiction. Instead, an increased T_a leads to a larger temperature gradient between the droplet surface and the surrounding air which increases the transport of heat from the droplet to the surrounding. Thus, T_a is in equilibrium between latent heat release and heat transport.

For the heat transport between a droplet and the surrounding air, equation (2.2) can be used as a starting point. For steady state and a thermal conductivity not depending on the spatial coordinate x, this reduces to the Laplace equation,

$$\nabla^2 T = 0, \tag{2.30}$$

with the boundary conditions $T(r = a) = T_a$ and $T(r \to \infty) = T_\infty$. The assumption of a constant heat conductivity K is justified because on one hand, the temperature dependence of K is weak (cf. section 2.2.2), and on the other hand, the temperature difference between the droplet and the surrounding air does not exceed a few Kelvin for saturation ratios of interest. In analogy to the determination of the water vapour density field, the temperature field is then given by

$$T(r) = T_\infty + (T_a - T_\infty)\frac{a}{r}. \tag{2.31}$$

Similar to the derivation of equation (2.28), integration of the heat flux density vector over the droplet surface yields the amount of heat transported to or from the droplet per unit time. With $j_h = -K\nabla T$, one obtains

$$\frac{dq}{dt} = 4\pi a K (T_\infty - T_a). \tag{2.32}$$

Note that K is the thermal conductivity of humid air which can be calculated according to equations (2.20) and (2.21).

2.4.2 Modifications Due to Gas Kinetics

The description of diffusional growth and evaporation is valid as long as one can assume that the water vapour density in the air is continuous up to the drop surface. This assumption is not justified for droplets with radii comparable to the mean free path λ of air molecules. It is reasonable to assume that the diffusion equation is only valid for distances larger than the "vapour jump length" $\Delta_v \simeq \lambda_{air}$ from the droplet surface (Fuchs, 1934). For $a < r < a + \Delta_v$, the concept of a concentration gradient is not applicable anymore. The transport of water molecules in this layer has to be described by gas kinetics. The approach in Pruppacher and Klett (1997) is followed to obtain the modifications of equations (2.28), (2.29) and (2.32) due to gas kinetics. The condensation flux of water vapour mass per unit area, i. e. the flux entering the droplet surface from within the layer, can be estimated as

$$j^\downarrow = \frac{\alpha_c \bar{v}_v \rho_v (r = a + \Delta_v)}{4}, \tag{2.33}$$

where $\bar{v}_v = \sqrt{\frac{8kT}{\pi\dot{m}}}$ is the mean molecular speed in a Maxwell-Boltzmann gas, ρ_v is the mass density of water vapour just outside the layer, $\dot{m}$ is the molecular mass of a H_2O molecule, and α_c is the condensation coefficient. α_c describes the fraction of water molecules that are actually retained by the droplet

surface when they come in contact with the surface. In a similar way, the evaporation flux, i. e. the flux leaving the droplet surface, can be written as

$$j^\uparrow = \frac{\alpha_e \bar{v}_v \rho_{v,sat}(T_a)}{4}, \tag{2.34}$$

where α_e is the evaporation coefficient which is assumed to be equal to α_c, and $\rho_{v,sat}(T_a)$ is the mass density of water vapour directly at the droplet surface with temperature T_a. The net flux to the droplet surface is then given by

$$J_v(r=a) = 4\pi a^2 \cdot (j^\downarrow - j^\uparrow) = \pi a^2 \alpha_c \bar{v}_v [\rho_{v,sat}(T_a) - \rho_v(a+\Delta_v)]. \tag{2.35}$$

Since continuity requires $J_v(r=a) = J_v(r=a+\Delta_v)$ for steady state, the right side of equation (2.35) must be equal to the flux described by Fick's law at the outer boundary of the layer:

$$J_v(r=a+\Delta_v) = -4\pi a^2 D_v \left(\frac{\partial \rho_v}{\partial r}\right)_{r=a+\Delta_v}. \tag{2.36}$$

The identity of (2.35) and (2.36) can be solved for $D_v \left(\frac{\partial \rho_v}{\partial r}\right)_{r=a+\Delta_v}$ with the result

$$D_v \left(\frac{\partial \rho_v}{\partial r}\right)_{r=a+\Delta_v} = D_v^* \frac{\rho_{v,sat}(T_a) - \rho_{v,\infty}}{a} = D_v^* \left(\frac{\partial \rho_v}{\partial r}\right)_{r=a}. \tag{2.37}$$

As $J_v(r=a) = -D_v \left(\frac{\partial \rho_v}{\partial r}\right)_{r=a+\Delta_v}$, the description of diffusional growth and evaporation accounting for gas kinetic effects at the droplet surface can be reduced to the description given in equation (2.28) and (2.29) with a modified diffusivity D_v^*:

$$D_v^* = \frac{D_v}{\left[\frac{a}{a+\Delta_v} + \frac{D_v}{a\alpha_c}\sqrt{\frac{2\pi M_w}{RT_a}}\right]}. \tag{2.38}$$

With similar arguments, gas kinetic effects can be accounted for in heat conduction via a modified form of the thermal conductivity of air, K_a:

$$K_a^* = \frac{K_a}{\left[\frac{a}{a+\Delta_T} + \frac{K_a}{a\alpha_T \rho c_{pa}}\sqrt{\frac{2\pi M_w}{RT_a}}\right]}, \tag{2.39}$$

where Δ_T is analogous to Δ_v and is assumed to be equal to the mean free path of air molecules λ_{air}, c_{pa} is the specific heat of air, and α_T is the thermal accommodation coefficient. Alty and Mackay (1935) have found α_T to be equal to 1, and Winkler et al. (2006) have excluded values below 0.85. It is therefore reasonable to assume $\alpha_T \simeq 1$ meaning that the vapour molecules coming into contact with the droplet surface are in thermal equilibrium with the surface. For the condensation coefficient α_c, a vast range of values between 0.01 and 1 have been reported in the past (Pruppacher and Klett, 1997). More recent studies where α_c was determined by quantitative comparison between calculated and measured growth of water droplets have reported values close to 1: Winkler et al. (2006) excluded values lower than 0.8 between 250 K and 270 K, whereas at higher temperatures up to 290 K, values lower than 0.4 could be excluded. Voigtlander et al. (2007) found α_c to be close to 1 at supersaturations representative for lower atmospheric conditions. They suggest that a value of $\alpha_c = 1$ should be used in cloud modeling. Hence, $\alpha_c = 1$ is assumed in the present calculations.

2.4.3 Implementation with IDL

An IDL routine is used for a numerical solution of the coupled differential equations for the droplet radius a and the droplet temperature T_a as a function of time. In each time step Δt, the mass change of

the droplet, $\Delta m = \frac{dm}{dt} \cdot \Delta t$ due to evaporation or condensation is calculated according to equation (2.28). From the new droplet mass, $m_{i+1} = m_i + \Delta m$, the new droplet radius a_{i+1} is calculated. The change in internal energy U of the droplet is a balance between the latent heat released due to condensation or evaporation and the heat exchanged with the surrounding air:

$$\frac{dU}{dt} = L_e \cdot \frac{dm}{dt} + \frac{dq}{dt}, \tag{2.40}$$

where L_e is the latent heat of evaporation of water, and dq/dt is calculated according to equation (2.32). In one timestep, the change of internal energy is $\Delta U = L_e \Delta m + \Delta q$. The change in droplet temperature can then be obtained via the relation

$$\Delta T_a = \frac{\Delta U}{m_{i+1} c_p}, \tag{2.41}$$

where c_p is the specific heat capacity of water. The droplet temperature is updated according to $T_{a,i+1} = T_{a,i} + \Delta T_a \cdot \Delta t$. As heat conduction is fast in the droplet (Fukuta and Walter, 1970), temperature differences between the droplet surface and the interior of the droplet can be neglected. Some care has to be taken defining the time step Δt. As small droplets grow or evaporate faster than larger ones at the same conditions, various time steps can be required within the same calculation. In the present routine, a mechanism has been implemented to automatically adapt the time step size to the current situation. For evaporating drops, the time step is reduced by a factor of five as soon as the decrease in mass Δm in one time step exceeds a fraction of 1×10^{-5} of the total droplet mass. This fraction could be optimized for shorter computational time, however, as computational time is not an important limitation in this case, priority has been given to a time step small enough that the result of the calculation is insensitive to variations in the time step. For an increasing droplet radius, the time step size is increased by a factor of 1.05 as soon as the mass increase per time step is less than a fraction of 1×10^{-6} of the total droplet mass. As the immersion freezing activity of coated aerosol particles might be investigated in future experiments, Koehler theory is included in the IDL routine in order to be able to simulate the evolution of a solution droplet in the IMCA chamber. The water vapour pressure right on the droplet surface, e_a, is then given by

$$e_a = e_{sat,w} \cdot a_w \left(\frac{2 M_w \sigma}{R T \rho_w a} \right), \tag{2.42}$$

where σ is the surface tension of the droplet surrounded by air, and a_w is the water activity of the droplet. Whereas the term in brackets in equation (2.42) represents the Kelvin effect, i. e. an increasing equilibrium vapour pressure over an increasingly curved surface, a_w incorporates the solute effect (or Raoult's effect) which reduces the equilibrium vapour pressure above the surface of a solution compared to pure water. For ideal solutions, the solute effect would be determined by the concentration of the solute alone. For non-ideal solutions, the water activity a_w accounts for the nature of the solute and the degree of non-ideality of the solution (Koop et al., 2000). a_w can be written as

$$a_w = \exp \left(-\nu \frac{m_s M_w}{m_w M_s} \Phi_s \right), \tag{2.43}$$

where ν denotes the number of ions a salt molecule dissociates into, m_s and m_w are the total masses of the solute and water in the solution, and M_w and M_s are the molar masses of the solute and water, respectively. Φ_s is the molal osmotic coefficient which indicates the degree of non-ideality of the solution. For concentration of interest in the present work, Φ_s takes values close to unity (i. e. the solution is close to ideal).

Parameter Settings

- The heat capacity of liquid water as a function of temperature is derived by linear interpolation of two sets of data. The CRC Handbook of Chemistry and Physics (Lide, 2008) provides data on c_p for temperatures above 273 K, while Angell et al. (1982) provide c_p for supercooled liquid water down to 236 K.

- The surface tension of a water surface surrounded by air as used in equation (2.42) is calculated as a linear function of temperature according to Pruppacher and Klett (1997).

- For the temperature dependent latent heat of evaporation, the linear function proposed by Pruppacher and Klett (1997) is used for temperatures above 273 K, whereas tabulated data from Rogers and Yau (1996) are interpolated at temperatures below 273 K.

- The density of water is interpolated from two data sets: For temperatures above 273 K, data are provided by the Engineering Toolbox (Toolbox, 2005c), whereas data on the density of supercooled water can be found in Hare and Sorensen (1987).

- The diffusivity D_v^* of H_2O vapour in air is calculated according to equation (2.38) taking gas kinetic effects into account. For D_v as a function of temperature and pressure, equation (2.12) is used.

- The equilibrium water vapour pressure above a flat water surface $e_{sat,w}$ is calculated according to Murphy and Koop (2005).

- The thermal conductance of humid air K_a^* is calculated according to equation (2.39) with the assumptions that $\Delta_T = \lambda_{air}$ and $\alpha_T = 1$. The uncorrected thermal conductance K_a of humid air is calculated using equation (2.20).

- The specific heat capacity of air is almost independent from temperature for temperatures of interest and is therefore taken as a constant, $c_{p,a} = 1.004 \text{ kJ kg}^{-1} \text{ K}^{-1}$.

- The air density depends on temperature and pressure and is calculated according to the ideal gas law.

- The mean free path of air λ_{air} used in the calculations of D_v^* and K_a^* can be written as

$$\lambda_{air} = \frac{2\eta_a}{p\sqrt{\frac{8M_a}{\pi RT}}}\,, \tag{2.44}$$

(Seinfeld and Pandis, 2006) p is the pressure, M_a the molar mass of air, and η_a the dynamic viscosity of air which can be parameterized as (Rogers and Yau, 1996)

$$\eta_a(T) = 1.72 \times 10^{-5} \left(\frac{393}{T + 120} \right) \left(\frac{T}{273} \right)^{3/2} \tag{2.45}$$

in $\text{Pa}\,\text{s}$.

Data sets for some of the above mentioned parameters can be viewed in Appendix A.

2.4.4 Validation of the Calculation

Some test calculations have been performed to compare the calculated droplet evolution with results from literature. Droplet growth has been calculated for two different solution droplets with different initial radii. A $(NH_4)_2SO_4$ particle with a dry mass of 1×10^{-15} kg and a NaCl particle with a dry mass of 1×10^{-13} kg exposed to 1% supersaturation at 293 K have been calculated during 8 seconds. The initial droplet radius corresponds to the equilibrium size of the corresponding salt solution at its deliquescence relative humidity (DRH) according to Köhler theory, i. e. 800 nm in radius for the $(NH_4)_2SO_4$ solution droplet (DRH = 82%), and 4μm for the NaCl droplet (DRH = 75%). The resulting droplet evolution is shown in Fig. 2.7.

Although in the present IDL calculation a condensation coefficient $\alpha_c = 1$ is taken, Fig. 2.7a shows curves for both $\alpha_c = 1$ and $\alpha_c = 0.045$, since Pruppacher and Klett (1997) assume α_c to be 0.045. One
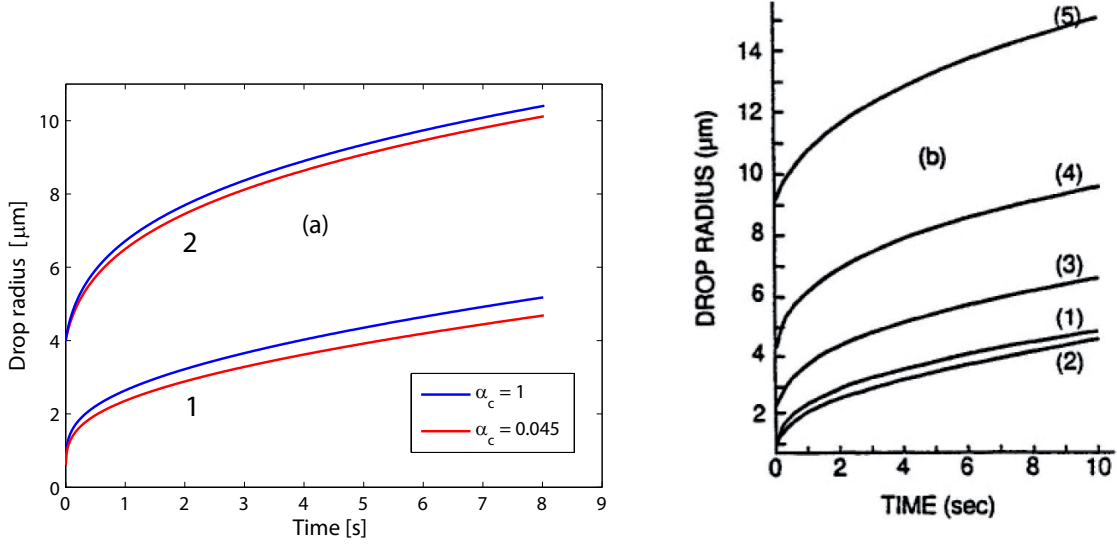
Figure 2.7: *Droplet growth at 1% supersaturation at 293 K. a) Present calculation for a small* $(NH_4)_2SO_4$ *solution droplet (labeled "1", dry mass* $1 \times 10^{-15} kg$*) and a larger NaCl droplet (labeled "2", dry mass* $1 \times 10^{-13} kg$*). Blue curves correspond to a condensation coefficient* $\alpha_c = 1$*, red curves to* $\alpha_c = 0.045$*. b) Droplet evolution from Pruppacher and Klett (1997) for different salt solution and dry masses. Curve (2) corresponds to the* $(NH_4)_2SO_4$ *particle in a), and curve (4) to the NaCl particle. The authors assume* $\alpha_c = 0.045$*.*

can see that the curves of the present calculation for $\alpha_c = 0.045$ are in reasonable agreement with curves (2) and (4) in Fig. 2.7b. As expected, the effect of a variation in α_c is larger for smaller droplets.

Droplet evaporation has been compared with calculations presented in Hinds (1999). Pure water droplets with initial diameters of $15 \mu m$, $10 \mu m$ and $4 \mu m$ exposed to 50% RH at 293 K have been calculated down to complete evaporation (in the present calculation, a droplet is considered as completely evaporated when its radius decreases below 100 nm since below this size, the calculation becomes very time consuming due to small time steps. This is justified since the evaporation time of a 100 nm droplet is negligible for RH's of interest). The calculations presented in Hinds (1999) have a different treatment of the corrections due to gas kinetic effects for small drop sizes. Instead of the modifications of D_v and K_a described in equations (2.38) and (2.39), Hinds (1999) multiplies the change of the drop diameter with time $\frac{d(d_p)}{dt}$ with the Fuchs correction factor ϕ which can be written as

$$\phi = \frac{2\lambda_{air} + d_p}{d_p + 5.33(\lambda_{air}^2/d_p) + 3.42\lambda_{air}} \tag{2.46}$$

(Davies, 1978), where λ_{air} is the mean free path of air. This leads to slight differences in the time required to evaporate a droplet, as can be seen in Fig. 2.8.

For each droplet size, the present calculation (Fig. 2.8a) has been done with the treatment of gas kinetic effects generally used in this work (dashed lines) and with the correction factor used by Hinds (solid lines). The differences in droplet evaporation time are not significant. However, comparison with the evaporation curves calculated by Hinds (Fig. 2.8b) shows that in the present calculation, evaporation is systematically slower by a factor around 0.82. One further difference in the calculations is that Hinds calculates the droplet temperature from the surrounding air temperature with an empirical formula involving the relative humidity. This droplet temperature is constant throughout the calculation, whereas in the present calculation, the droplet temperature is updated in each timestep. This leads to a slightly lower droplet temperature in the present calculation which slows down evaporation. However, this effect cannot account for the entire difference between the calculations. Different parameterizations of physical parameters like c_p or D_v or the saturation vapour pressure can also lead to differences in the results.
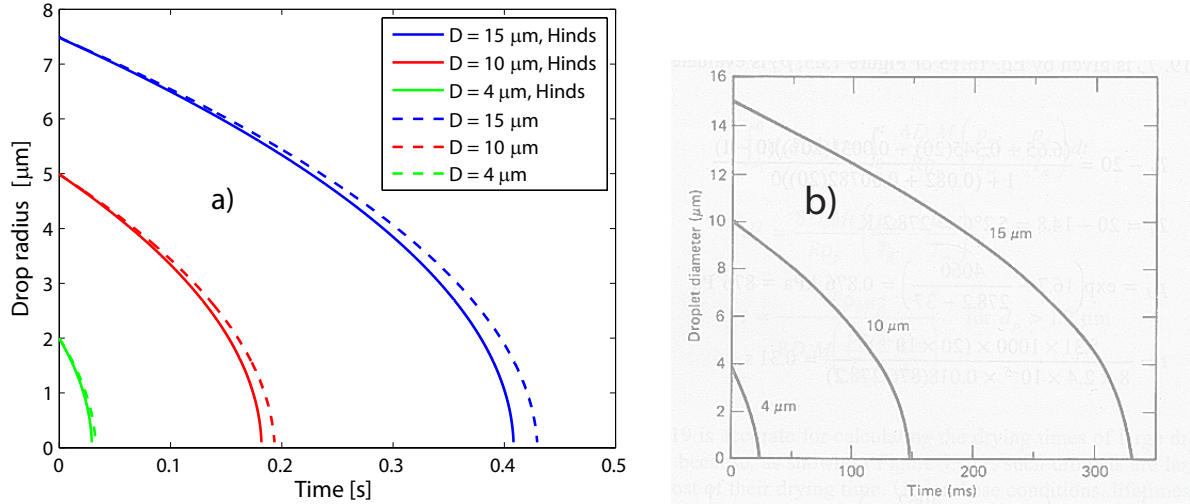
Figure 2.8: *Evaporation of pure water droplets at 50% RH at 293 K for different initial drop radii. a) Results of the present calculation with gas kinetic corrections generally used in the present work (dashed lines), and with gas kinetic corrections implemented according to Hinds (1999) (solid lines). b) Calculation by Hinds (1999).*

In any case, compared to the range of droplet evaporation times covering several orders of magnitude depending on the conditions and the droplet size, the differences between the present and the Hinds calculation are acceptable.

In a further test, the equilibrium radius of a salt solution droplet from the IDL calculation has been compared with the value calculated with Köhler theory. The evolution of an ammonium sulfate solution droplet with a dry mass of 1×10^{-15} kg and an initial diameter of $3\,\mu$m and $0.5\,\mu$m has been calculated at a temperature of 293 K and $RH = 90\%$. The result is shown in Fig. 2.9.
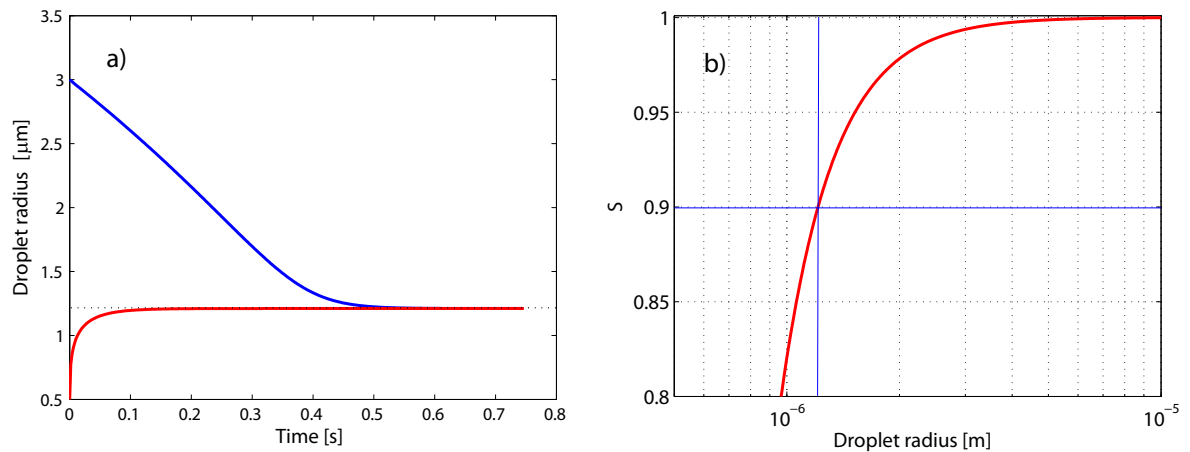
Figure 2.9: *a) Droplet size as a function of time for $(NH_4)_2SO_4$ solution droplets for a dry salt mass of 1×10^{-15} kg. Both droplets with initial radii $3\,\mu$m and $0.5\,\mu$m reach the same Köhler equilibrium radius. b) Ascending branch of the Köhler curve for the solution droplet in a).*

The final equilibrium radius for both calculated initial droplet sizes is $1.21\,\mu$m. Köhler theory combining Kelvin effect and the solute effect on the equilibrium water vapour pressure over a solution droplet gives the equilibrium saturation ratio S according to equation (2.42) and $S = \frac{e_a}{e_{sat,w}}$. For $RH = 90\%$ and $T = 293$ K, the theoretical equilibrium radius is $1.23\,\mu$m (cf. Fig 2.9 (b)) which is in reasonable agree-

34

ment with the IDL calculation. The fact that in the IDL calculation the mass density of the solution droplet varies with the droplet size whereas in the reference calculation it is assumed constant and equal to the density of water can lead to a slightly larger equilibrium radius in the reference calculation.

2.4.5 Importance of the Kelvin Effect

The sensitivity of pure water droplets to evaporation depends strongly on the droplet size. A water droplet with $20\,\mu m$ initial size can "survive" $RH = 90\%$ for more than half a minute, whereas a $3\,\mu m$ droplet completely evaporates in less than one second. The fact that the change in radius per unit time da/dt decreases for increasing droplet radius is primarily due to stronger gradients in vapour pressure over water surfaces with stronger curvature (i. e. smaller droplets). According to equation (2.25), the water vapour field around a spherical droplet with radius a is given by

$$\rho_v(r) = \rho_\infty + (\rho_a - \rho_\infty)\frac{a}{r}.$$

The gradient of this field at the droplet surface points in radial direction and has a magnitude of

$$\left(\frac{d\rho_v}{dr}\right)_{r=a} = -\frac{\rho_a - \rho_\infty}{a}$$

which is inversely proportional to the radius a. Therefore, small droplets evaporate faster than large ones even without taking the Kelvin effect into account. The Kelvin effect considerably increases the equilibrium water vapour pressure over a curved surface only for droplet sizes below 100 nm (see Fig. 2.10).
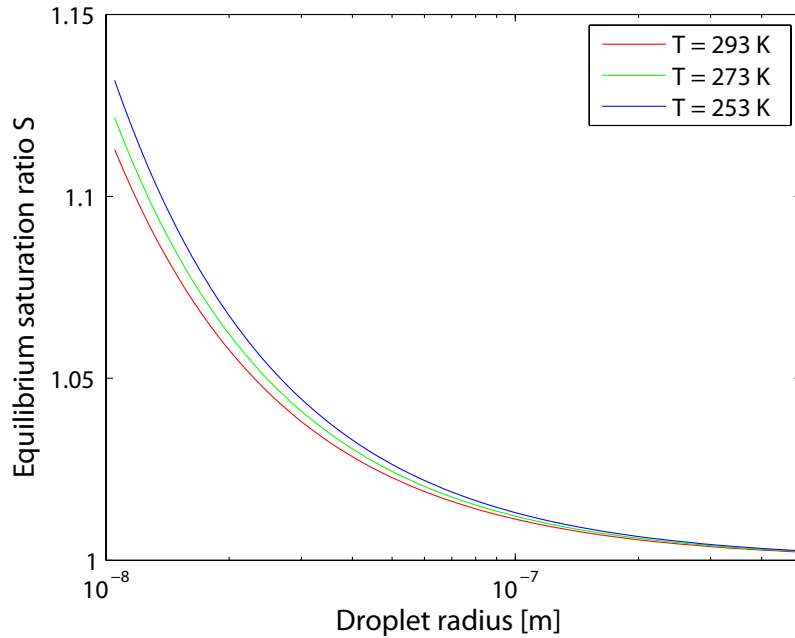
Figure 2.10: *Equilibrium vapour pressure over a droplet surface as a function of droplet radius (Kelvin effect) for different temperatures.*

Nevertheless, taking the Kelvin effect into account can be important also for larger droplet sizes, depending on the combination of droplet size and ambient RH. The Kelvin curves define a critical water germ size for every supersaturation. A droplet smaller than this critical germ size can reach a state of

lower total energy by getting rid of water molecules, whereas for a droplet larger than the critical germ size it is energetically favourable to acquire more water molecules (see section 1.3.1). Thus, the former droplet evaporates and the latter grows at the given supersaturation. The Kelvin effect is therefore only negligible when the droplet size is much larger than this critical germ size. Whereas for small droplets this is not the case for a wide range of supersaturations, large droplets can also be close to or below the critical germ size for a narrow range of low supersaturations. For example, a relatively "large" droplet with $1\,\mu$m diameter evaporates if the surrounding air is supersaturated by less than 0.2%. This is illustrated in Fig. 2.11:
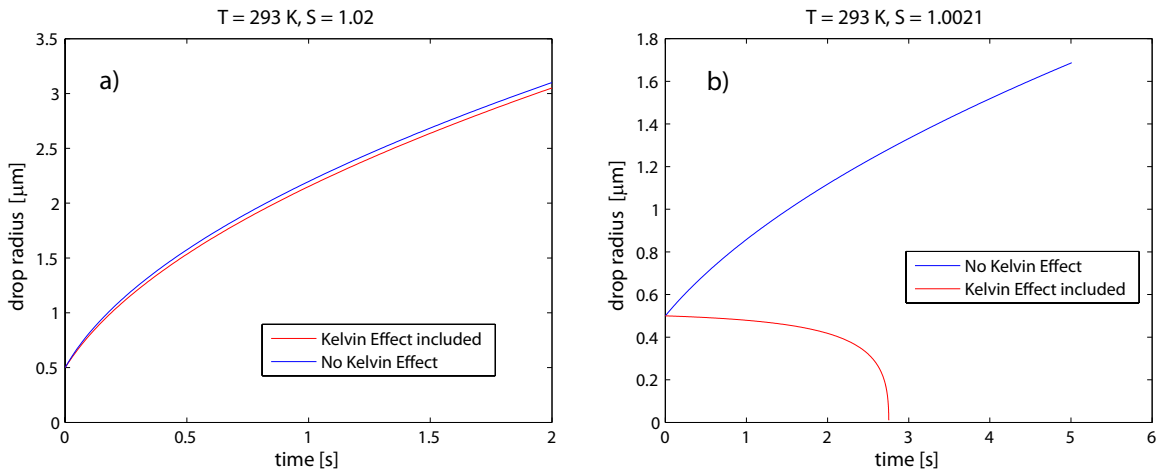
Figure 2.11: *Droplet evolution starting at 0.5 μm radius calculated with and without taking Kelvin effect into account. a) $S = 1.02$, b) $S = 1.0021$.*

At 2% supersaturation, the initial diameter of $1\,\mu m$ is well above the critical germ size, and thus neglecting Kelvin effect does not affect the calculation significantly. However, at 0.21% supersaturation, the initial droplet size is below the critical germ size and thus the droplet evaporates, whereas omitting Kelvin effect leads to an increasing droplet radius.

2.4.6 Evolution of IMCA Droplets

The aim of droplet evolution calculations is to obtain an estimate of the size of droplets nucleated in the IMCA chamber at the time when they leave IMCA and enter ZINC which, ideally, is operated at exactly 100% RH with respect to water. The most useful quantity in this context is the droplet radius as a function of the position in the IMCA chamber. In the calculations presented in Fig. 2.7 and 2.8, the conditions are assumed to be constant in both space and time. The real situation in the IMCA chamber is such that droplets travel through a volume with varying temperature and RH. In a Lagrangian perspective, one can consider a droplet traveling through IMCA as a stationary droplet subject to temperatures and RH's that change with time. The rate of change of these quantities can be determined from the FLUENT simulations. The evolution of the droplet radius as a function of the position in the IMCA chamber is obtained with the following procedure:

- A FLUENT simulation for a specific set of boundary conditions is performed which yields the fields of temperature, RH and flow velocity in the fluid zone.

- Profiles of temperature, RH and flow velocity along the path of a droplet are stored as databases for the calculation of droplet evolution.

- In the IDL calculation, the vertical position z_i in timestep i of the droplet is determined according to $z_i = z_{i-1} + \Delta t \cdot v_{i-1}$, where v_{i-1} is the flow velocity at the droplet position at timestep $i-1$.

The droplet position z_i is then used to determine the current flow velocity v_i, temperature T_i and relative humidity RH_i at the droplet position from the FLUENT profiles by linear interpolation. Interpolation is reasonable since the distance that a droplet travels in one timestep of the IDL calculation is typically around three orders of magnitude smaller than the average vertical extension of a FLUENT grid cell.

- The droplet radius r_i is updated according to diffusional growth or evaporation during timestep Δt at conditions defined by RH_i and T_i.

2.5 FLUENT Simulation Results

As mentioned earlier, FLUENT simulations of the IMCA chamber have served to assess the suitability of the chamber geometry prior to its construction. Furthermore, FLUENT simulations in combination with the droplet evolution calculation described in the previous section give an estimate of the response of the droplets to the conditions prevailing in the chamber and can help to find a set of good experimental parameters. The simulation represents an idealized case of the IMCA chamber. Therefore, the absolute values of calculated droplet size at the end of the chamber are expected to deviate somewhat from the values found experimentally. However, the sensitivity of the droplet size to variations in the experimental parameters can be studied in a detailed manner. The results of the performed simulation studies are presented in this section.

2.5.1 IMCA Flow Characteristics

In order to represent a typical experimental configuration, IMCA and ZINC parameters were set as follows for the present FLUENT simulation: The temperatures at the sample position in the IMCA chamber cover a range between 313 K at the inlet position and 243 K at the transition to ZINC (for a cross section of the geometry see Fig. 2.2). The heating blocks at the chamber top were set to 323 K and 303 K to obtain a typical supersaturation profile. The cooling blocks defining the transition between liquid water humidification and ice coating of the walls are kept at 273.3 K (cf. section 2.1.1). The ZINC chamber walls are set to 243 K and 250 K for RH_w to be close to saturation with respect to water. The sheath air is heated to 313 K at $RH_w = 80\%$. For the sample inlet conditions, two cases are considered corresponding to activation of cloud droplets within a W-CPC and directly in the IMCA chamber, respectively. In the former case, the sample air has a temperature of 313 K and is saturated to 100%. This is representative for the case where droplets nucleated in the W-CPC leave the W-CPC in a saturated air stream at 313 K. The choice of 313 K for the growth tube temperature of the W-CPC and the top part of IMCA is discussed in section 2.5.3. For droplet activation in IMCA, the sample is set to room temperature at a saturation of 80%. This corresponds to the case where aerosol particles produced at room temperature are directly led into the IMCA chamber. Figure 2.12 shows the temperature distribution in the top part of IMCA for the W-CPC activation case. Besides heater C and heater W, an additional temperature control is implemented which keeps the uppermost part with the inlet channels at 313 K. This part is thermally isolated from the rest of the chamber by a layer consisting of a material with low thermal conduction. The sample flow is set to 0.6 lpm which corresponds to the flow through a TSI 3782 W-CPC. Each sheath air channel adds a flow of 2.2 lpm. The inlet boundary conditions for these flows are set via a constant flow velocity over the entire cross section of the inlet area. The laminar flow profile then establishes whithin the first few centimeters after the inlet. This velocity is primarily dependent on the volumetric flow in the channel, but also on the temperature. Since in the experiment, all flows are controlled by mass flow controllers at room temperature, an increase in temperature at the inlet of a channel leads to an increased flow velocity due to the decreased gas density. The real flow velocity v is calculated based on the ideal gas law as
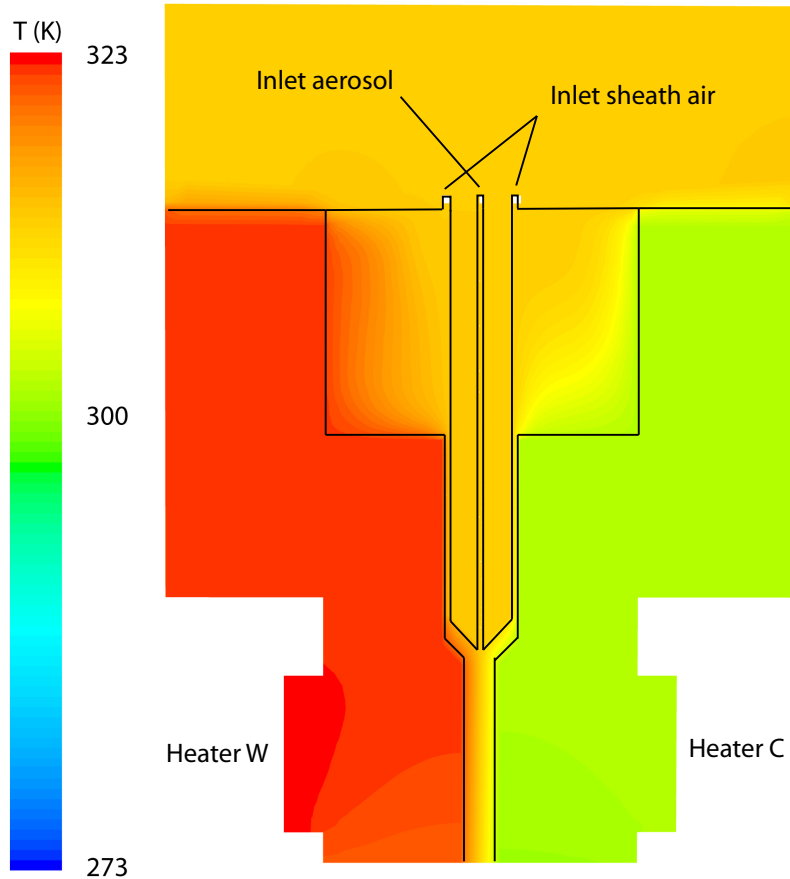
$$v = v_0 \cdot \frac{T}{T_0},$$

Figure 2.12: *Typical temperature distribution in the top part of IMCA.*

where v_0 denotes the flow velocity at room temperature T_0, and T is the real temperature at the inlet. The calculations of droplet evolution require the knowledge of temperature, RH and flow velocity along the path of a droplet in the IMCA chamber. Due to temperature differences between the warmer and the colder wall and the entailed buoyant modification to the laminar flow profile (see section 2.2.4) the pathline of a droplet started in the center between the two inlet blades deviates from a totally straight line through the chamber. Figure 2.13 shows the pathline of a droplet in the top part of IMCA and at the transition between IMCA and ZINC. These are the regions where buoyancy has the strongest influence on the flow profile.

The width of only 0.5 cm in IMCA as compared to 1 cm in ZINC and the decreasing wall temperature difference in flow direction only lead to a minor deviation from a straight pathline (Fig. 2.13a). In the ZINC chamber, the pathline is considerably shifted towards the cold wall (Fig. 2.13b). Thus, especially for the lower part of the simulation domain, it is important to record the profiles of temperature, velocity and RH along pathlines rather than straight lines.

As mentioned earlier, the lowermost part of IMCA is cooled to the ZINC temperature in order to allow for a smooth temperature transition between the chambers. In the present simulation of a representative case, two ways of cooling the low part of IMCA are considered: In the default case, the cooling channels of the low cooling blocks (cf. Fig. 2.2) carry the cooling liquid of the corresponding ZINC wall and therefore have the same temperature as the ZINC walls (this case will be referred to as "$\Delta T \neq 0$ case" in the following). In the second case, both cooling blocks are set to the same temperature which is the average of the ZINC wall temperatures (referred to as the "$\Delta T = 0$ case"). The way in which the lower part of IMCA is cooled affects the saturation conditions and thus the droplet evolution. Figure 2.14 shows the temperature profile along a droplet trajectory from the inlet of IMCA to the transition
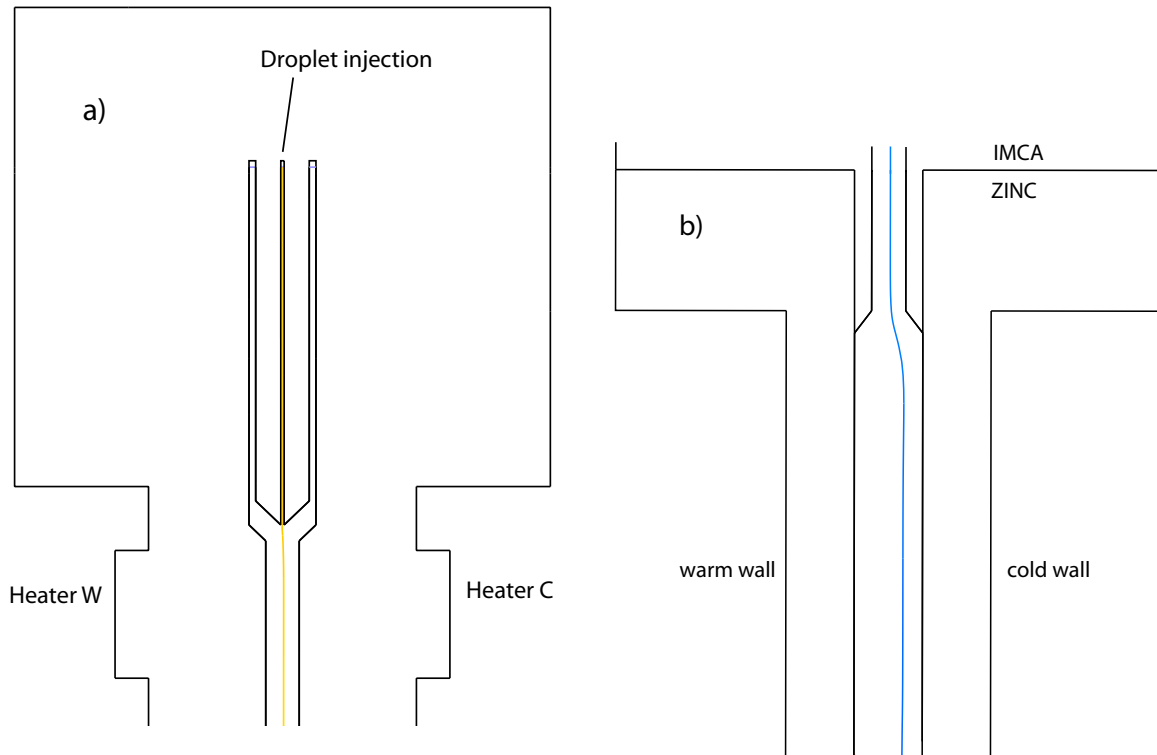
Figure 2.13: *Pathlines of a droplet starting in the center between the inlet blades: a) in the top part of IMCA, and b) at the transition between IMCA and ZINC.*

into ZINC and the first 10 cm of the ZINC chamber for the case of the lower cooling blocks being at different temperatures.

The three temperature control units define two cooling sections with different temperature gradients. The temperature difference between the walls is highest in the top part of IMCA, then decreases towards the intermediate cooling section, and increases again towards the ZINC chamber in the $\Delta T \neq 0$ case. The plot in Fig. 2.14 refers to the case where droplets are nucleated directly in the IMCA chamber, therefore the air temperature at the inlet is 293 K (room temperature). It can be seen that at some locations with small wall temperature differences, the air and droplet temperatures are higher than the corresponding warm wall temperature. This is due to the fact that the air at the center of the chamber at a certain vertical position is always somewhat warmer than the average of the corresponding wall temperatures as long as there is a vertical temperature gradient in the chamber. This difference depends on the flow velocity and the width of the chamber and will be discussed later. The droplet temperature can in general differ from the surrounding air temperature if the air temperature changes so quickly that the heat exchange from the droplet to the air is not fast enough to establish equilibrium, or if latent heat is released or consumed. The droplet temperature in Fig. 2.14 only differs significantly from the air temperature at the beginning of the upper cooling section where the droplet grows and latent heat is released. The largest temperature difference corresponds to the largest supersaturation in the upper cooling section which can be seen in Fig. 2.15. The fact that there is no discernable difference between air and droplet temperature in the lower cooling section with the largest temperature gradient shows that the temperature change of the surrounding air is slow enough for the droplet temperature to relax to the air temperature. *RH* profiles of the IMCA chamber are shown in Fig. 2.15. The red and green curves represent the *RH* conditions for droplet activation via W-CPC, whereas the blue curve represents the case of a dry sample at the inlet carrying aerosol particles that are directly activated in IMCA.

All three curves show a supersaturation peak close to 10% supersaturation in the first few centimeters of the chamber. This peak is at the position of the largest wall temperature difference with humidified
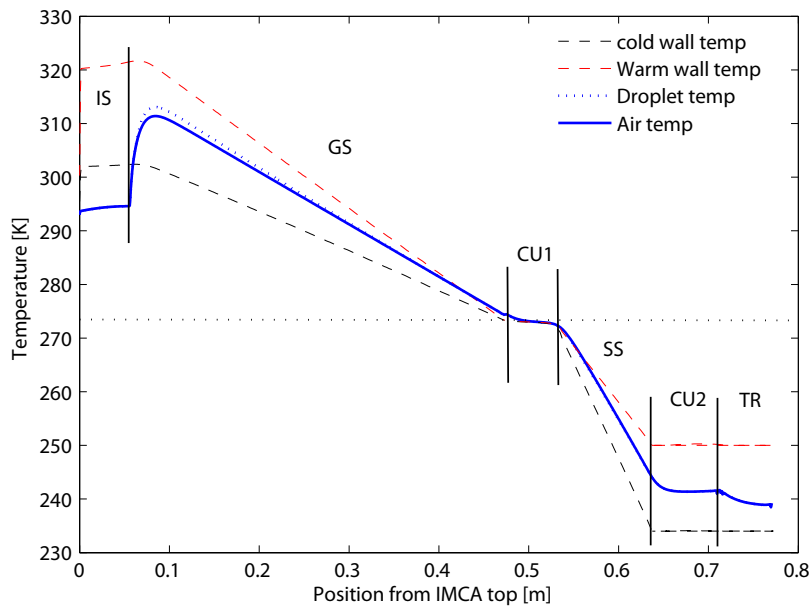
Figure 2.14: *Profiles of air and droplet temperature along a droplet trajectory. Dashed lines indicate the wall temperatures. The six sections indicated by abbreviations refer to the ones indicated in Fig. 2.2 and represent the following sections of IMCA: IS: Inlet section until the sample flow is combined with the sheath air flows (see Fig. 2.12). GS: Growth section. CU1: Cooling unit 1 at 273.3 K. SS: Supercooling section. CU2: Cooling unit 2. TR: Transition and first centimeters of the ZINC chamber.*
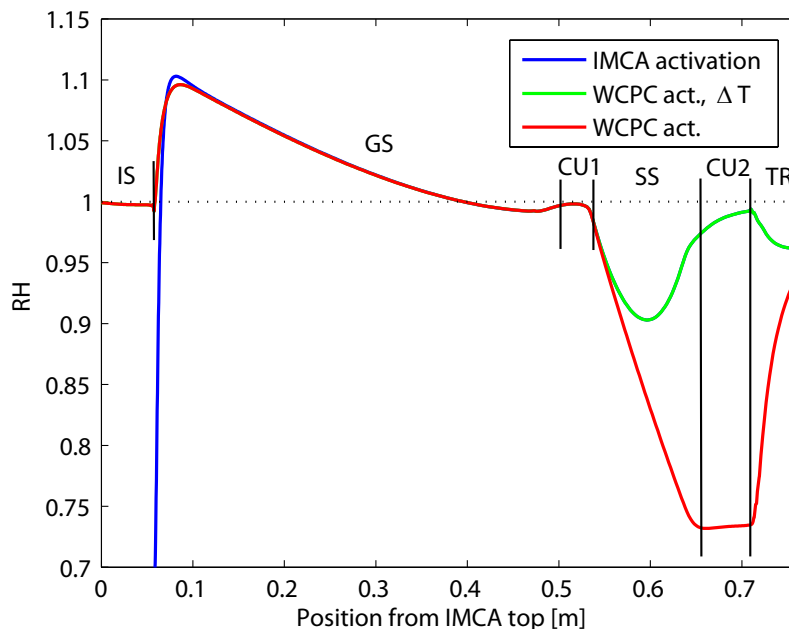
Figure 2.15: *Relative humidity (RH) in the IMCA chamber along a droplet trajectory. The blue curve represents injection of a dry aerosol sample which has to be activated to cloud droplets in IMCA. The red and green curves represent the case of injected cloud droplets in a humid air flow previously activated in a W-CPC. For the green curve, the low cooling blocks of IMCA are set to the same temperature, whereas for the red curve, they are set to the corresponding ZINC wall temperature.*

40

walls. The supersaturation peak of the blue curve is slightly higher than the one of the other curves because in this case, the sample air is injected with a temperature of 293 K instead of 313 K. While the sample air is heated up to the surrounding temperature, it gets supersaturated to a higher degree than air entering with a temperature of 313 K (in section 2.5.4, this will be discussed in more detail). After the peak, *RH* decreases and falls slightly below 100% before it increases again to 100% in section CU1 where both walls are at 273.3 K. In the lower part of IMCA, the red curve (labeled with ΔT) corresponds to the $\Delta T \neq 0$ case, whereas the green curve represents the $\Delta T = 0$ case. In the latter case, *RH* considerably decreases below 100% whereas in the former case, *RH* increases again towards section CU2 due to the increasing wall temperature difference (cf. Fig. 2.14). The decrease of the red curve in section TR is due to the shift of the droplet pathline out of the supersaturation maximum when the droplet enters the ZINC chamber. These different *RH* conditions in the low part of IMCA affect the droplet evolution and the droplet temperature. A detailed view of air and droplet temperatures in sections CU2 and TR is shown in Fig. 2.16.
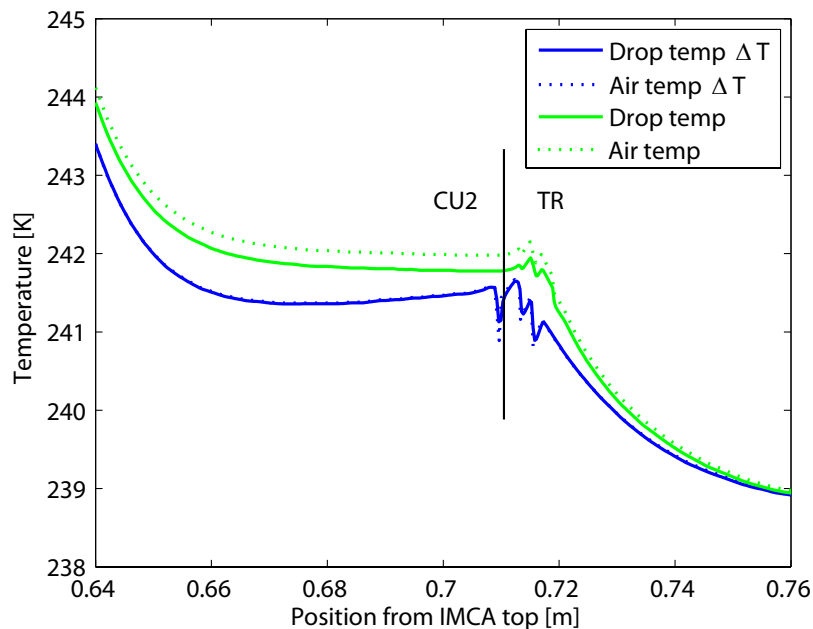
Figure 2.16: *Detailed view of the temperature profiles at the lower end of IMCA for the two cases with the lower cooling blocks at the same temperature or at the temperatures of the ZINC walls (labeled with ΔT)*

The blue curves represent the $\Delta T \neq 0$ case, whereas both blocks have the same temperature for the green curves. The temperature at a certain vertical position is lower in the $\Delta T \neq 0$ case because of a slight shift of the droplet trajectory towards the colder wall compared to the $\Delta T = 0$ case. Without temperature difference, *RH* is lower in sections SS, CU2 and TR and therefore the droplet temperature is lower than the surrounding air temperature by up to 0.5 K due to the latent heat required in the evaporation process. This compares to almost no difference between air and droplet temperature in the $\Delta T \neq 0$ case. In section TR, the temperature decreases by approximately 2 K even if the low cooling blocks of IMCA are set to the corresponding ZINC wall temperature. This is due to the droplet trajectory shifted towards the colder wall when the droplet enters ZINC. A smoother temperature transition at the beginning of ZINC could be obtained by adjusting the cooling liquid temperature in CU2. Since this, like the $\Delta T = 0$ case also, involves an additional temperature regulation independent from the ZINC wall temperatures, a more realistic way of improving the temperature transition is to avoid deflection of the droplet path lines towards the cold ZINC wall. This can be done by increasing the total flow in the ZINC chamber

by additional sheath air, such that buoyancy at the warm ZINC wall becomes less important. Such a modification is planned in the future.

The staggered behaviour of the curves at the transition between sections CU2 and TR is an artefact of the CFD simulation. In horizontal direction, the temperature difference between two adjacent grid cells is much larger than in vertical direction if the wall temperatures differ significantly at the corresponding position. Since in this case, the droplet trajectory at the transition between IMCA and ZINC has a horizontal component, some non-continuity in the temperature profile has to be expected. This effect could be reduced by increasing the grid resolution.

2.5.2   Subsaturation in IMCA

From Fig. 2.15, it is obvious that besides the subsaturation in the ice coated part of IMCA between CU1 and CU2, a slight subsaturation establishes after the supersaturation peak at a position between 0.4 m and 0.5 m, before RH_w increases back to 1 at CU1. The occurrence of a subsaturation in this part of IMCA might be surprising since a temperature difference between two humidified walls implicates RH_w to be greater than 1 (see section 2.2.3), even if the temperature difference is small. However, this is strictly valid only when the temperature profile between the walls is linear. In fact, the linear temperature profile obtained in section 2.2.3 is a result of the reduction of equation (2.1) to one dimension, which is not possible for the IMCA chamber where the temperature T also depends on the vertical coordinate y. Instead, the horizontal temperature profile in IMCA is convex, i. e. lying above a linear profile. A simulated horizontal temperature profile at a vertical position $y = 0.4$ m (i. e. just after the transition from supersaturated to subsaturated in Fig. 2.15) is shown in the second panel of Fig. 2.17.
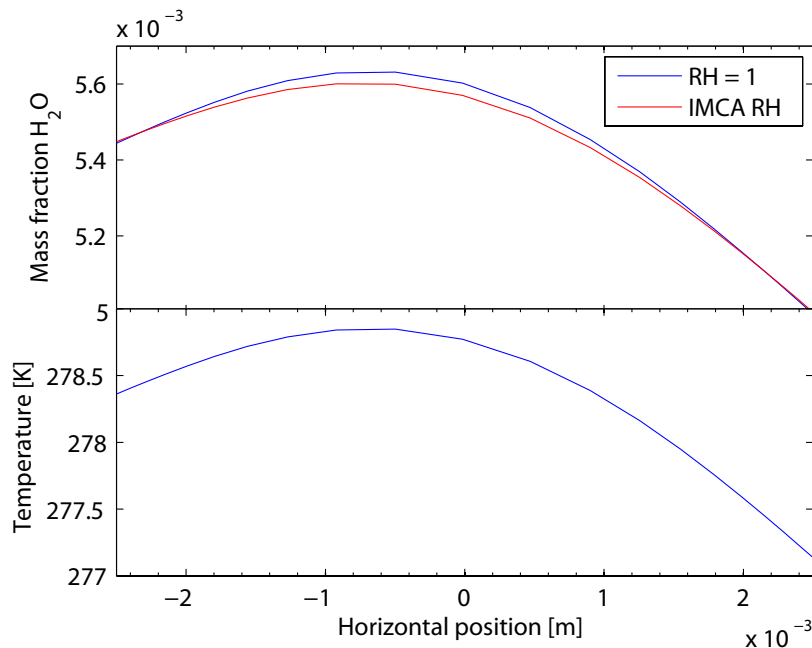
Figure 2.17: *Upper panel: Horizontal profiles of the mass fractions of* H_2O *in the sample air around 10 cm above CU1. The red curve displays the profile obtained from the FLUENT simulation, whereas the blue curve displays the value calculated for* $RH_w = 1$ *at the corresponding temperature.*

Given the vertical temperature gradient in IMCA, a linear horizontal temperature profile would only be possible if the thermal conductivity K of air was infinitely large. A finite value of K inevitably results in the formation of a convex temperature profile. The convexity increases with the vertical temperature gradient. In general, a horizontal temperature profile lying above the linear one between the two wall temperatures leads to a RH_w profile below the one expected for a linear temperature profile, because

the diffusion of water is faster than the diffusion of heat (this is discussed in more detail in section 2.5.4). The fact that the convex temperature profile in IMCA can lead to $RH_w < 1$ in spite of a finite wall temperature difference is illustrated in the first panel of Fig. 2.17. The mass fraction of water vapour obtained from the FLUENT simulation lies below the mass fraction calculated for $RH_w = 1$ at the corresponding temperature.

2.5.3 Droplet Evolution in the IMCA Chamber

Influence of Supersaturation Peak and ZINC Temperature

According to the procedure presented in section 2.4.6, calculations of the droplet radius as a function of the position in the combined ZINC and IMCA chambers have been performed. Figure 2.18 shows the growth and evaporation of droplets for a set of different conditions in IMCA.
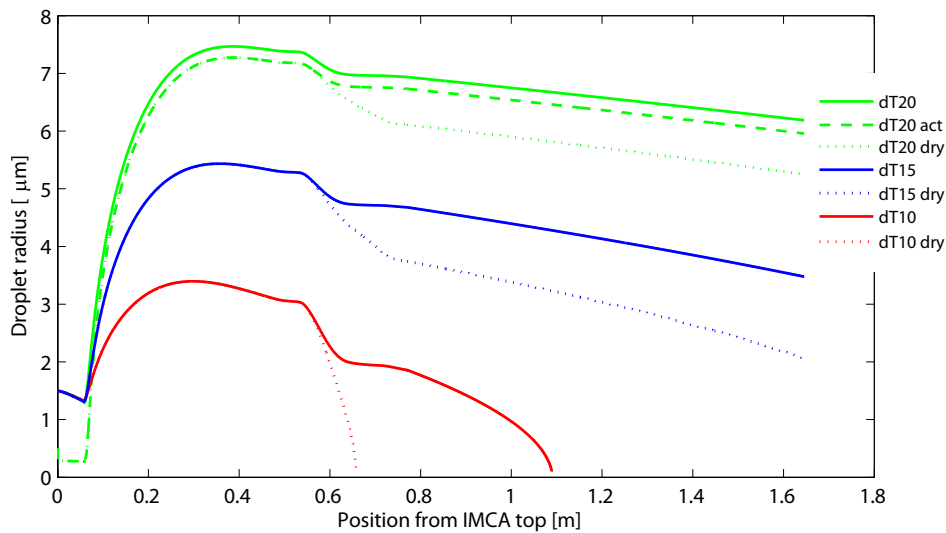
Figure 2.18: *Calculations of the droplet evolution between the top of IMCA (inlet section) and the bottom of ZINC (detector position) for different IMCA supersaturations (represented by top wall temperature differences $dT = 10\,K$, $dT = 15\,K$, and $dT = 20\,K$). Dotted lines labeled "dry" represent the $\Delta T = 0$ case where the two cooling blocks of CU2 are at equal temperatures leading to lower saturation than in the $\Delta T \neq 0$ case where the cooling blocks of CU2 carry the cooling liquid of the corresponding ZINC walls. The green dashed line represents droplet activation directly in IMCA for $dT = 20\,K$, whereas prior droplet nucleation in a W-CPC is assumed for all other curves.*

Three different temperature differences, $dT = 10\,$K, $dT = 15\,$K, and $dT = 20\,$K are applied to the heaters at the top of the IMCA walls, whereas the temperature at the sample inlet is always 313 K. For each dT, the droplet evolution is shown for both cases with and without a temperature difference between the IMCA walls at CU2 (i.e., the $\Delta T \neq 0$ and $\Delta T = 0$ cases). The calculations are started with a droplet of $3\,\mu m$ initial diameter, which roughly corresponds to the size of a droplet at the exit of a TSI 3782 W-CPC. For comparison, the case of direct droplet nucleation in the IMCA chamber is shown as the dashed green line in Fig. 2.18 for $dT = 20\,$K. For the IMCA chamber including the transition and the first 10 cm of the ZINC chamber, droplet evolution is calculated based on the profiles of temperature, RH_w and flow velocity from the FLUENT simulation, according to section 2.4.6. For the remaining part of ZINC, the conditions are assumed to be constant, and droplet evaporation is calculated for a residence time of 14 s at $T_{ZINC} = 243$ K and $RH_w = 95\%$. This RH_w can be seen as a lower boundary for RH_w in ZINC during an experiment. Although in an experiment, the ZINC wall temperatures are tuned to obtain a saturation

as close to $RH_w = 100\%$ as possible at the position of the sample layer, uncertainties can lead to a lower value of RH_w. As a total flow rate of 5 lpm leads to a considerable shift of the aerosol layer towards the cold wall of ZINC, the aerosol layer is not exactly situated at the maximum of the saturation profile. This entails a gradient of RH_w over the aerosol layer. Figure 2.19 visualizes a typical saturation profile in ZINC at the sample position assuming a perfectly linear temperature profile between the walls. Even if this is not accurate (see section 2.5.2), it serves to get an estimate of the range of RH_w in the sample layer. Wall temperatures are set to $T_w = 250$ K and $T_c = 234$ K, respectively.
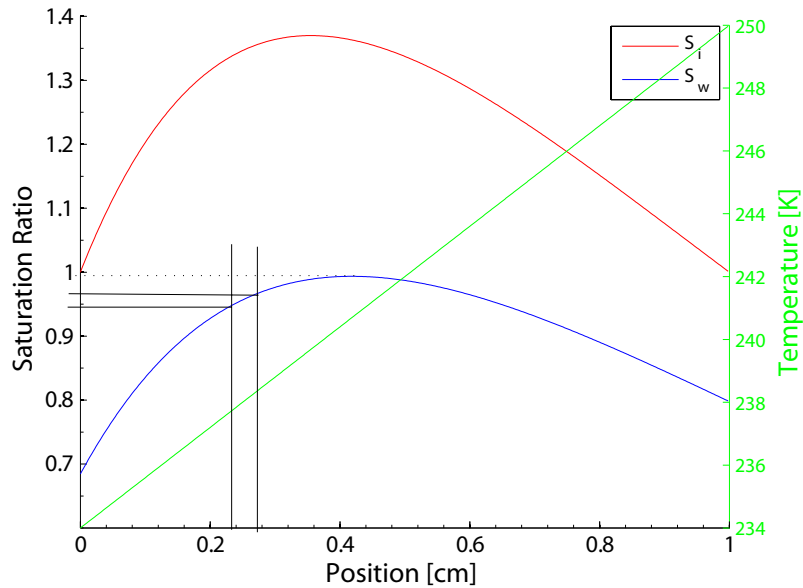
Figure 2.19: *Typical calculated saturation profile in the ZINC chamber, based on a linear temperature gradient between the walls. The vertical black lines indicate the boundaries of the sample layer.*

A difference of 2 - 3% has to be accounted for between the minimum and the maximum RH_w in the sample layer. Since the maximum RH_w in the layer must not be higher than 100% in order to avoid condensation nucleation in ZINC, a fraction of the droplets encounters conditions subsaturated by at least 2 - 3% in ZINC. Furthermore, temperature fluctuations of ± 0.25 K in the cooling liquid of the cold wall have been observed during the experiments, which gives rise to an uncertainty around 1.5% in RH_w. Altogether, we consider it reasonable to take $RH_w = 95\%$ as a lower boundary for the saturation in the ZINC main chamber. Shortly before reaching the detector, droplets additionally encounter subsaturation because the detector is mounted on a 14 cm long section which is cooled to equal wall temperatures (see section 4.1.4). However, as in this section the chamber width narrows from 30 cm to 15 cm at the position of the detector, the residence time from the ZINC main chamber to the detection volume is only around one second. Therefore we did not take the additional subsaturation in this section into account. The error in the final droplet size arising from this simplification can be significant for small values of dT, but can be considered unimportant for values of dT used in the experiments.

The difference in final droplet size between activation in IMCA and W-CPC-activation appears to be insignificant. As the motivation to use a W-CPC to activate droplets is mainly to obtain larger droplets which are less likely to evaporate in the cold part of the experiment, this simulation result questions the worthiness of activating droplets with the W-CPC compared to direct droplet activation in IMCA. However, the direct comparison between the two cases is difficult, since the present calculation of droplet evolution does not include the nucleation process itself. Instead, in the case of IMCA activation, the calculation starts off with a small droplet (diameter $d = 1 \mu$m) at the inlet of IMCA. If an aerosol particle immediately nucleates a cloud droplet upon entering the supersaturated region after the IMCA inlet, the

error inferred by starting off with a small droplet instead of a bare particle is negligible. Although the $1\,\mu$m droplet has an advance in the growth process and reaches a larger size in the supersaturated region, the difference in the maximum droplet size is unimportant, since the growth rate of a droplet decreases with increasing droplet radius. Differences in initial droplet size are therefore reduced during the droplet growth, which can be seen comparing the green solid line and the green dashed line in Fig. 2.18. On the other hand, the time required for the nucleation process to take place when a bare particle enters the supersaturated region is unknown for the present experiment. As the sample is exposed to a high supersaturation for a relatively short time only, a delay of the nucleation process might have a considerable influence on the maximum droplet size as compared to the case of injecting an already nucleated droplet into IMCA. In this case, the calculation for droplets nucleated in IMCA might overestimate the actual droplet sizes reached in the top part of IMCA.

Test experiments did not yield a perceptibly lower minimum IMCA supersaturation required to observe droplets at the bottom of ZINC when droplets were activated with a W-CPC, which supports the simulation results of similar final droplet sizes for both cases. For this reason, further simulation results will be presented for the case of IMCA activation only.

Droplet evolution in IMCA crucially depends on the temperature difference dT applied to the electrical heaters at the top of IMCA. Whereas for $dT = 20\,$K, a droplet quickly grows to a size large enough that it is not strongly affected by the subsaturation in the cold part of IMCA and ZINC, $dT = 10\,$K clearly does not provide sufficient droplet growth. For the $\Delta T = 0$ case, labeled with "dry" in Fig. 2.18, a droplet does not even reach the ZINC chamber, but evaporates between CU1 and CU2 of IMCA. For the $\Delta T \neq 0$ case, the droplet evaporates somewhere in the ZINC chamber. The decrease of the droplet radius at a position around 0.6 m (i. e. in the RH_w minimum between CU1 and CU2) is more pronounced for smaller droplet sizes, again since small droplets evaporate more quickly than larger ones. In Fig. 2.20, the supersaturation peak in the upper part of IMCA is displayed for the three values of dT.

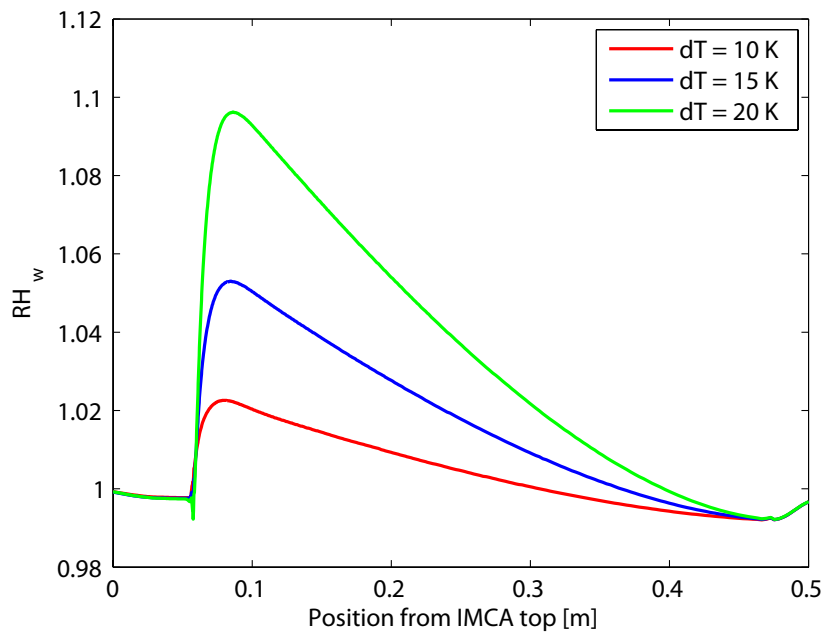**Figure 2.20:** *Supersaturation peak in the upper part of IMCA for different temperature differences dT applied to the electrical heaters at the top of the IMCA walls. A larger temperature difference leads to a higher supersaturation peak.*

The peak supersaturation depends non-linearly on dT: A doubling of dT from 10 K to 20 K leads to an increase of the maximum supersaturation from around 2% to around 10%. Based on the results of

these droplet evolution calculations, the temperature difference dT has been set to at least 20 K in IMCA experiments.

Besides the RH_w profile, the experimental temperature in ZINC also plays a significant role for the droplet evolution. Figure 2.21 shows a comparison of the droplet evolution for experimental temperatures of $T_{\mathrm{ZINC}} = 243\,\mathrm{K}$ and $T_{\mathrm{ZINC}} = 253\,\mathrm{K}$, respectively, for an IMCA temperature difference $dT = 15\,\mathrm{K}$ and a ZINC RH_w of 95%.
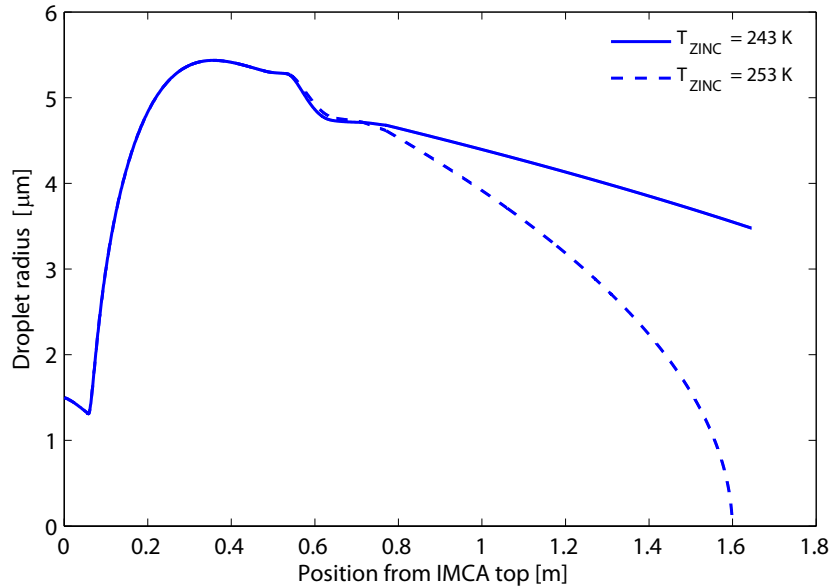
Figure 2.21: *Droplet evolution for two different experimental temperatures in ZINC for an IMCA temperature difference $dT = 15\,K$ and a ZINC RH_w of 95%.*

Whereas for $T_{\mathrm{ZINC}} = 243\,\mathrm{K}$, a droplet should reach the detector with a diameter around $7\,\mu\mathrm{m}$, the droplet does not survive the conditions at $RH_w = 95\%$ for $T_{\mathrm{ZINC}} = 253\,\mathrm{K}$. This is mainly due to the larger gradient in the partial pressure of water vapour between the sample air and the droplet for the same RH_w at warmer temperatures. Whereas the mass diffusivity D_v is only around 8% larger for $T_{\mathrm{ZINC}} = 253\,\mathrm{K}$ compared to $T_{\mathrm{ZINC}} = 243\,\mathrm{K}$ (according to equation 2.12), the mass fraction of water vapour in air at $RH_w = 100\%$ is 7.6×10^{-4} for $T_{\mathrm{ZINC}} = 253\,\mathrm{K}$, but only 3.1×10^{-4} for $T_{\mathrm{ZINC}} = 243\,\mathrm{K}$. That is, higher experimental temperatures require particular attention to the relative humidity in ZINC.

Influence of the Sample Temperature within IMCA

The fact that the water vapour density at a certain relative humidity is larger for warm air than for cold air implies that a water droplet grows faster at warm temperatures, given a certain supersaturation. Consequently, one might consider operating IMCA at highest possible top temperature to optimize conditions for droplet growth. The influence of the temperature that the sample and sheath air flows are heated to between the electrical heaters at the top of the IMCA chamber has been investigated by comparing the RH_w profiles and the droplet evolution for three different pairs of heater temperatures: 293/313 K, 303/323 K, and 313/333 K. These top wall temperatures correspond to temperatures in the center of the aerosol layer of 303 K, 313 K and 323 K between the heaters. Accordingly, we will refer to these three cases as $T_{top} = 303\,\mathrm{K}$, $T_{top} = 313\,\mathrm{K}$ and $T_{top} = 323\,\mathrm{K}$. The inlet sample and sheath air temperatures were also set to 303 K, 313 K and 323 K. For $T_{top} = 323\,\mathrm{K}$, the effect of a cooler inlet temperature, $T_{in} = 293\,\mathrm{K}$, was additionally tested. The results are shown in Fig. 2.22.

At first sight contra-intuitively, a lower temperature leads to a higher supersaturation peak for a

Figure 2.22: *RH_w profiles and droplet evolution for different temperatures in the center of the aerosol layer at the top of IMCA: $T_{top} = 303\,K$, $T_{top} = 313\,K$ and $T_{top} = 323\,K$. The temperature difference between the heaters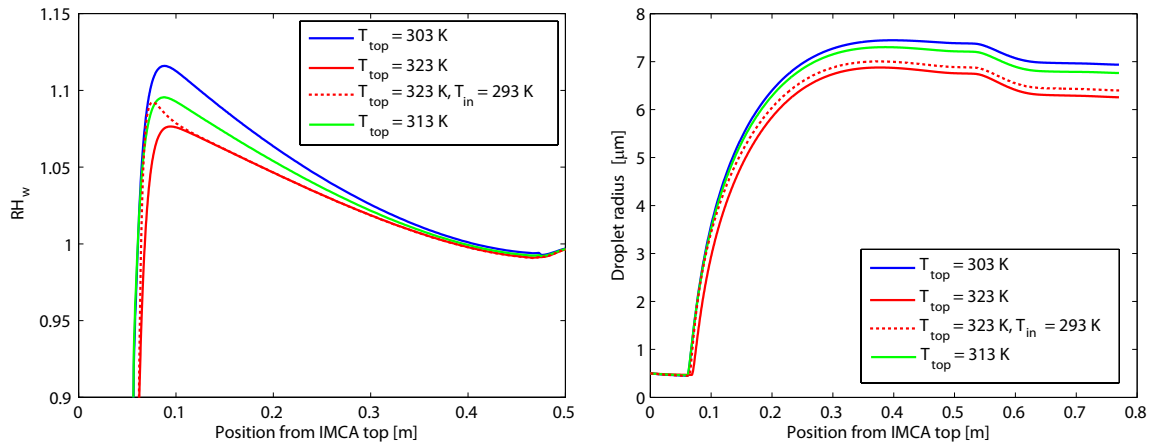 is 20 K for all cases, and the temperature in ZINC is set to 243 K. The dashed red lines represent the $T_{top} = 323\,K$ case with the inlet section at 293 K instead of 323 K.*

fixed heater temperature difference of $dT = 20\,K$. This effect is stronger than the generally decreasing concentration of water vapour for decreasing temperature, leading to a slightly larger droplet size for $T_{top} = 303\,K$ than for $T_{top} = 313\,K$. Increasing the temperature to $T_{top} = 323\,K$ reduces the supersaturation peak and leads to smaller droplets at the end of IMCA. Keeping the inlet section at $T_{in} = 293\,K$ instead of 323 K for the $T_{top} = 323\,K$ case increases the supersaturation peak. This mechanism will be discussed in more detail in section 2.5.4. The resulting droplet size for this case is still smaller than for the standard case $T_{top} = 313\,K$. This suggests that temperatures larger than $T_{top} = 313\,K$ are not useful for the present experiments. The advantage of lower temperatures is relatively small. Furthermore, the feasibility of lower temperatures is technically limited. Due to heat conduction from the warmer wall to the cooler wall despite the implemented isolations, keeping a temperature difference of $dT = 20\,K$ requires active cooling of the top part of the cooler IMCA wall for temperatures below $T_{top} = 313\,K$. Hence, we consider $T_{top} = 313\,K$ as the optimum sample temperature for the top of IMCA.

Influence of the Flow Rate

Unlike the ZINC chamber having a plate distance of 1 cm, IMCA has been built with a plate distance of 0.5 cm. Given the relatively steep temperature gradient between CU1 and CU2 in IMCA, a chamber width of 1 cm would lead to insufficient adaptation of the sample temperature to the wall temperature. This is illustrated in Fig. 2.23 a, where a horizontal temperature profile between the walls some centimeters above CU2 is plotted for a chamber width $d = 0.5$ cm and for $d = 1$ cm (the temperature in ZINC is set to 243 K). For comparison, the black lines indicate linear temperature profiles between the chamber walls. In both cases, a total flow rate of 5 lpm is assumed, leading to a lower flow velocity in the $d = 1$ cm case.

In Fig. 2.23 b, the difference between the actual temperature profile and the linear profile is plotted. It is obvious that this difference is considerably larger for $d = 1$ cm than for $d = 0.5$ cm, i. e. the adaptation of the sample temperature to the wall temperatures is worse, although the flow velocity is slower by a factor of 2. Good temperature adaptation is important for controlled cooling of the nucleated cloud droplets, and furthermore, an excessively convex temperature profile, as for $d = 1$ cm reduces the relative humidity in the sample layer considerably, as discussed at the beginning of this section. The consequence of these considerations is that the vertical temperature gradient established in IMCA requires a plate distance smaller than the one used in ZINC. $d = 0.5$ cm has been chosen as the minimum
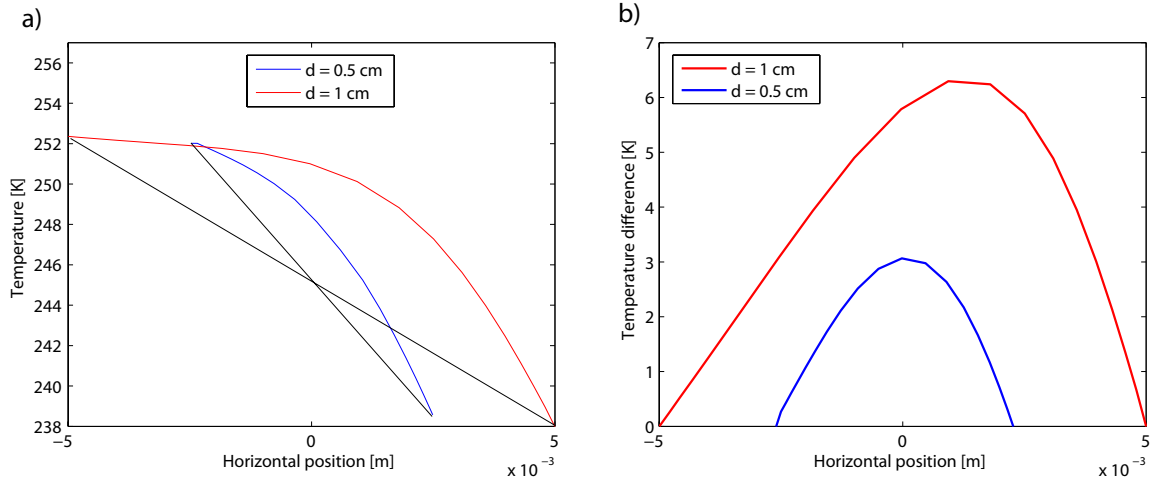
Figure 2.23: *a) Horizontal temperature profiles in IMCA taken a few centimeters above CU2 for a plate distance of d = 0.5 cm and the hypothetical case of d = 1 cm. Black lines indicate a linear temperature profile between the walls for comparison. b) Difference between the temperature profiles plotted in a) and the corresponding linear profile.*

distance which still allows for the implementation of humidified filter papers on both walls. As an alternative, reducing the vertical temperature gradient in IMCA would require a massive increase in the chamber length which is not realistic due to laboratory dimensions.

The total flow rate in the experiment has to be chosen as a compromise between two counteracting effects: A low flow rate allows for better temperature adaptation, i. e. a better horizontal temperature profile between the walls. Compared to a standard ZINC experiment with a total flow rate of 10 lpm, the flow has to be reduced at least to 5 lpm in order to obtain an acceptable temperature adaptation. A further convincing argument to use a flow rate lower than 10 lpm is that droplets can grow to larger sizes at a lower flow rate. Figure 2.24 shows that even though the RH_w profile is not significantly different for the 5 and 10 lpm cases, the final droplet size is considerably smaller for the 10 lpm case due to the shorter time that droplets are exposed to supersaturation.
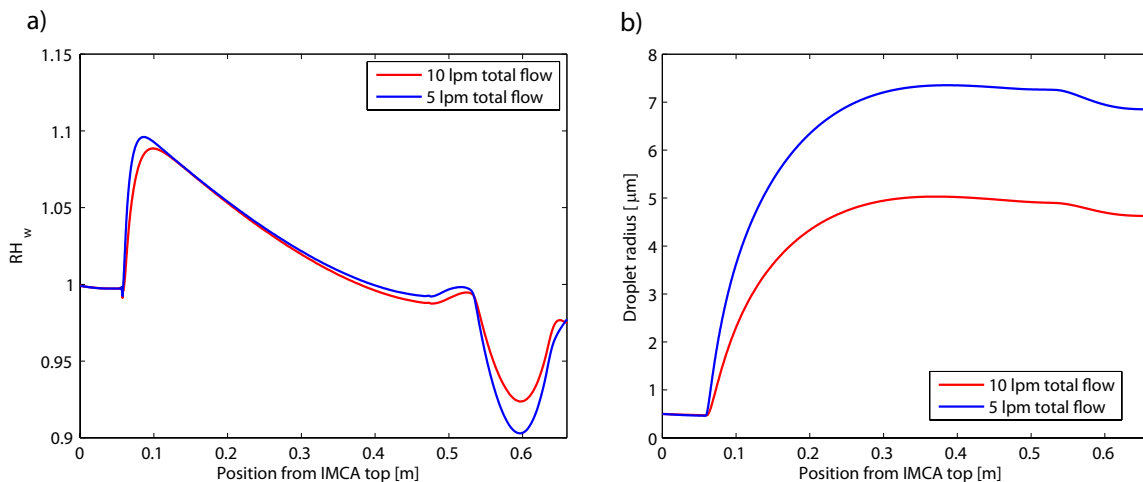
Figure 2.24: *Profiles of RH_w and droplet evolution for 10 lpm and 5 lpm total flow. $T_{top} = 313\,K$ with a top wall temperature difference $dT = 20\,K$, and $T_{ZINC} = 243\,K$.*

On the other hand, a decreasing flow rate increases the influence of buoyancy on the warm walls of ZINC and IMCA. Whereas for a typical wall temperature difference, the influence of buoyancy in ZINC

48

is moderate for a 10 lpm flow, a backflow layer establishes on the warm wall for 5 lpm (see section 2.2.4), shifting the sample layer towards the cold wall of ZINC. Taking this into account, the flow rate should not be lower than 5 lpm in order to keep the ZINC flow regime stable.

2.5.4   Cold Inlet - A Useful Modification?

As mentioned earlier, the IMCA chamber can be considered as a special case of a CFDC, and uses the same principle with two humidified walls at different temperatures to generate supersaturation as a CFDC. Another mechanism is used to generate high supersaturations in CPC's: Particles in a saturated, cool air stream enter into a humidified, warm growth tube. After the sharp temperature transition, a high supersaturation establishes in the center of the growth tube which gradually decreases with increasing distance from the transition. This supersaturation peak is sufficient to basically activate all particles entering the CPC. The supersaturation of the air stream in such a setup is a consequence of the different diffusivities of water vapour and heat. Phenomenologically, it can easily be explained by the different molecular mass of H_2O and air (mostly N_2) molecules. Due to the equipartition theorem, each gas molecule has the same kinetic energy, dependent on temperature. The light H_2O molecules therefore travel at a higher average velocity than the heavier air molecules. Since the diffusion of water vapour in air is driven by the motion of H_2O molecules, and heat conductance by the motion of air molecules and energy transfer between them, one can conclude that water vapour diffuses more quickly than heat. Direct comparison of the diffusion coefficients of water vapour in air and temperature illustrates this. Dividing the heat conductivity of air (in $J\,s^{-1}\,m^{-1}\,K^{-1}$) by the product of heat capacity and density of air, one can obtain a temperature diffusivity $K' = \frac{K}{c_p \rho}$ which can be compared with the mass diffusivity D_v of H_2O in air. Both D_v and K' have the unit $m^2\,s^{-1}$. In Fig. 2.25, K' and D_v obtained with the FLUENT simulation are plotted for the upper section of IMCA (i. e. between the inlet section and CU1) for an inlet sample temperature of 313 K. For the entire temperature range between 273 K and 313 K, the diffusivity of H_2O is clearly larger than the one of temperature.
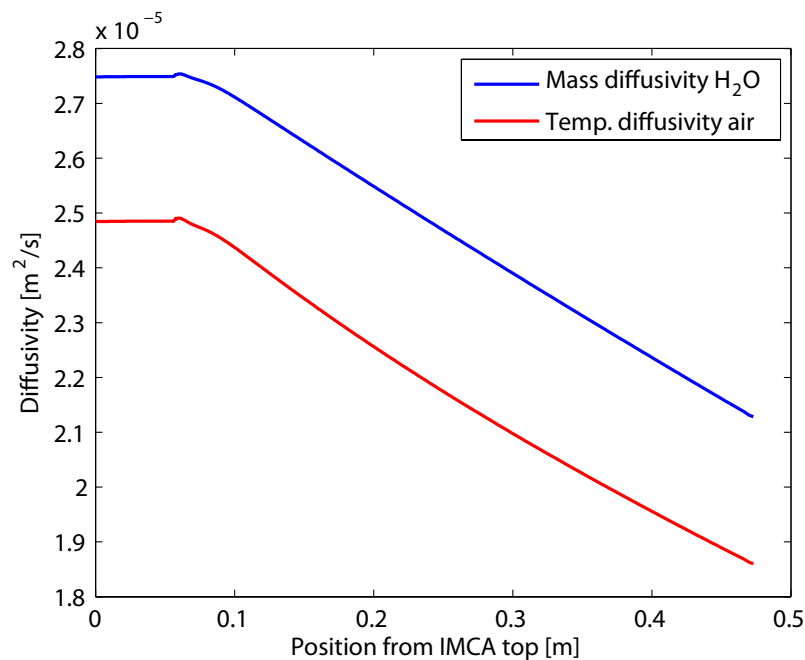

Figure 2.25: *Diffusivities of H_2O in air and temperature in air in the upper part of IMCA between the inlet section and CU1.*

The fact that water diffuses more quickly than heat can in principle be exploited in the IMCA chamber by cooling the sample air below room temperature before it enters IMCA. A temperature distribution in the inlet region for $T_{in} = 278\,\text{K}$ obtained with a FLUENT simulation can be seen in Fig. 2.26 a, where the black dashed line indicates the path along which the temperature is plotted in Fig. 2.26 b. In the FLUENT simulation, defining T_{in} involves defining the initial temperatures of the sample air, the two sheath air flows, and the head of the chamber (including the blades injecting the sample air into IMCA, cf. Fig. 2.26a.
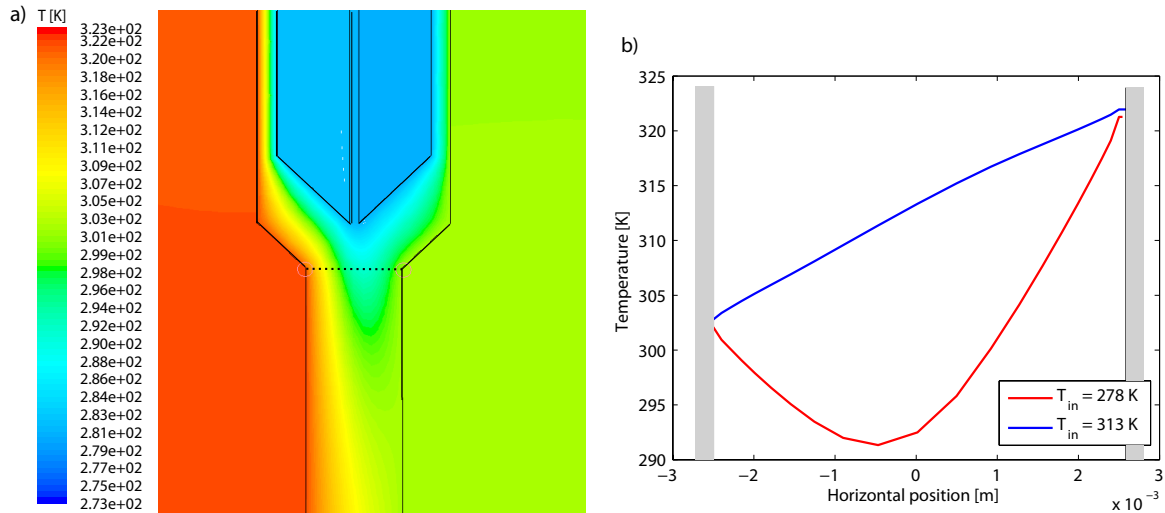
Figure 2.26: *a) Temperature distribution in the inlet section of IMCA for $T_{in} = 278$ K. The heaters at the top of the walls are set to 303 K and 323 K. b) Temperature profile between the walls at the position of the dashed line in a). $T_{in} = 278$ K leads to a distinctly concave temperature profile in the inlet section of IMCA.*

The sample air with a temperature $T_{in} = 278$ K is combined with sheath air of the same temperature and injected between the two humidified walls at 303 K and 323 K, respectively. Since the sample temperature cannot adapt to the new wall temperatures so quickly, the temperature profile lies considerably below a linear profile as in the case where the sample is injected with $T_{in} = 313$ K. This can be seen in Fig. 2.26 b. As a consequence, the supersaturation establishing just after the sample inlet must be larger than for $T_{in} = 313$ K. Calculated vertical profiles of RH_w and temperature for $T_{in} = 278$ K, $T_{in} = 293$ K and $T_{in} = 313$ K in the upper part of IMCA are shown in Fig. 2.27.

Cooling the sample (and the sheath air) to 278 K increases the supersaturation peak to a maximum value above 115%. After the maximum, RH_w quickly decreases to the value for $T_{in} = 313$ K since the sample temperature adapts to the value determined by the wall temperatures, and the horizontal temperature profile approaches a linear profile. Injecting the sample at room temperature (293 K) instead of 313 K does not have a significant effect on the supersaturation peak. The effect that the modified RH_w profile has on the droplet evolution can be seen in Fig. 2.28.

Obviously, the effect of cooling the sample and sheath air to 278 K does not have a significant effect on the droplet size, despite the increased supersaturation peak. Whereas the relative humidity in the supersaturation peak is significantly higher for a cold inlet temperature, the absolute water vapour pressure is not necessarily larger, because the saturation vapour pressure strongly depends on temperature. Figure 2.27 shows that the temperature difference between the three cases is still significant at the location of the supersaturation peak. For $T_{in} = 293$ K, droplet growth is slightly slower compared to the $T_{in} = 313$ K case, although the supersaturation is slightly larger. This sensitivity analysis suggests that, at least with the present inlet geometry of IMCA, a cooling of the sample and sheath air prior to injection is of little use to obtain larger droplets.
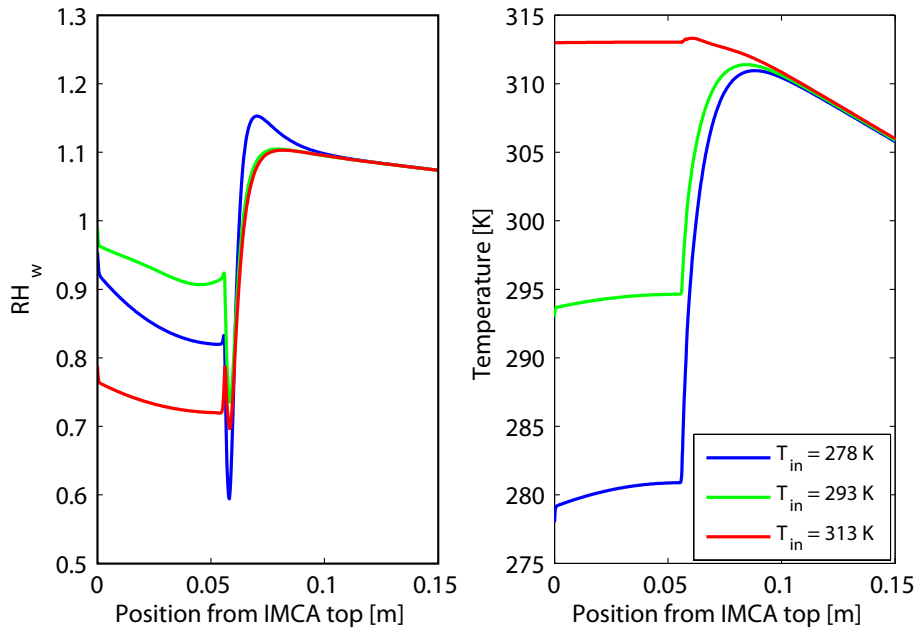
Figure 2.27: *Calculated RH_w and temperature profiles for different sample inlet temperatures. The top wall temperature difference is set to $dT = 20$ K for all cases. The sheath air inlet temperature is equal to the sample inlet temperature. For $T_{in} = 278$ K and $T_{in} = 293$ K, the sheath air is set to 100% RH_w, whereas for $T_{in} = 278$ K, only $RH_w = 80\%$ is realistic in the present experimental setup.*
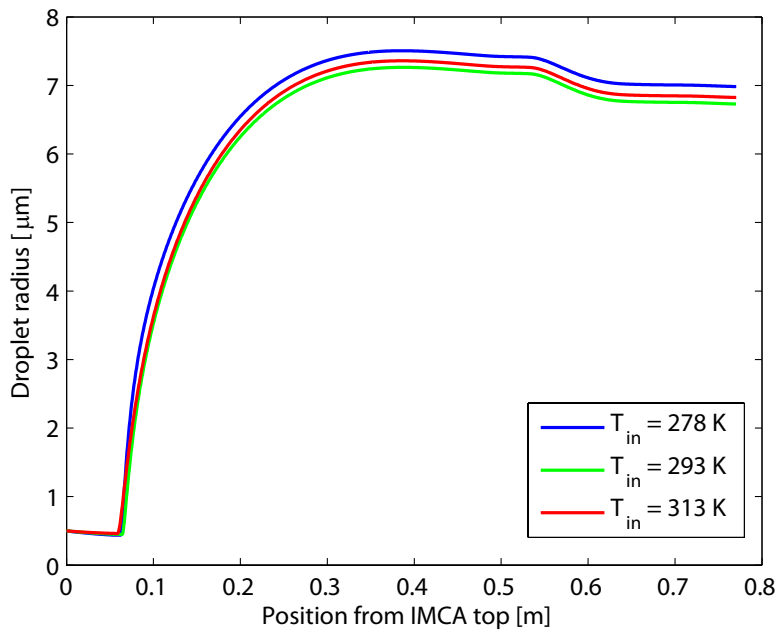
Figure 2.28: *Calculated droplet evolution for different sample and sheath air inlet temperature. The IMCA top wall heaters are set to 303 K and 323 K, respectively, and the ZINC chamber is set to 243 K.*

2.6 Water Vapour Depletion in IMCA

In all FLUENT simulations discussed so far, IMCA and ZINC are assumed to be "empty", i. e. the presence of aerosol particles or water droplets is not included in the simulation. Instead, the droplet evolution is calculated with a seperate IDL routine, based on the profiles obtained from the simulation. This raises the question if the RH_w profiles obtained with FLUENT are accurate, or if the water vapour in the supersaturated region of IMCA is depleted by growing cloud droplets. Depending on the concentration of water droplets (i. e. on the concentration of aerosol particles injected into IMCA), diffusional growth of the droplets might be a considerable sink of water vapour. A simple model is used in this section to assess the importance of water vapour depletion in the supersaturated part of IMCA. Some simplifying assumptions are made, which are illustrated in Fig. 2.29:
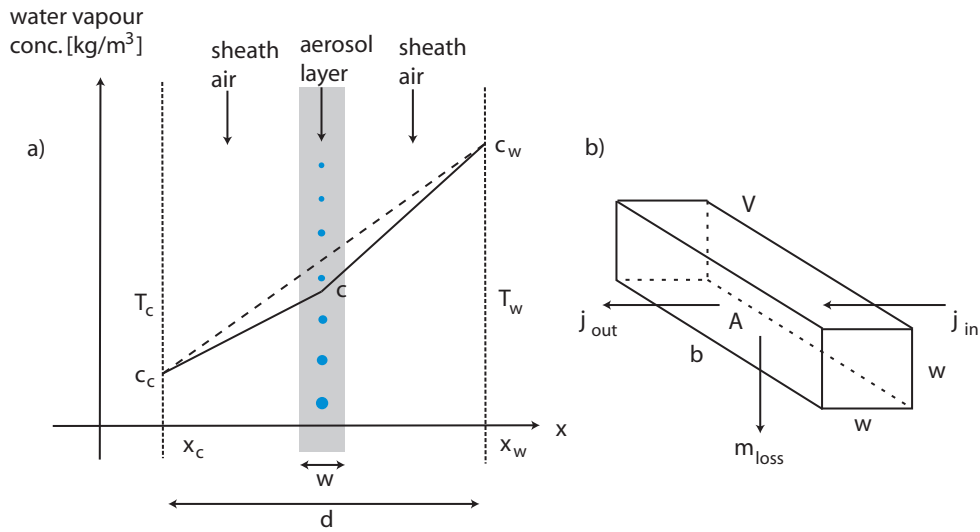
Figure 2.29: *a) Schematic of the approximated profile of water vapour mass concentration across the IMCA chamber (solid, piecewise linear profile). The dashed line represents the "undisturbed" case without water vapour depletion due to growing droplets. Vertical dashed lines represent the position of the IMCA chamber walls, and the grey shaded area indicates the aerosol layer. b) Schematic picture of the volume within the aerosol layer used to calculate a balance of water vapour mass fluxes (see text for details).*

- The mass density c of water vapour is constant over the aerosol layer (grey shaded area in Fig. 2.29).

- c follows a piecewise linear profile between the aerosol layer and each of the chamber walls.

- c and the temperature T can be assumed as constant in a brick-shaped volume V of the aerosol layer with the width w of the aerosol layer, the same height, and depth b which is equal to the depth of the chamber, $b = 30\,\mathrm{cm}$.

Based on the continuity equation, a water vapour mass flux balance can be stated for V in the aerosol layer as depicted in Fig. 2.29b. Without aerosol particles, water vapour diffuses into the volume V from the warm side, and out of V towards the cold side, represented by the mass flux densities j_{in} and j_{out}. In this case $j_{\mathrm{in}} = j_{\mathrm{out}}$. Growing cloud droplets in V give rise to a loss term m_{loss} corresponding to the water mass that the total of droplets in V gain in a time interval Δt. The mass flux balance for V can then be written as

$$\Delta m = j_{\mathrm{in}} \cdot A \cdot \Delta t - j_{\mathrm{out}} \cdot A \cdot \Delta t - m_{\mathrm{loss}}. \tag{2.47}$$

The change in water vapour mass density c within Δt in V can then be written as

$$\Delta c = \frac{\Delta m}{V} = \frac{j_{\text{in}}}{w} \cdot \Delta t - \frac{j_{\text{out}}}{w} \cdot \Delta t - \frac{m_{\text{loss}}}{A \cdot w}, \qquad (2.48)$$

since $V = A \cdot w$. For j_{in} and j_{out}, Fick's law can be used:

$$j_{\text{in}} = D_v \cdot \nabla c|_{x > x_c + d/2} \qquad (2.49)$$

$$j_{\text{out}} = D_v \cdot \nabla c|_{x < x_c + d/2} \qquad (2.50)$$

As c is assumed piecewise linear, ∇c is piecewise constant, and equations (2.49) and (2.50) can be written as

$$j_{\text{in}} = D_v \cdot \frac{c_w - c}{d/2} \qquad (2.51)$$

$$j_{\text{out}} = D_v \cdot \frac{c - c_c}{d/2} \qquad (2.52)$$

where c_w and c_c denote the mass densities of H_2O at the humidified warm and cold walls of IMCA, respectively. A relation between the mass density of water vapour c and the water vapour pressure e can be established using the ideal gas law $pV = N_{\text{tot}}RT$, i. e. $eV = N_{H_2O}RT$, where N_{tot} is the total number of moles of gas molecules in V, and N_{H_2O} is the number of H_2O molecules in V. Since $N_{H_2O} = \frac{c \cdot V}{M_w}$ with the molar volume M_w of H_2O, c can be written as

$$c = \frac{e \cdot M_w}{RT}, \qquad (2.53)$$

which can be used to replace c in equations (2.51) and (2.52) to give

$$j_{\text{in}} = D_v \cdot \frac{2M_w}{Rd} \left(\frac{e_w}{T_w} - \frac{e}{T} \right) \qquad (2.54)$$

$$j_{\text{out}} = D_v \cdot \frac{2M_w}{Rd} \left(\frac{e}{T} - \frac{e_c}{T_c} \right) \qquad (2.55)$$

where $e_w = e_{\text{sat},w}(T_w)$ and $e_c = e_{\text{sat},w}(T_c)$. The mass of water leaving V by condensation of water vapour on the droplets present in V, m_{loss}, can be written as

$$m_{\text{loss}} = c_{\text{DMA}} \cdot V \cdot dm_1 \cdot \Delta t, \qquad (2.56)$$

where c_{DMA} denotes the particle concentration in the aerosol layer (which is assumed to be the same as the one in the monodisperse sample air after the DMA), and dm_1 is the water mass that one single droplet acquires in Δt. Equations (2.54), (2.55) and (2.56) can be substituted in equation (2.48) to give

$$\Delta c = D_v \cdot \frac{2M_w}{Rdw} \left(\frac{e_w}{T_w} + \frac{e_c}{T_c} - \frac{2e}{T} \right) \cdot \Delta t - c_{\text{DMA}} \cdot dm_1 \cdot \Delta t, \qquad (2.57)$$

or, if equation (2.53) is invoked again, we obtain the change in partial water vapour pressure, Δe, during Δt due to condensation on growing droplets:

$$\Delta e = \frac{2D_v}{dw} \left(\frac{T}{T_w} \cdot e_w + \frac{T}{T_c} \cdot e_c - 2e \right) \cdot \Delta t - \frac{c_{\text{DMA}} \cdot dm_1 \cdot \Delta t \cdot RT}{M_w}. \qquad (2.58)$$

This is a discretized differential equation for e which has been solved numerically with the initial conditions

$$c(t=0) = \frac{c_w + c_c}{2}, \quad \text{i.e.} \quad e(t=0) = \frac{T}{2} \left(\frac{e_c}{T_c} + \frac{e_w}{T_w} \right).$$
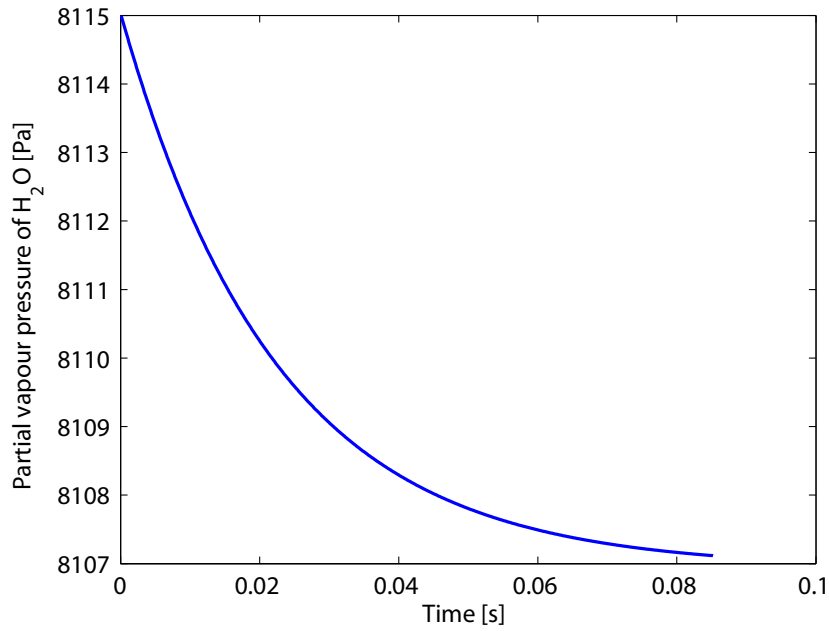
Figure 2.30: *Water vapour pressure as a function of time from the start of condensational droplet growth in the aerosol layer at a position with maximum supersaturation in IMCA. The top wall temperatures are set to 323 K and 303 K, respectively. At time t = 0, condensation of water vapour onto droplets with a concentration of* $5000\,\mathrm{cm}^{-3}$ *is enabled.*

Iterations were continued until the change in e between two iterations, relative to e itself, became smaller than 1×10^{-7}. Figure 2.30 shows the relaxation of e upon a sudden presence of growing water droplets with a concentration of $5000\,\mathrm{cm}^{-3}$.

The water vapour pressure at $t = 0$ corresponds to the "undisturbed" case without water droplets in the aerosol layer. After $t = 0$, condensational growth of water droplets is enabled and reduces the water vapour pressure until the system has relaxed to an equilibrium value after roughly 0.1 s.
In order to obtain a profile of the change in supersaturation due to droplet growth along the entire supersaturated region of IMCA, the described calculation has been done for all grid points along a droplet trajectory through the supersaturated part of IMCA, since the amount of water mass condensing on a droplet in Δt depends on the supersaturation and hence on the position in IMCA. Thus for every position, the corresponding value of dm_1 and the wall temperatures were taken from a FLUENT simulation to calculate the reduced equilibrium water vapour pressure e at that position (a standard simulation with IMCA wall top temperatures of 323 K and 303 K was used). The resulting saturation profiles are displayed in Fig. 2.31 and 2.32 for two different aerosol particle concentrations, $c_{\mathrm{DMA}} = 500\ \mathrm{cm}^{-3}$ and $c_{\mathrm{DMA}} = 5000\ \mathrm{cm}^{-3}$.

Calculation of the flow profile with a sample flow of 0.6 lpm yields a width of the aerosol layer of $w = 5 \times 10^{-4}\,\mathrm{m}$, leading to a volume $V = 7.5 \times 10^{-8}\,\mathrm{m}^3$. The time step was set to $\Delta t = 1 \times 10^{-4}\,\mathrm{s}$. Reducing the time step has no significant influence on the result of the calculation. It is obvious from Fig. 2.31 that a realistic concentration of particles in the aerosol layer (which ranges up to around 500 cm^{-3} in the present experiments) has no significant effect on the supersaturation in IMCA. The difference to the "undisturbed" case is less than 0.03% RH_w. Even a ten times larger particle concentration leads to a decrease in RH_w which is not comparable to the variations in RH_w across the sample layer due to the horizontal RH_w profile between the IMCA walls. Therefore, the conclusion can be drawn that no correction of the calculated RH_w profile in IMCA due to condensational droplet growth has to be made for any particle concentrations that can be reached with the experimental setup.
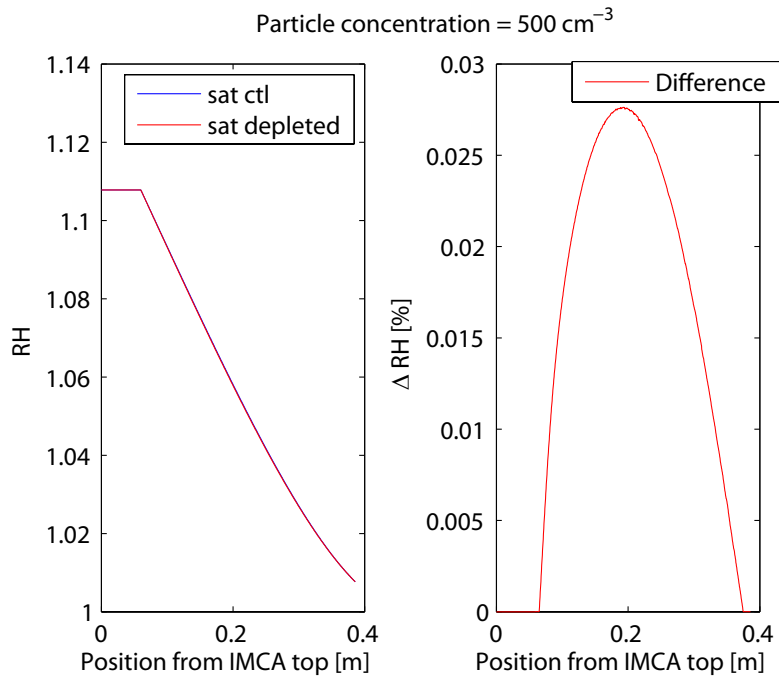
Figure 2.31: *Water vapour depletion in IMCA due to condensational growth of water droplets. The left panel shows profiles of water vapour pressure e in the supersaturated part of IMCA for the case without droplets (blue curve) and for the depleted case with a droplet concentration of $500 \, cm^{-3}$. The right panel shows the difference in % RH_w between the two cases.*
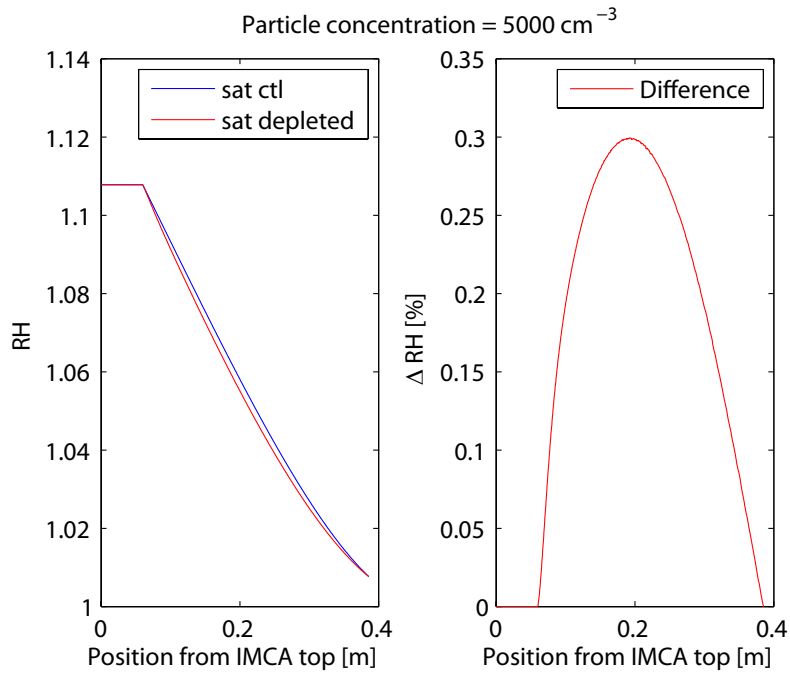
Figure 2.32: *As for Fig. 2.31, but with a droplet concentration of $5000 \, cm^{-3}$.*

Chapter 3

Experimental Study on the Ice Nucleation Ability of Size Selected Kaolinite Particles in the Immersion Mode

Authors: F. Lüönd [1], O. Stetzer[1], U. Lohmann[1]

Abstract

The newly developed Immersion Mode Cooling Chamber (IMCA) has been used as an extension of the Zurich Ice Nucleation Chamber (ZINC) in order to measure the ice nucleation efficiency of size selected kaolinite particles in the immersion mode. Particles with selected sizes of 200 nm, 400 nm and 800 nm have been activated as cloud condensation nuclei (CCN) in order to obtain droplets with single immersed particles. After continuous cooling of the droplets to the experimental temperature in ZINC, the frozen fraction of the droplets was measured with a recently developed depolarisation detector IODE (Ice Optical Detector). In the investigated size range, kaolinite particles do not appear to be particularly efficient ice nuclei (IN). Although not very strong, a size dependence of the freezing efficiency has been observed. The median freezing temperature increases from 238 K for 200 nm kaolinite particles to 240 K for 800 nm particles. The temperature dependent frozen fraction of droplets has been fitted with functions derived with different theoretical models. Best fits of the data are obtained with two models: One is based on classical nucleation theory (CNT) in combination with a surface distribution of active sites of various efficiency (represented by a contact angle α), and the other is a deterministic model attributing a distinct freezing temperature to each potential nucleating site. In contrast, a fit function based on CNT with one constant contact angle for all IN (stochastic hypothesis) cannot be used to describe immersion freezing with kaolinite particles.

3.1 Introduction

Knowledge about atmospheric ice nucleation is crucial for the understanding of the formation of precipitation and cloud radiative properties (Durant and Shaw, 2005). Field measurements have shown that formation of ice crystals in clouds can occur at temperatures well above the onset of homogeneous freezing (e. g. Hobbs and Rangno, 1985) via heterogeneous nucleation on IN. However, assessing the dependence of ice nucleating capabilities of aerosol particles on their properties remains challenging.

---

[1]ETH Zurich, Institute for Atmospheric and Climate Science, Switzerland

Complicating the description of heterogeneous ice nucleation is the fact that four different modes can be distinguished: Ice nucleation by direct deposition of water vapour on an IN (deposition nucleation), freezing of a cloud droplet with an immersed IN (immersion freezing), condensation of a supercooled cloud droplet on an IN and subsequent freezing (condensation freezing), and freezing of a supercooled cloud droplet upon contact with an IN (contact freezing). The relative importance of these heterogeneous ice nucleation modes is still not fully understood.

Measurements of ice crystal residuals have shown that clay minerals such as kaolinite, montmorillonite and illite are enriched in the center of ice crystals (Kumai, 1961; DeMott et al., 2003b). Sassen (2002) reported Asian dust to be efficient in cirrus cloud formation. Numerous laboratory studies have been conducted to assess the ice nucleation capabilities of mineral dust aerosols. Archuleta et al. (2005), Kanji et al. (2008) and Welti et al. (2009) have reported a high IN efficiency of mineral dust aerosols in the deposition mode. Heterogeneous freezing of water and solution droplets has been investigated e. g. by Niedermeier et al. (2009) and Hung et al. (2003), and in earlier studies by Pitter and Pruppacher (1973) and Hoffer (1961). They have shown that mineral dust particles act as IN in the immersion and in the contact mode (contact: see Pitter and Pruppacher (1973)), but it is also obvious from these studies that freezing temperatures measured in immersion freezing experiments depend considerably on the experimental procedure, particularly on the size of droplets and immersed particles. Besides differences in ice nucleation capability between different mineral dust types, a size dependence of IN efficiency has been reported with a tendency to higher IN efficiency for larger particles (Hung et al., 2003; Archuleta et al., 2005; Welti et al., 2009). Coating of mineral dust particles with soluble or partly soluble compounds in aging processes also influences the ice nucleation properties of aerosol particles. Depending on the coating substance, Niedermeier et al. (2009) have found a decrease of the IN efficiency of coated ATD particles compared to uncoated particles.

In the present work, we focus on the IN efficiency of size selected kaolinite particles in the immersion mode under conditions relevant for mixed-phase clouds. Unlike droplets produced from suspensions, the droplets in the present study are produced by CCN activation of the IN. This method of producing droplets with single immersed, size selected aerosol particles allows for a good knowledge of the droplet content. Furthermore, the pathway of CCN activation, subsequent cooling and freezing of droplets simulates the process of immersion freezing in the real atmosphere. In the present study, we are particularly interested in the dependence of the frozen fraction of droplets on the size of the immersed IN. The size dependence of ice nucleation properties of IN is an important parameter for modeling studies since atmospheric conditions and the distance to a natural dust source influence the size distribution of dust transported to a certain location (Welti et al., 2009). We derive fit functions for the measured frozen fraction of droplets as a function of temperature using different theoretical models. Since in general, no dependence of heterogeneous ice nucleation on the size of IN is implemented in general circulation models (e. g. Lohmann and Diehl, 2006; Morrison and Gettelman, 2008; Hoose et al., 2008), such fit functions can help to improve the parameterization of heterogeneous ice nucleation in modeling studies.

3.2 Experimental

3.2.1 Setup Overview

The setup used in the present work consists of a combination of the established Zurich Ice Nucleation Chamber (ZINC) with the newly developed Immersion Mode Cooling Chamber (IMCA) and the newly developed Ice Optical Detector (IODE) (Nicolet et al., 2008). The ZINC chamber has previously been used to study ice nucleation in the deposition mode (Stetzer et al., 2008; Welti et al., 2009). It is a parallel-plate continuous flow diffusion chamber (CFDC) based on the principle of Rogers (1988). The ice coated walls of ZINC can be cooled to individual temperatures in the main chamber such that temperature and relative humidity can be set independently. Below the main chamber an evaporation section at ice saturation usually evaporates water droplets nucleated in the main chamber at conditions above water

saturation. In a typical ZINC experiment, dry aerosol particles are injected into ZINC and channeled in the center of the chamber by two sheath air layers. An optical particle counter (OPC) is used to infer the fraction of particles that nucleate ice at the prevailing temperature and supersaturation. For more details about the ZINC chamber, see Stetzer et al. (2008). For the present experiments, ZINC has been vertically extended by the IMCA chamber. Also, the evaporation section has been removed and replaced by a short lower section (20 cm in length) to avoid evaporation of droplets prior to their detection. An overview schematic of the setup is shown in Fig. 3.1.
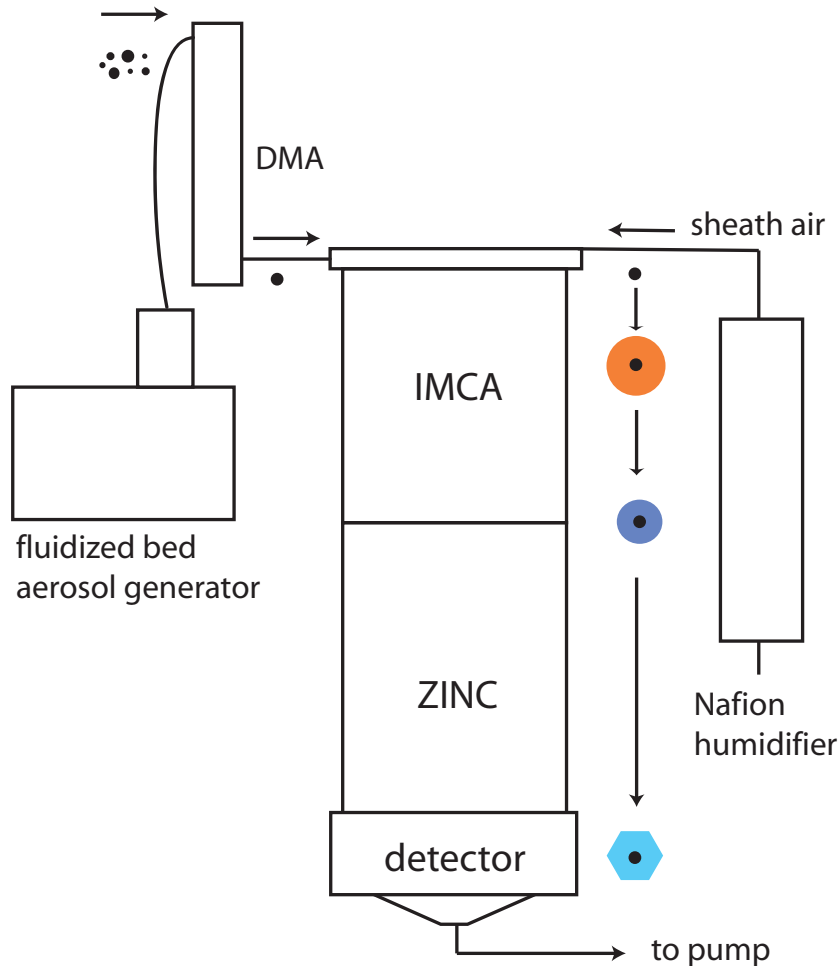
Figure 3.1: *Overview of the experimental setup. Size selected kaolinite particles are activated to cloud droplets (red droplet) and cooled to ZINC temperature (blue droplet) in IMCA. The frozen fraction of the droplets is measured at the end of ZINC with the IODE detector.*

Airborne IN are generated with a fluidized bed aerosol generator (TSI 3400A) and size selected with a differential mobility analyzer (DMA, TSI 3081) before they enter the IMCA chamber. IMCA activates the particles into cloud droplets and continuously cools them to the experimental temperature maintained in ZINC which is set to a relative humidity close to water saturation. This prevents the droplets from evaporating before they freeze. At the end of ZINC, the IODE detector is used instead of an OPC to measure the frozen fraction of the droplets as a function of the experimental temperature.

3.2.2 The IMCA Chamber

A detailed schematic of the IMCA chamber is shown in Fig. 3.2.
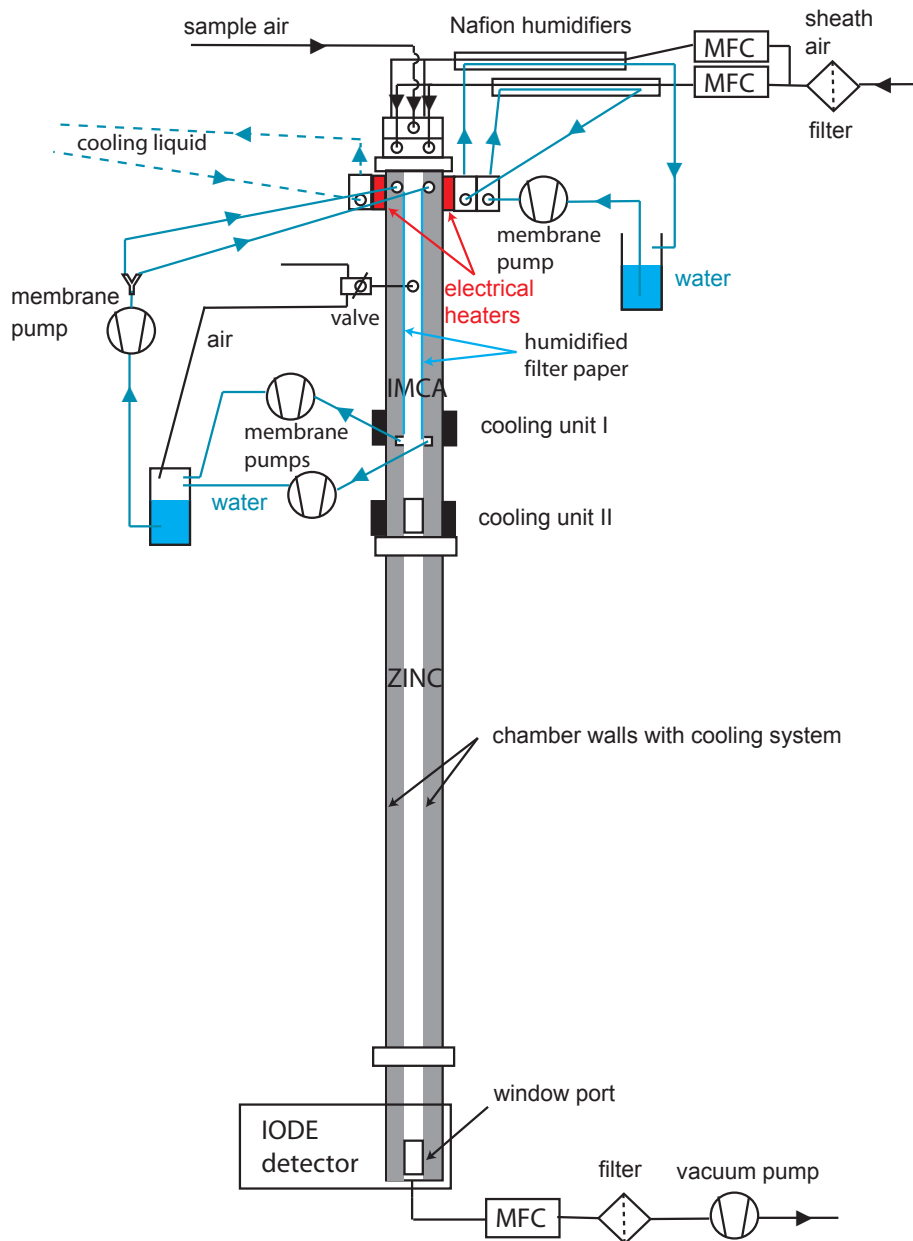
Figure 3.2: *Schematic of the IMCA chamber (side view). Chamber walls are grey shaded. See text for details.*

IMCA is a 66 cm long, vertical extension of ZINC with the same parallel plate geometry. It establishes both a vertical and horizontal temperature gradient: The uppermost part is heated by electrical heaters to temperatures suitable for the nucleation and diffusional growth of cloud droplets, whereas the lower part is cooled with two cooling units to establish the streamwise temperature gradient which cools the cloud droplets continuously down to the temperature prevailing in ZINC. Aerosol particles are injected with the sample air in the top of IMCA and are combined with sheath air layers humidified at the top temperature of IMCA. In order to obtain the required supersaturation to nucleate and grow cloud droplets, the walls are humidified by wet filter papers, and different temperatures are applied to

the electrical heaters. This leads to a second, horizontal temperature gradient between the walls. Due to the non-linear temperature dependence of the saturation vapour pressure this leads to a supersaturation profile between the walls with a maximum approximately in the center of the chamber where the aerosol flow is located (for details about the saturation profile between the walls of a CFDC see Stetzer et al. (2008)).

The filter papers are permanently supplied with water, with any excess water being pumped out of the chamber at the end of the filter papers at the vertical position of cooling unit 1 (CU1). This unit defines the transition between the warm part of IMCA (above 273 K) and the cold part (below 273 K), therefore both chamber walls are set to 273 K at this position. Cooling unit 2 (CU2) cools the lowermost part of IMCA to the ZINC wall temperatures. Between CU1 and CU2, the chamber walls are coated with ice. The icing procedure is done prior to the experiments, and no water supply is necessary in this part throughout an experiment.

A calculated example of a typical vertical temperature and saturation profile of IMCA obtained in a computational fluid dynamics (CFD) simulation with FLUENT is shown in Fig. 3.3.
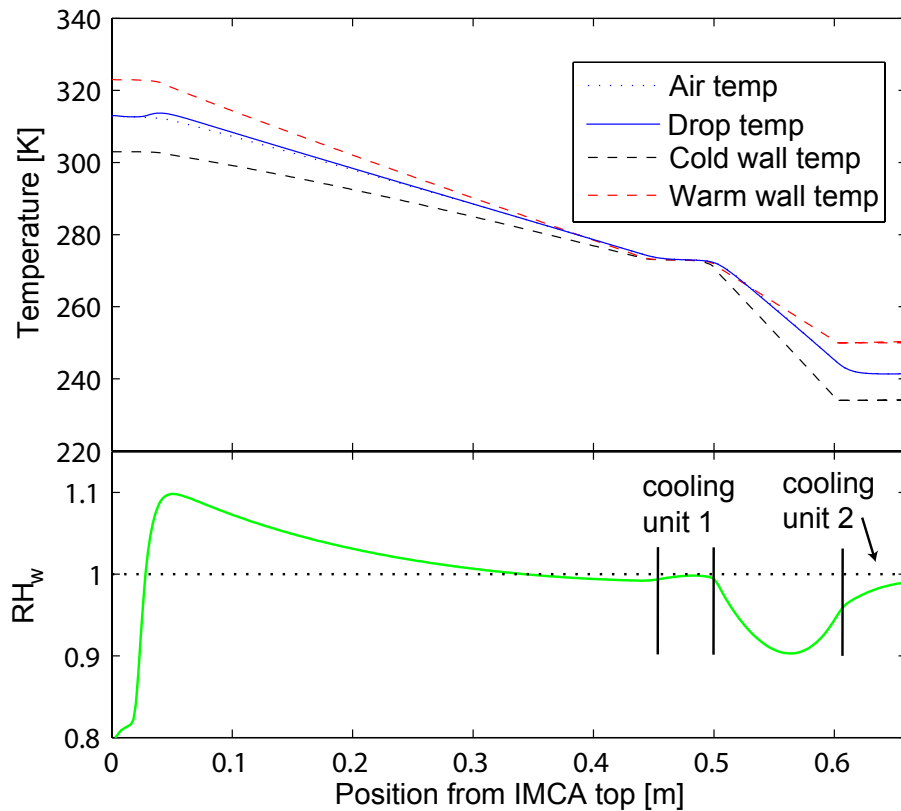
Figure 3.3: *Upper panel: Vertical profile of temperature in the IMCA chamber. Dashed lines indicate the wall temperatures, the dotted line denotes the sample air temperature, and the solid line represents the droplet temperature. Lower panel: Profile of RH_w at sample position. As the humidified chamber walls are heated to different temperatures at the top of IMCA, a supersaturation peak establishes. Note that due to latent heat release during diffusional growth, the droplet temperature is slightly higher than the air temperature. Between cooling unit 1 and cooling unit 2, ice coating of the chamber walls leads to subsaturation with respect to water.*

The sample temperature at the top of IMCA was set to 40°C with a top wall temperature difference of 20°C, and the experimental temperature in ZINC was set to −30°C. The x-axis denotes the distance from the particle inlet section down the chamber. After 66 cm, the droplets reach the end of CU2 and enter the

ZINC chamber. The saturation profile displays a pronounced supersaturation peak close to $RH_w = 110\%$ after the particle inlet where the horizontal wall temperature difference is at maximum. The slightly subsaturated area above CU1 is due to the decreasing temperature of the sample air for increasing x in connection with the fact that water diffuses more quickly than heat. A more substantial decrease in RH_w occurs between CU1 and CU2 because the water vapour pressure over the ice coated walls is lower than water saturation. However, since the wall temperatures in CU2 are equal to the ZINC wall temperatures, RH_w increases again towards the lower end of IMCA and reaches the ZINC value slightly below water saturation (we choose to operate ZINC between 99% and 100% RH_w rather than at or above water saturation to avoid condensation freezing in ZINC).

In order to find a suitable geometry for the IMCA chamber that allows for sufficient droplet growth before the droplets enter the subsaturated lower part of IMCA, calculations of diffusional growth and evaporation of water droplets have been carried out using the temperature, RH_w and flow velocity profiles obtained from the FLUENT calculations. A ratio of 3:1 between the lengths of the warm and the cold section of IMCA allows for sufficient diffusional growth that the droplets can travel through the lower part of IMCA and through ZINC without excessive mass loss due to evaporation. Accordingly, IMCA was constructed with this length relation. Both the wall temperature difference and the sample temperature in the top part of IMCA influence diffusional growth of droplets. On one hand, the efficiency of diffusive transport increases with increasing temperature. On the other hand, the peak supersaturation obtained in the top part of IMCA for a fixed wall temperature difference decreases with increasing temperature. Whereas for top temperatures larger than 40°C these effects roughly cancel out, a top temperature of 30°C would lead to larger droplets at the lower end of IMCA for the same wall temperature difference of 20°C. However, this difference is technically more difficult to maintain at lower temperature as the top of the cooler IMCA wall can only be cooled with water at room temperature in the present setup. Therefore, a sample temperature of 40°C has been used throughout the experiments.

FLUENT simulations have shown that a distance of 0.5 cm between the walls, as used in IMCA, leads to a better adaptation of the sample air to the wall temperatures than a distance of 1 cm as in ZINC. The larger the distance, the more the difference between the sample temperature in the center of the chamber and the average of the wall temperatures at the corresponding vertical position for a fixed flow velocity. According to the FLUENT simulation, this difference can reach up to around 3°C maximum in the present experiment. The total flow rate of the sample air combined with the sheath air has been reduced to 5 lpm compared to 10 lpm in a ZINC experiment because the increased residence time of the droplets in IMCA leads to larger droplet sizes. The residence time in the IMCA chamber with 5 lpm total flow is around 8 seconds. The total flow consists of 0.6 lpm of sample air combined with 4.4 lpm of humidified sheath air.

3.2.3 The IODE Detector

Experiments on immersion freezing in a CFDC require the destinction between airborne frozen and unfrozen droplets. In the present experiments, we have used the recently developed depolarisation detector IODE. As a detailed description of IODE can be found in Nicolet et al. (2008), we just summarize the most important points. IODE has been designed to measure the depolarisation of linearly polarized incident laser light by ice particles and water droplets in cloud chambers. The laser beam crossing the chamber in the center between the walls is tilted by 3° with respect to the horizontal plane which allows for detection of light scattered under an angle of 177°. A Wollaston prism splits the scattered light into its components of parallel and perpendicular polarisation with respect to the polarisation of the incident light, and two photomultiplier tubes (PMT) detect the intensity in each channel. Some improvements have been done to the original version of the detector described in Nicolet et al. (2008), whereas the working principle has remained the same. IODE has been designed for single particle detection, therefore a peak detection algorithm is used to find intensity peaks from individual particles in the backscattered signal. The signal amplitudes at a peak location are used to calculate the depolarisation

ratio according to

$$\delta = \frac{I_\perp}{I_\parallel + I_\perp} \qquad (3.1)$$

(Nicolet et al., 2008), where $I_\perp$ and $I_\parallel$ are the signal intensities (with the background signal subtracted) in the perpendicular and the parallel channel, respectively. Nicolet et al. (2008) report an interaction time around 6 ms of a particle with the laser beam which in the present experiments increases to 12 ms due to the reduced total flow rate of 5 lpm. In order to avoid false peaks originating from noise at a frequence higher than around 80 Hz (which corresponds to a peak width of 12 ms), a 80 Hz lowpass filter is applied to the raw signal.

The depolarisation ratio of a scattered signal peak is a proxy for the asphericity of the corresponding particle. The asphericity of a hydrometeor itself can be used to discriminate between the liquid and the ice phase. Whereas spherical particles like water droplets theoretically do not depolarize the incident light, δ increases with increasing particle asphericity in a first approximation. However, Nicolet et al. (2007) showed from simulations of idealized ice particles that the measured depolarisation can also significantly depend on the orientation of a particle. One specific ice crystal can therefore cover a significant range of depolarisations depending on its orientation with respect to the incident laser beam. It has to be noted that even a perfectly spherical water droplet cannot be expected to yield zero depolarisation in a real measurement due to imperfections in the system (like imperfect polarisation of the incident laser or imperfections or slight misalignments of optical elements). From these considerations one has to conclude that it might be difficult in some cases to unambiguously assign liquid or ice phase to a particle with a small depolarisation ratio. Especially for small frozen water droplets a low asphericity could lead to a small depolarisation ratio. In fact, depolarisation histograms from the present experiments do not exhibit two distinct modes for water and ice particles. Instead, a depolarisation threshold τ_δ has to be defined above which a measured particle is considered an ice crystal.

To determine this depolarisation threshold, a test experiment was performed at ZINC temperatures above 0°C where no freezing of activated droplets could occur. In this experiment $\tau_\delta = 0.07$ appeared to be the minimum threshold such that no ice crystals were detected among the water droplets. Too high values of τ_δ bear the risk of miscounting ice crystals as water droplets. However, ice crystals nucleated in the deposition mode usually yield ice fractions above 95% with $\tau_\delta = 0.07$. Therefore we assume that $\tau_\delta = 0.07$ is a reasonable choice for our setup. Before calculating the frozen fraction f of the droplets, background counts measured with particle free sample air are subtracted from the measured number of total and ice counts. Background counts can originate from ice crystals nucleating on the chamber walls which can grow and eventually fall through the detection volume of IODE. Whereas at the beginning of an experiment, background counts are often negligible, they can significantly influence the fraction of ice particles measured with IODE after 2-3 hours of supersaturation in ZINC. Therefore, a new background measurement with particle free sample air is taken after every two measurements in an experiment.

3.2.4 Kaolinite Samples

All experiments were performed with industrial kaolinite ($Al_2Si_2O_5(OH)_4$) purchased from Fluka. As the size selection with a DMA is not directly based on the particle size, but on the electrical mobility, multiple-charged particles can make it difficult to obtain a sample of monodisperse particles. A neutralizer with a polonium 210 radioactive source is used to give the particles a charge distribution with most particles being single charged. However, with increasing particle size the probability of multiply charged particles increases. These particles can have the same mobility with a higher mass than the actually selected, single charged particles. Depending on the size selected, the contribution of larger, multiply charged particles in the "monodisperse" sample can be significant. In general, this is the case for sizes smaller than the median size of the total size distribution, since multiple-charged larger particles are present in large amounts. For sizes well above the median size of the total size distribution the contribution of multiple charges is negligible.

The size selection of the particles used in the present experiments has been tested by measuring a

size distribution of the size selected aerosol with a Scanning Mobility Particle Sizer (SMPS) including a second DMA. This has been done for the sizes 200 nm and 400 nm. The measured size distributions are shown in Fig. 3.4.
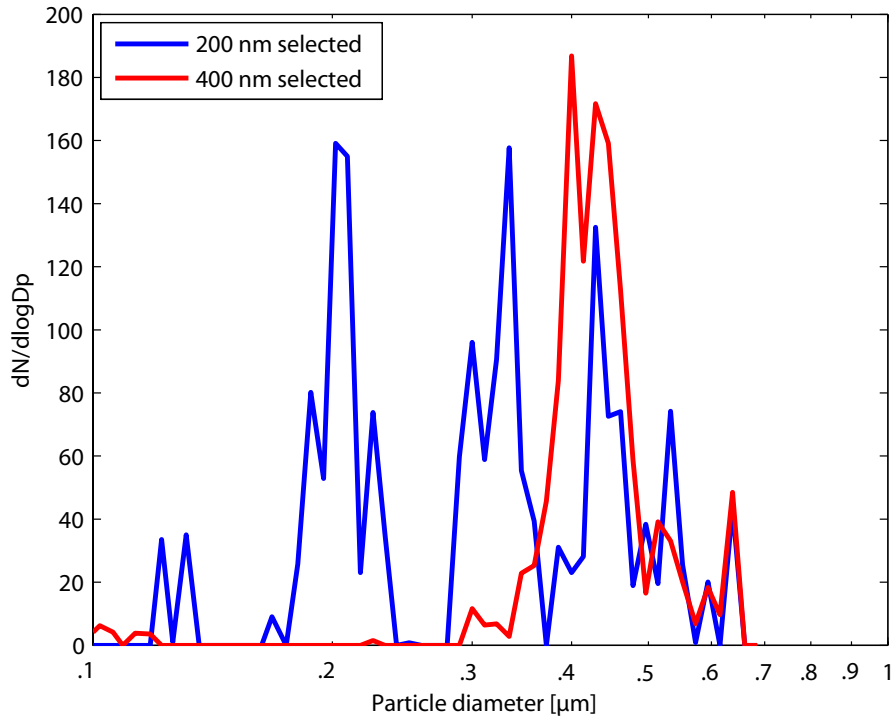
Figure 3.4: *Size distributions of size selected kaolinite particles. Sizes were selected with a DMA, and a size distribution of the resulting sample has been taken with a SMPS for selected sizes 200 nm and 400 nm. The size distribution for 400 nm particles has been scaled down in order to have similar peak values for both distributions.*

The fact that the size distributions are not smooth functions is mainly due to a relatively low particle concentration in the size selected sample. Since the SMPS can only scan up to sizes close to $1\,\mu$m at a low sample flow rate, the sample had to be diluted by filtered air in order to keep the required total flow rate of 1 lpm at the condensation particle counter (CPC) of the SMPS. The size distribution of selected 200 nm particles clearly shows that size selection with the DMA does not yield a monodisperse sample at this particle size. Peaks at larger sizes originate from multiply charged particles with the same electrical mobility and make a considerable part of the size selected sample. Inspection of the raw counts yields a fraction of 52% of real 200 nm particles, whereas 32% of the selected particles have a diameter around 330 nm, and 16% are 400 nm or larger. The fraction of multiple charges is much less pronounced for selected 400 nm particles since particles larger than 400 nm are only present in small amounts. In the following, size selected 200 nm particles including all multiply charged larger particles will be termed "200 nm particles" for simpliticy.

The number concentration of particles in the sample air has to be low enough to allow for single particle detection with IODE. Tolerable particle concentrations have been determined by visual inspection of the total signal (i. e. the sum of the parallel and the perpendicular channel), zoomed to a level where single particle peaks are well visible. The particle concentrations determined in that way and used in the experiments significantly depend on the particle size. Whereas for 200 nm particles, concentrations around 500 cm^{-3} were used, we did not exceed 60 cm^{-3} for 800 nm particles. This indicates that in general not all particles reach the IODE detector immersed in a detectable droplet or ice crystral, but

that some of them reach the detector as bare aerosol particles or at least close to their original size. The fraction of such "unactivated" particles appears to be larger for smaller sizes. Unactivated particles do not induce sufficient scattering to be detected by IODE. Nicolet et al. (2007) report that 500 nm particles are below the detection limit, and in the present study, we have compared the background counts from particle free sample air with the number of particles detected when 800 nm particles were present without droplet or ice nucleation. As this test experiment did not yield a significant increase of particle counts in the presence of 800 nm particles, we conclude that all aerosol particle sizes used in the present experiments are below the detection limit of IODE.

3.3 Results

We have performed experiments with size selected 200, 400 and 800 nm kaolinite particles in the following manner: After icing of ZINC and the lower part of IMCA, ZINC is cooled to the lowest temperature of the experiment and the wall temperatures are set to obtain $RH_w = 99.5\%$ in ZINC. At the same time, the top part of IMCA is heated to 40°C with both walls at equal temperatures. After switching on the particle flow through the chamber, the saturation in the warm section of IMCA is increased to $RH_w = 110\% - 115\%$ in order to start CCN activation of the particles. When the activation is well established, the fraction of frozen droplets, f, is measured with the IODE detector. The supersaturation in IMCA is turned down again, and ZINC is set to the next higher experimental temperature. Temperature steps are usually 0.5°C to 1°C at lower temperatures depending on how steeply f increases with decreasing temperature. At higher temperatures f weakly depends on temperature, and the temperature steps are increased to 2°C or even 4°C. Data points are taken until f has decayed to zero or does not depend on temperature anymore. The experiment is performed 4–5 times for each particle size, so as to obtain statistically more significant data.

3.3.1 Immersion and Deposition Freezing

The time series in Fig. 3.5 displays a detailed view on a typical experiment with 800 nm particles.

The top panel shows the wall and temperatures in ZINC, and panel 2 shows calculated RH_w curves of ZINC (blue) and IMCA(red). Panels 3 and 4 display measurements obtained with IODE: The red curve in panel 3 shows the number of particles detected as ice crystals with a time resolution of 0.5 s, whereas the blue curve shows the same for water droplets. Panel 4 displays a timeseries of the depolarisation of ice crystals averaged over a 0.5 s interval. Until 1200 s on the time axis, the experiment is in the cooling phase. The warm wall has reached its equilibrium temperature, whereas the cold wall is still decreasing in temperature. The sample temperature therefore decreases while the relative humidity increases (blue curve in panel 2). Note that the sample temperature is not the average of both wall temperatures because buoyancy on the warm wall leads to a shift of the aerosol layer towards the cold wall. During this cooling period the ice counts measured by the IODE detector (red curve in panel 3) are nucleated in the deposition mode, as there is no supersaturation, i. e. no cloud droplet activation in the IMCA chamber. Accordingly, almost no particles are identified as water droplets. With decreasing temperature and increasing RH in ZINC, the fraction of IN nucleating ice via the deposition mode increases.

Shortly after $t = 1100$ s, RH in the warm section of IMCA starts increasing. As a consequence, the ice counts are drastically reduced at first, meaning that deposition nucleation is suppressed by the supersaturation in IMCA. At the beginning of an IMCA activation, droplets start to nucleate but do not grow large enough to reach the ZINC chamber without evaporating. Nevertheless, some remaining liquid water might block ice nucleating sites on the aerosol particles and thus make them unavailable for deposition nucleation. With increasing IMCA supersaturation, a minimum in the ice counts is reached which is followed by a steep increase. A significant increase in the droplet counts, however, can only be seen with a delay at roughly $t = 1300$ s. Whereas there is little doubt that the delayed arrival of droplets at the detector is due to the fact that a minimum IMCA supersaturation is required such that liquid droplets
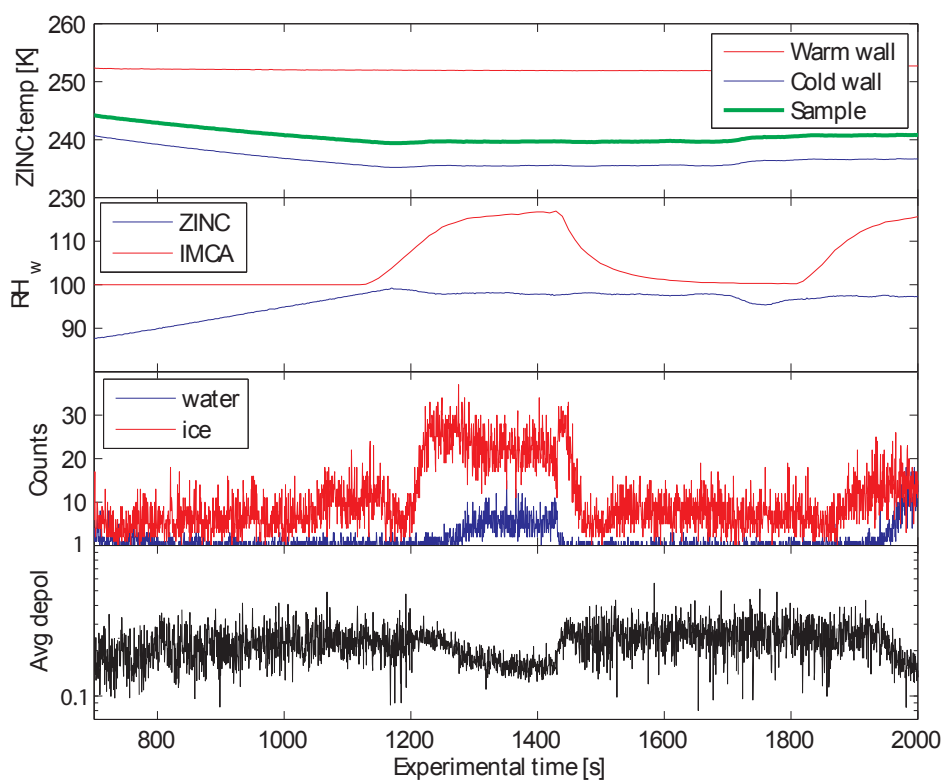
Figure 3.5: *Detailed view of a timeseries of a typical experiment with 800 nm kaolinite particles. Top panel: Wall and sample temperatures in ZINC; panel 2: Calculated RH_w in ZINC and IMCA; panel 3: Number of ice crystals and water droplets detected by IODE within a time interval of 0.5 s; panel 4: Depolarisation of ice crystals averaged over 0.5 s.*

do not evaporate in the subsaturated regions of IMCA and ZINC, the transient processes between the steep increase of the ice counts and the arrival of liquid droplets remain somewhat speculative. It is possible that when droplets grow large enough in the warm section of IMCA to reach the ZINC chamber, one part of them freezes, but the other part is too small to survive the slight subsaturation in ZINC until the detector is reached. These evaporating droplets leave aerosol particles which might partly get active in the deposition mode. Only at higher IMCA supersaturations, liquid droplets reach the end of ZINC, and no deposition nucleation can take place anymore. This would explain the slight decrease of ice counts parallel to the increase in droplet counts.

An alternative explanation could be the concept of contact nucleation inside out: Durant and Shaw (2005) found the freezing temperature of evaporating droplets to be increased by around $3°C$ when the immersed IN came into contact with the droplet surface. Although the droplet and IN sizes used in the study of Durant and Shaw (2005) are unrealistic for cloud droplets, and it is therefore questionable if these findings are representative for the present study, they can also provide a possible explanation for the decreasing frozen fraction f of droplets with increasing IMCA supersaturation (i. e. increasing droplet size). With decreasing IMCA supersaturation shortly after $t = 1400$ s, an inverse behaviour of ice and water counts can be observed with decreasing droplet counts and increasing ice counts at the same time. Also, a minimum in the ice counts is reached before deposition nucleation is no longer suppressed by IMCA supersaturation. This pattern has been observed in most IMCA activations at frozen fractions $f > 50\%$.

In order to determine the frozen fraction of droplets in one activation, it is necessary to wait until

66

the IMCA supersaturation is fully established and the conditions are at equilibrium. In Fig. 3.5, data between $t = 1300$ s and $t = 1400$ s can be used to determine f. Looking at panel 4 in Fig. 3.5, a decrease in the depolarisation of the ice counts can be clearly seen between $t = 1200$ s and shortly after $t = 1400$ s, where droplets are nucleated in IMCA. This suggests that ice crystals nucleated in the immersion mode depolarize light to a smaller degree than ice crystals nucleated in the deposition mode, which is probably due to a smaller asphericity of ice crystals originating from frozen droplets.

3.3.2 Temperature and Size Dependence of f

Plots of the measured temperature dependence of the frozen fraction f of droplets for the three particle sizes investigated are shown in Fig. 3.6, 3.7, and 3.8.
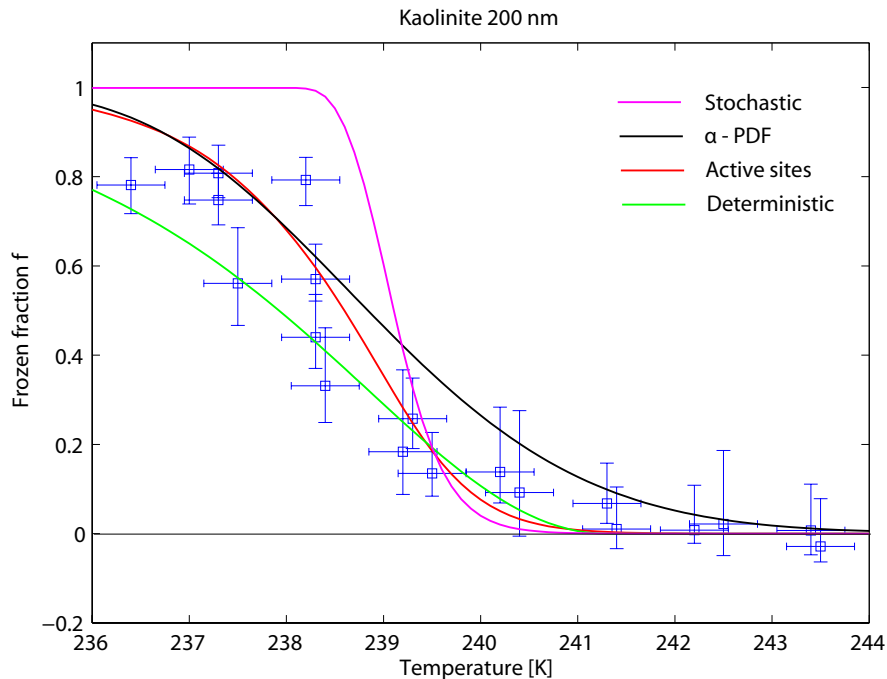
Figure 3.6: *Frozen fraction f of droplets as a function of temperature for immersed* 200 *nm kaolinite particles. Solid lines show fit curves obtained with different functions for f derived from nucleation theory with different assumptions concerning the stochastic or deterministic nature of the ice nucleation process. See text for details.*

One data point corresponds to one activation event as shown in Fig. 3.5. Solid lines represent fit curves which will be discussed in section 3.4. The measurements show that a small ice fraction usually remains at higher temperatures, whereas one would expect f to decay to 0. As has been shown in Fig. 3.5, deposition nucleation is suppressed in an activation event with IMCA. However, it cannot be seen from the time series if the contribution of deposition nucleation decays to zero, or if a small contribution remains throughout the experiments, given the temperature is low enough for deposition nucleation to be active. We have assumed that the latter is the case, and therefore we have subtracted the ice counts at the minimum before the steep increase at the lowest experimental temperature for every particle size. As the efficiency of deposition nucleation decreases with increasing temperature, this deposition contribution does not represent the exact value for all temperatures. However, it can be taken as the maximum possible ice counts originating from deposition nucleation. The remaining ice counts can then be assigned to immersion freezing alone. Data points with $f < 0$ are due to the subtraction of a too high deposition contribution at the higher temperatures. The same is true for errorbars reaching to values below $f = 0$.

Figure 3.7: *Same as Fig. 3.6 with* 400 *nm instead of* 200 *nm particles*

Errorbars are determined as follows: The horizontal errorbars represent the uncertainty in the experimental temperature. As the ZINC walls are set to different temperatures, a temperature gradient exists across the aerosol layer in the chamber. From the wall temperature difference and the width of the aerosol layer, a maximum temperature difference within the sample can be calculated and taken as the temperature uncertainty of the measurement. Throughout the covered temperature range, this ΔT has 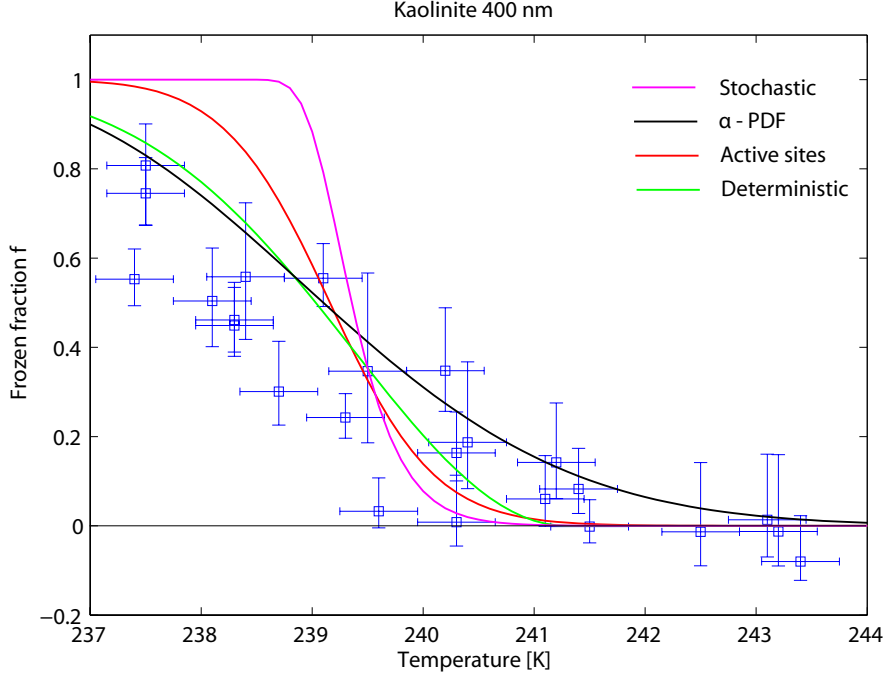a value of approximately 0.7 K. Vertical error bars represent an uncertainty in f due to measurement errors of the IODE detector. Due to electronic noise, there is an error in both quantities $I_\perp$ and $I_\parallel$ measured by IODE. With the depolarisation δ given in equation 3.1, the error in δ can be calculated via error propagation. The result is

$$\Delta\delta = \frac{1}{(I_\parallel + I_\perp)^2} \sqrt{I_\parallel^2 (\Delta I_\perp)^2 + I_\perp^2 (\Delta I_\parallel)^2}, \tag{3.2}$$

where for the measurement errors $\Delta I_\perp$ and $\Delta I_\parallel$ the standard deviations $\sigma_\perp$ and $\sigma_\parallel$ of the background signal have been taken. $\Delta\delta$ has negligible impact for particles with a depolarisation well below or well above the depolarisation threshold τ_δ. However, a particle with δ slightly below τ_δ can be miscounted as an ice crystal if $\delta + \Delta\delta > \tau_\delta$, and vice versa. Therefore, the number of potentially miscounted ice crystals in one activation subtracted from the measured ice counts yields the lower errorbar. Similarly, the number of potentially miscounted water droplets yields the upper errorbar.

3.3.3 Discussion

Small kaolinite particles with sizes between 200 and 800 nm do not appear to be very efficient IN in the immersion mode. Temperatures below 243 K are required to freeze 50% of the droplets. A size dependence of the IN efficiency is clear when comparing Fig. 3.6 to Fig. 3.8. Whereas a frozen fraction of 50% is reached around 238 K for both 200 and 400 nm particles, $f = 0.5$ is reached at 240 K for 800 nm particles. Pitter and Pruppacher (1973) reported considerably larger values for the median freezing temperature T_m (250 K) for kaolinite in wind tunnel studies. However, their experimental methods are different, and they investigated droplets as large as $300 \mu m$ containing particles up to $30 \mu m$ in
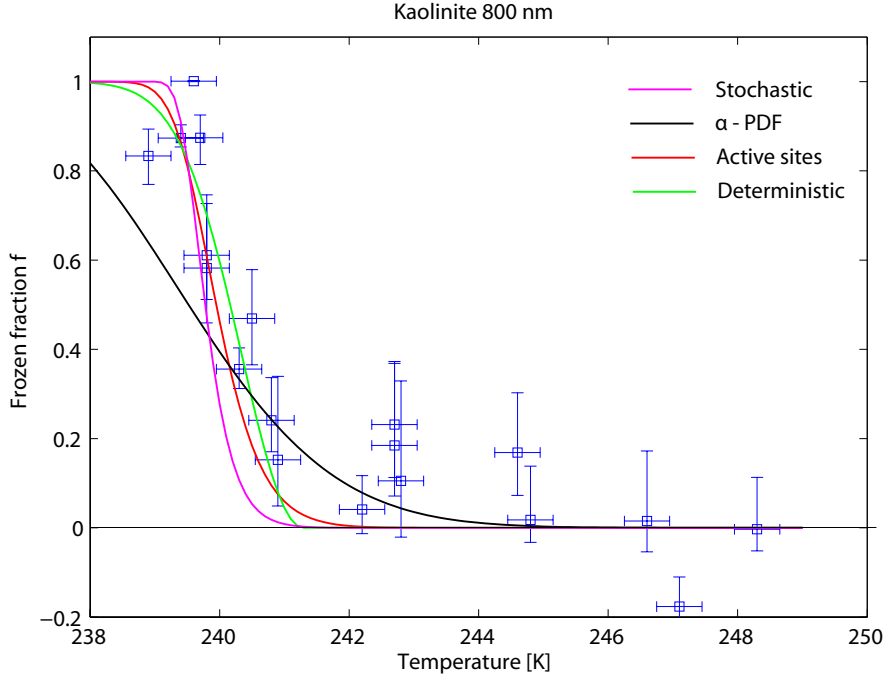
Figure 3.8: *Same as Fig. 3.6 with* 800 *nm instead of* 200 *nm particles*

diameter. Our findings are closer to those of Hoffer (1961) who reported median freezing temperatures of 240.5 K for $100 - 120\,\mu m$ kaolinite suspension droplets supported in a silicone oil matrix.

The difference between 200 nm and 400 nm is less pronounced. This is not unexpected in view of the fact that a sample of size selected 200 nm particles contains a considerable amount of particles with a diameter close to 400 nm, as discussed in section 3.2.4. Whereas the experiments with 200 nm and 800 nm particles were usually reproducible within the errorbars, there is significantly more scatter in the data for 400 nm. The reason for this scatter is unclear, but it is probably due to problems in adjusting the detector optics during these experiments. Although the onset of freezing for 200 nm particles is clearly above the onset of homogeneous freezing, it might be that homogeneous nucleation starts to contribute to the frozen fraction at the lowest experimental temperatures. Marcolli et al. (2007) have reported the onset of homogeneous freezing for $2.4\,\mu m$ and $10\,\mu m$ droplets to be 236.5 K and 237.4 K, respectively. We expect the droplets in the present experiments to be between these sizes, i. e. some droplets freezing via homogeneous nucleation is realistic at 237 K.

There are several possible sources of errors in the present experiments. Uncertainty arises from the fact that a depolarisation threshold τ_δ needs to be defined to discriminate between water droplets and ice crystals. Given the value of τ_δ is correct, the error in f arising from the measurement error of the signal intensities has been calculated as described in section 3.3.2. It has to be assumed that there is also some uncertainty to the value of τ_δ which has been determined in test experiments. This uncertainty, however, is difficult to quantify. Instead, we give an estimate of the sensitivity of f to τ_δ. For an activation with 200 nm particles at $T = 237.3 \pm 0.35$ K, f varies between 0.79 and 0.86 upon varying τ_δ by ± 0.01 around the used value of $\tau_\delta = 0.07$. At $T = 238.3 \pm 0.35$ K, the same variation in τ_δ results in a variation of f between 0.44 and 0.54, and at $T = 243.5 \pm 0.35$ K between 0.04 and 0.1. The sensitivity of f to τ_δ is similar for the entire range of f between 0 and 1. Although variations in f due to an uncertainty in τ_δ are considerable, the effect on the median freezing temperature T_m (i. e. where 50% of the droplets are frozen) is rather moderate. Taking an uncertainty of ± 0.01 for τ_δ as realistic, the uncertainty in T_m due to an uncertainty of 0.1 in f can be estimated as less than 1 K since the dependence of f on T is larger than 0.1/K. A further uncertainty arises from a contribution of ice crystals nucleated in the deposition mode. Although calculations of diffusional growth and evaporation of droplets in the IMCA chamber predict

that droplets nucleated in the warm section of IMCA grow large enough not to evaporate in the subsaturated regions of IMCA and ZINC, there are indications that a fraction of unactivated aerosol particles could be present in ZINC during an activation event. This can be due to simplified assumptions made in the calculations. An assumption that might not be realistic is that RH_w in the ZINC chamber is equal for all droplets. Due to the finite width of the sample air layer in ZINC, RH_w can vary by around $2-3\%$ over the width of the sample air layer. Wall temperature inhomogeneities could also influence RH_w in ZINC and lead to droplet evaporation different from the evaporation expected from the simulation.

As ice crystals detected by IODE cannot a priori be discriminated between ice crystals nucleated in the deposition mode and crystals nucleated in the immersion mode, a maximum possible contribution from deposition nucleation has been subtracted from the measurements as explained in section 3.3.2. The effect of this subtraction is not very significant for large f, but makes a difference up to 0.1 in f for small values of f, or even 0.2 for some data points in the 400 nm experiments. Whereas this correction probably works quite well to isolate the immersion freezing mode for large frozen fractions f, some error is certainly introduced for higher temperatures. This becomes manifest in the values of f falling below 0 after the correction.

3.4 Fit Curves for f

In order to make the presented data useful for parameterisations of immersion freezing in modeling studies, we have tested several theoretical models to obtain a fit curve for the measured temperature dependence of f. Depending on the theoretical model, f depends on the residence time of the droplets in the supercooled environment. With the derived fit functions, f can be calculated for different residence times, such that measurements with different experimental setups can be compared. The tested models are described in this section, and the resulting fit curves displayed in Fig. 3.6, 3.7, and 3.8 are discussed. The question if heterogeneous freezing of water or solution droplets is rather a stochastic or a deterministic process has been adressed by several studies in the past (e. g. Vali and Stansbury, 1966; Vonnegut and Baldwin, 1984; Vali, 1994). Vali developed the time-dependent freezing rate (TDFR) theory (Vali, 1994) which allows for the calculation of the freezing rate of droplets containing a distribution of different IN. This theory involves an assumption on the IN surface in the sample: In the stochastic hypothesis it is assumed that all IN have an equal efficiency to nucleate ice, and therefore heterogeneous ice nucleation is a stochastic process which can be described by classical nucleation theory (CNT) similarly to homogeneous ice nucleation. The singular hypothesis assumes that there can be a large variability in the ice nucleation efficiency amongst IN of the same species. The rate at which critical ice embryos can be formed on a specific IN then sharply increases within a small temperature interval around a characteristic temperature T_c of that IN. Whereas there is evidence that the singular hypothesis describes heterogeneous ice nucleation well to a first approximation (Vali, 1994), different studies have used different approaches to formulate the droplet freezing rate using singular hypothesis (Connolly et al., 2009; Marcolli et al., 2007), and the importance of the stochastic contribution to droplet freezing has been the subject of recent research (Vali, 2008). The experimental results of the present study have been fitted with fit functions based on three different approaches to describe the singular hypothesis of heterogeneous ice nucleation. The first two formulations involve the concept of a nucleation rate according to CNT. A contact angle α between the IN and the ice embryo is used as a proxy for the ice nucleating properties of the IN with two different approaches for the distribution of contact angles among the IN. The third approach is thoroughly deterministic: The freezing of each IN is determined by its characteristic temperature T_c. The resulting fit curves are compared with a fit based on stochastic hypothesis assuming that all IN have the same surface properties.

70

3.4.1 Distribution of Contact Angles

The description of heterogeneous ice nucleation involving a contact angle distribution combines the stochastic concept of a nucleation rate according to CNT with the assumption of singular hypothesis that individual IN have different ice nucleation properties. According to CNT, the heterogeneous freezing rate of droplets can be written as

$$\frac{dN_u}{dt} = -J \cdot N_u \cdot 4\pi r_N^2, \tag{3.3}$$

where N_u is the number of unfrozen droplets, J is the nucleation rate (i. e. the formation rate of critical ice embryos per unit particle surface area), and r_N is the radius of the IN which is assumed to be spherical. A contact angle distribution is assigned to the IN where every particle is characterized by a different contact angle which is assumed constant over its surface. This model will be referred to with the abbreviation "α-PDF" later on. The nucleation rate J is therefore different for different particles, and equation 3.3 has to be stated for each subset of droplets with contact angle α:

$$\frac{d}{dt} dN_{u,\alpha} = -J(T,\alpha) \cdot dN_{u,\alpha} \cdot 4\pi r_N^2. \tag{3.4}$$

Integration yields

$$dN_{u,\alpha}(T,t) = dN_{u,0}(\alpha,T) \cdot \exp(-J(T,\alpha) \cdot 4\pi r_N^2 \cdot t), \tag{3.5}$$

where $dN_{u,0}$ denotes the number of droplets containing an IN with contact angle α at time $t = 0$ where no freezing has occurred yet. If the contact angles are distributed with a PDF $p(\alpha)$ among the IN, $dN_{u,0}$ is given by $dN_{u,0}(\alpha,T) = N_{tot} \cdot p(\alpha)d\alpha$, where N_{tot} is the total number of droplets. Inserting $dN_{u,0}$ in equation 3.5 and integration yields the number of unfrozen droplets as a function of time,

$$N_u(T,t) = N_{tot} \cdot \int_0^\pi p(\alpha) \cdot \exp(-4\pi r_N^2 J(T,\alpha)t) \, d\alpha. \tag{3.6}$$

From this the frozen fraction of the droplets after the residence time in the ZINC chamber t_{ZINC} can be calculated:

$$f_i = \frac{N_{tot} - N_u(T,t_{\text{ZINC}})}{N_{tot}} = 1 - \int_0^\pi p(\alpha) \cdot \exp(-4\pi r_N^2 J(T,\alpha)t_{\text{ZINC}}) \, d\alpha. \tag{3.7}$$

According to Zobrist et al. (2007), the nucleation rate $J(T,\alpha)$ can be written as

$$J(T,\alpha) = \frac{kT}{h} \exp\left(-\frac{\Delta F_{\text{diff}}(T)}{kT}\right) \cdot n \exp\left(-\frac{\Delta G(T) f_{\text{het}}(\alpha)}{kT}\right), \tag{3.8}$$

where k and h are the Boltzmann and the Planck constant, n is the number density of water molecules at the ice nucleus/water interface, ΔG is the Gibbs free energy for critical ice embryo formation, and ΔF_{diff} is the diffusion activation energy of a water molecule to cross the water/ice embryo interface. Parameterisations for n, ΔG and ΔF_{diff} are given in Zobrist et al. (2007). The compatibility factor f_{het} reduces the energy barrier to ice nucleation compared to homogeneous ice nucleation and can be written as $f_{\text{het}} = (2 + \cos\alpha)(1 - \cos\alpha)^2/4$ (Pruppacher and Klett, 1997). According to Marcolli et al. (2007), the distribution of contact angles for Arizona Test Dust (ATD) can be described by a lognormal distribution. We consider it reasonable to assume that a similar function can be used for kaolinite except from the fit parameters μ and σ which are expected to differ for different mineral dusts:

$$p(\alpha) = \frac{1}{\alpha \sigma \sqrt{2\pi}} \exp\left(-\frac{\log(\alpha) - \mu}{2\sigma^2}\right) \tag{3.9}$$

The fit parameters μ and σ are found using equation 3.7 by minimizing the sum of squared errors weighted by the error bars of the measurements. Since the integral in equation 3.7 cannot be solved analytically, we discretized the range of contact angles into 100 equally spaced bins such that the integral turns into a finite sum. The reference case based on the stochastic hypothesis with all IN having the same contact angle α_0 is obtained from equation 3.7 by replacing $p(\alpha)$ by a delta-function, i. e. $p(\alpha) = \delta(\alpha = \alpha_0)$. This reference case will be referred to as the "stochastical model" later on.

3.4.2 Distribution of Active Sites

The previously described model using contact angles which are constant over an IN surface can be refined by the assumption that nucleating sites of various quality are distributed randomly over the IN surface. One specific IN then has a certain number of such active sites of different quality, and ice nucleation will only occur on these sites. Each active site is characterized by one contact angle, and the frequency of occurrence of different active sites is a function of the contact angle. Similarly to Marcolli et al. (2007) we assume that the active surface area of a nucleating site can be approximated by the surface area covered by a critical ice embryo. Although the radius of a critical embryo generally depends on temperature, for simplicity we assume a constant active surface area of 6 nm^2 which corresponds to a critical ice embryo at 239 K as calculated from CNT. From equation 3.5 it can be seen that the probability for a droplet containing one active site with contact angle α to freeze is given by

$$p_\alpha = 1 - \exp(-J(T,\alpha)A_\alpha t_{\mathrm{ZINC}}), \tag{3.10}$$

where A_α is the surface area of the active site. With the range of contact angles discretized as in 3.4.1, the probability p_{frz} for a droplet to freeze is equal to the probability that ice nucleation occurs on an active site in any of the contact angle intervals that the total contact angle range consists of. As the probability that a droplet containing one active site with contact angle α does *not* freeze is given by $\bar{p}(\alpha) = \exp(-J(T,\alpha)A_\alpha t_{\mathrm{ZINC}})$, p_{frz} can be written as

$$p_{\mathrm{frz}}(T) = 1 - \prod_{i=1}^{m} \bar{p}(\alpha_i) = 1 - \prod_{i=1}^{m} \exp(-J(T,\alpha_i)A_{\alpha_i} t_{\mathrm{ZINC}}), \tag{3.11}$$

where m is the number of intervals in $[0,\pi]$ with an interval size $\Delta\alpha$, and A_{α_i} is the total surface area of all active sites with contact angles in $[\alpha_i, \alpha_i + \Delta\alpha]$ present in the droplet. For an individual droplet, A_{α_i} can be integer multiples of the active site surface area $A_1 = 6$ nm^2, i. e. $A_{\alpha_i} = n_i \cdot A_1$, $n_i = 0, 1, 2, ...$ In order to calculate $p_{\mathrm{frz}}(T)$ for a specific droplet, the droplet has to be assigned a set of n_i values depending on the surface density of active sites in each contact angle interval $[\alpha_i, \alpha_i + \Delta\alpha]$. If $\rho(\alpha)$ is the surface density of active sites per unit contact angle interval, then the average number of active sites in $[\alpha_i, \alpha_i + \Delta\alpha]$ on one IN (i. e. in one droplet) is given by

$$\bar{n}_i = 4\pi r_N^2 \rho(\alpha_i) \Delta\alpha. \tag{3.12}$$

The probability to have a number of n_i active sites in $[\alpha_i, \alpha_i + \Delta\alpha]$ in a single droplet is then given by the poisson distribution:

$$P(n_i) = \frac{\lambda_i^{n_i} \exp(-\lambda_i)}{n_i!}, \quad \text{with} \quad \lambda_i = \bar{n}_i = 4\pi r_N^2 \rho(\alpha_i) \Delta\alpha. \tag{3.13}$$

We use poisson distributed random variables to assign a set of n_i values to one droplet, and for an ensemble of 1000 droplets we calculate the freezing probability $p_{\mathrm{frz},j}$ for each droplet. The frozen fraction of the droplets after time t_{ZINC} in the ZINC chamber is then calculated as the sum of the individual freezing probabilities divided by the total number of droplets,

$$f_i(T) = \frac{1}{N_{tot}} \sum_{j=1}^{N_{tot}} p_{\mathrm{frz},j}(T). \tag{3.14}$$

Marcolli et al. (2007) have found that the surface site density $\rho(\alpha)$ for ATD can be fitted by a function of the following type:

$$\rho(\alpha) = b \cdot \exp\left(\frac{-\beta_1}{\alpha - \beta_2}\right), \tag{3.15}$$

with three fit parameters b, β_1 and β_2. Again we consider it reasonable to assume that the active site surface density of kaolinite can be described by a similar function. Therefore we fitted the measured frozen fraction of droplets with the theoretical frozen fraction from equation 3.14 using equation 3.15. The resulting optimum fit parameters b, β_1 and β_2 correspond to weighted least squared errors between measurements and the fit function. This model will be referred to as the "active site model" later on.

3.4.3 Deterministic Formulation

Unlike in the two previously described formulations of the singular hypothesis which keep the stochastic concept of a nucleation rate, the assumption can be made that the nucleation rate of a specific IN (or a specific active site) is not a smooth function with temperature, but increases so sharply at a certain characteristic temperature T_c that it can be described by a step function. In this case, the IN will inevitably freeze the droplet it is immersed in as soon as the temperature of the droplet decreases below T_c. At constant temperature, however, no freezing event can occur. In this approximation, one can define a surface density $n_s(T)$ of sites active between T and $273\,K$ (Connolly et al., 2009). If $K(T) = \frac{d}{dT}n_s(T)$, then $-K(T)$ denotes the number of sites becoming active per unit surface area of the IN upon cooling the sample by a unit temperature interval. In a sample of droplets, the number of freezing droplets dN_i per temperature interval dT can be written as

$$\frac{dN_i}{dT} = (N_{tot} - N_i)AK(T) \quad \text{or} \quad dN_i = (N_{tot} - N_i)AK(T)dT\,, \tag{3.16}$$

where N_i is the number of frozen droplets, N_{tot} is the total number of droplets, and A is the surface area of an IN, approximated by $A = 4\pi r_N^2$. In this formulation, the expression $-AK(T)dT$ is the average number of sites active in $[T, T+dT]$ on one IN. Integration of equation 3.16 yields the number $N_i(T)$ of droplets frozen after the sample has been cooled to temperature T,

$$N_i(T) = N_{tot}\left(1 - \exp(-An_s(T))\right) \quad \text{with} \quad n_s(T) = -\int_{273K}^{T} K(T')dT'\,, \tag{3.17}$$

(Connolly et al., 2009). The frozen fraction of droplets f_i is then given by

$$f_i = 1 - \exp(-An_s(T))\,. \tag{3.18}$$

This model will be referred to as "deterministic". Note that as long as $n_s(T)$ can be calculated analytically, the calculation of N_i is straightforward. However, if numerical integration is necessary with finite temperature intervals ΔT rather than infinitesimal dT, then equation 3.16 might not hold strictly anymore: If the probability that an IN has two or more active sites in $[T, T+\Delta T]$ is not negligible, then the assumption entering in equation 3.16 of each active site causing one freezing event is not fully justified anymore. For fitting our data with equation 3.17 according to weighted least squares, we used a function for $n_s(T)$ similar to the one found by Connolly et al. (2009) for different mineral dust samples like ATD and Asian Dust,

$$n_s(T) = \begin{cases} A_1(T+A_2)^2\,, & T < -A_2 \\ 0\,, & T \geq -A_2 \end{cases} \tag{3.19}$$

We also tested a linear function for $n_s(T)$, but this yielded a poor fit of the measured data.

3.4.4 Resulting Fit Curves

The fit curves obtained with the previously described models are shown in Fig. 3.6, 3.7, and 3.8. For the models involving CNT, a residence time of $t_{ZINC} = 14$ s at the experimental temperature has been taken. As the models use parameterisations of surface properties of the kaolinite particles like e. g. a distribution of contact angles or a surface density of nucleating sites active between $0°C$ and T which are independent of the particle size, the data for all investigated sizes can be fitted with one set of parameters for each model. In the case of the α-PDF model, the difference in the corresponding fit curves for different particle sizes are then only due to the particles exhibiting different surface areas, whereas in the active site model, larger particles are also IN of better "quality". The resulting fit parameters are given in Tab. 3.1.

For the α-PDF model and the active site model, the contact angle distribution and the surface density of active sites are displayed in Fig. 3.9.

Table 3.1: *Fit parameter values obtained by minimizing the sum of squared errors. The obtained minimum value for the weighted sum of squared errors is given in the fourth column labeled Total error. The root mean square error (RMSE) between the fits and the data points are given in the last column.*

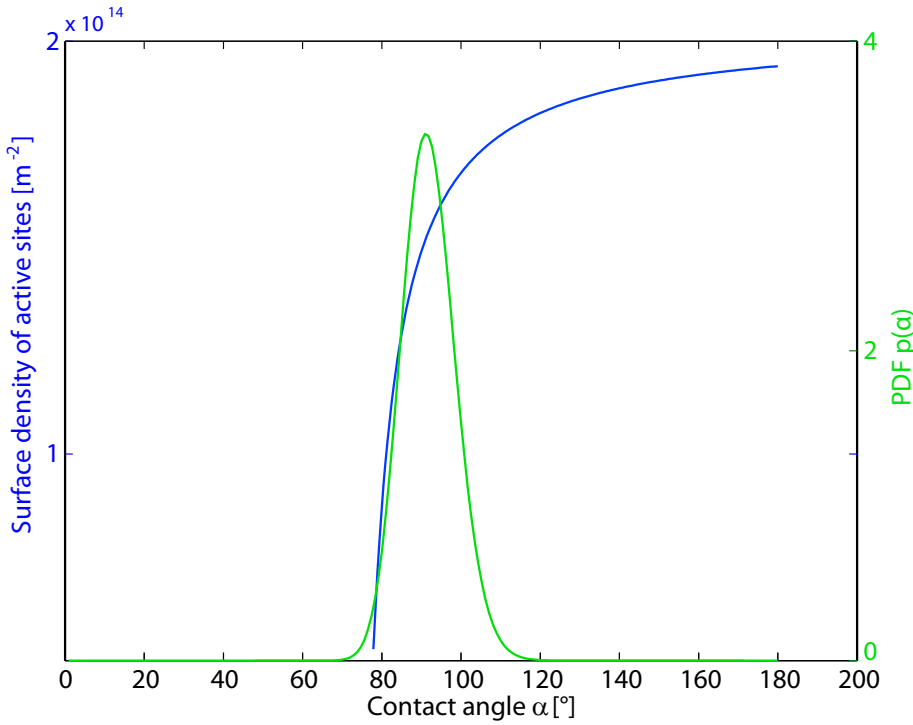| Model	Parameter	Value	Total error	RMSE
Stochastic	α	1.579	169.73	0.26
α-PDF	μ	1.6	106.55	0.168
	σ	0.074		
Active sites	b	$2.031 \cdot 10^{14}\,\mathrm{m}^{-2}$	76.85	0.173
	β_1	0.085		
	β_2	1.296		
Deterministic	a_1	$2.704 \cdot 10^{11}\,\mathrm{m}^{-2}\mathrm{K}^{-2}$	60.52	0.138
	a_2	$31.709°\mathrm{C}$		

Figure 3.9: *Distribution of contact angles among the IN for the α-PDF model (green curve) and surface density of active sites per unit contact angle interval for the active site model (blue curve).*

Note that the PDF $p(\alpha)$ is normalized to 1 for α in radians, and $\rho(\alpha)$ is the surface density of active sites per unit contact angle interval (also in radians). It is clear from Fig. 3.6, 3.7, and 3.8 that the stochastic model with one constant contact angle for all IN does not well represent the data. This is supported by the fact that with a value of 0.26, the root mean square error (RMSE) between the data and the fit is the largest among all models (see Tab. 3.1). For the other models, the differences are less pronounced. For 200 nm and 800 nm particles, visual inspection of the fit curves suggests that the model using a distribution of active sites represents the data better than the α-PDF model. This is also supported by the smaller sum of weighted squared errors (labeled "Total error" in Tab. 3.1) of 76.85 compared to 106.55, whereas the RMSE value is slightly lower for the α-PDF model. The α-PDF model seems to slightly overestimate the frozen fraction for the 200 nm particles, whereas it slightly underestimates f for the 800 nm particles. This underestimation of the size dependence of f suggests that not only the

larger surface area of larger particles is responsible for the size dependence of f. Including also the possibility that larger aerosol particles are IN of better "quality", the active site model represents the size dependence of f better. With a value of 0.138, the deterministic model has the smallest RMSE of all tested models.

In Fig. 3.10, the fit functions of the active site model and the deterministic model are displayed for all three particle sizes.
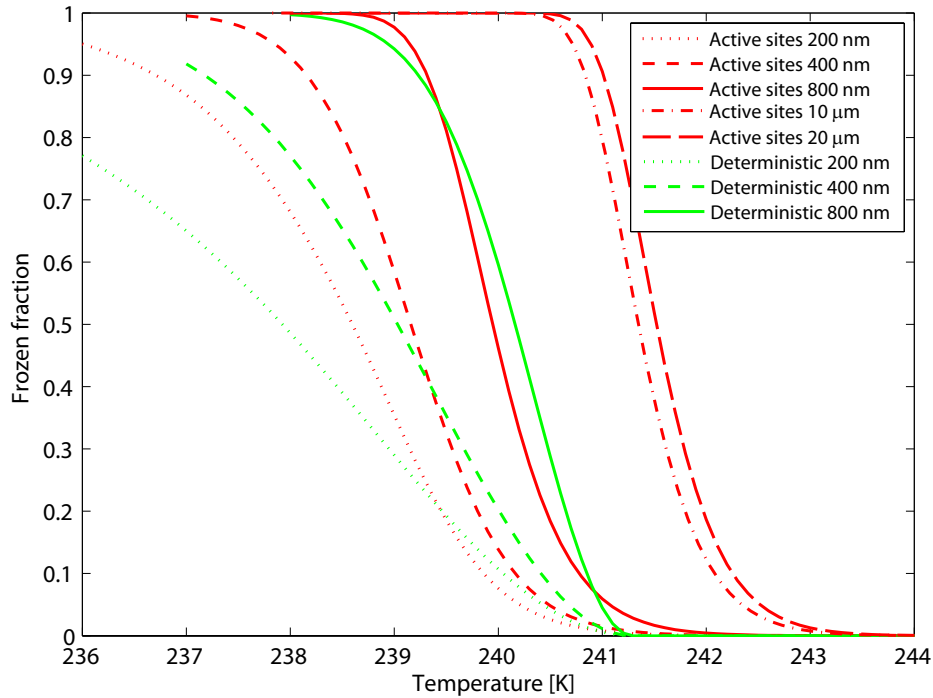

Figure 3.10: *Fit curves for the active sites model and the deterministic model for all particle sizes. The active site model is also extrapolated to* $10\,\mu m$ *and* $20\,\mu m$ *particles.*

Whereas the low RMSE value of the deterministic model suggests that this model best represents the measured data in the present experiments, a drawback of the deterministic model compared to the active site model is visible at the onset of ice nucleation. Whereas the onset occurs at colder temperatures for smaller IN in the active site model, it occurs at the same temperature in the deterministic model. Therefore, this model can only be used to calculate f for the size range of IN which the fit parameters were determined with. Extrapolation to increasing IN sizes requires an onset of freezing at increasing temperatures. The red dash-dotted line in Fig. 3.10 shows an extrapolation to $20\,\mu m$ particles with the active site model. Extrapolating a fit to (atmospherically irrelevant) large particle sizes has been done to compare the present measurements with earlier measurements with suspension droplets by Pitter and Pruppacher (1973) and Hoffer (1961). One large IN in the present fit then approximates the total IN surface in a suspension droplet. The extrapolation shows that the size dependence of f becomes weaker for increasing particle size and vanishes for particles larger than around $20\,\mu m$. That is, the active site model predicts no median freezing temperatures above around $-31°C$ for droplets with immersed kaolinite particles, regardless of the droplet and particle sizes. However, it is unclear if the fit function correctly describes the surface distribution of active sites with low contact angles which are too sparsely distributed to be present on the particles used in the present experiments but could be present on $20\,\mu m$ particles.

In general, we consider the fits of the active site model and the deterministic model as satisfactory for the experiments with 200 nm and 800 nm particles. For 400 nm particles, the curves poorly match the

data except for the α-PDF model. However, due to experimental difficulties during the experiments on 400 nm particles, these data have more scatter and are more difficult to fit with the functions determined with the entire set of data.

3.5 Conclusions

In the present study, heterogeneous ice nucleation in the immersion mode has been investigated for three different sizes of kaolinite particles. Water droplets with single immersed IN have been produced by CCN activation and subsequently cooled down to the required supercooling in a streamwise temperature gradient with the newly developed IMCA chamber. After exposing the droplets to supercooled temperatures in ZINC, the frozen fraction of the droplets has been measured with the newly developed IODE depolarisation detector. Tests with IMCA have shown that the supersaturation profile in the warm upper section of IMCA allows nucleated water droplets to grow large enough that they do not evaporate in the subsaturated cold part of IMCA and in ZINC. However, there are indications for some unactivated particles in the ZINC chamber which might contribute to the measured ice crystals via deposition nucleation. Ice nucleation in the immersion mode has been observed at temperatures where deposition nucleation has been reported to be active for the same kind of particles (Welti et al., 2009). In the present experimental runs, a concurrence between the deposition and the immersion mode can be seen in a significant reduction of ice crystals nucleated in the deposition mode upon increasing the supersaturation in the IMCA chamber. After this reduction, the ice crystal number concentration increases when water droplets reach the ZINC chamber and freeze via immersion freezing (given the temperature in ZINC is low enough). The maximum possible ice crystal contribution from deposition nucleation has been subtracted from the detected ice crystal number concentration in order to obtain the amount of ice formed in the immersion mode alone.

Depolarisation measurements with IODE have shown that ice crystals nucleated via immersion freezing lead to less depolarisation than ice crystals nucleated in the deposition mode, which is probably due to frozen droplets having a less aspherical shape than ice crystals grown in the deposition mode. The onset of droplet freezing has been observed at around $-30°$C, depending on particle size. 50% of the droplets were frozen at a median freezing temperature of $T_m = -35°$C roughly for 200 nm particles and $T_m = -33°$C for 800 nm particles. Although not very strong, a size dependence of the IN efficiency of the particles can be seen. The measured median freezing temperatures do not suggest kaolinite particles in this size range to be very efficient IN. Our measurements support the findings on freezing of kaolinite suspension droplets by Hoffer (1961), whereas the higher freezing temperatures reported by Pitter and Pruppacher (1973) could not be reproduced. Extrapolating the best fit of the measured data to large particle sizes representing the increased IN surface in large suspension droplets yielded an increase in the median freezing temperature of around 2 K maximum, compared to the value for 800 nm particles. This increase is not large enough to account for the difference between our measurements and the wind tunnel experiments by Pitter and Pruppacher (1973). We suppose that this discrepancy could be due to the different experimental technique in the wind tunnel experiments. Also, mineral dust samples of the same species may exhibit variable properties when they originate from different sources.

The temperature dependent frozen fraction of droplets has been fitted with different theoretical approaches. Whereas classical nucleation theory with the stochastic hypothesis is clearly not suitable to describe the present data, a formulation based on classical nucleation theory in combination with a surface distribution of active sites of different qualities represents the measured data reasonably well. An even better fit of the measured data is obtained with the simpler deterministic model. However, the fit obtained with this model cannot be used to calculate f for particle sizes outside the investigated size range. More work on the time dependence of the frozen fraction can help to further assess differences between the active site model and the deterministic model. More experiments with particles coated with soluble substances will also help to rule out deposition nucleation in the ZINC chamber.

Chapter 4

IMCA Experiments

4.1 Details of the Experimental Setup

The experimental setup used in the present work is shortly described in chapter 2 and 3. Also, the choice of IMCA chamber dimensions (wall distance, chamber length etc.) is discussed in chapter 2. In this section, some more technical details are presented. A schematic picture showing IMCA in a side view including all functional elements around it is shown in Fig. 4.1, and Fig. 4.2 shows a photograph of IMCA in the laboratory in a frontal view.

The IMCA chamber walls are machined from aluminum plates, and the inner surfaces are sandblasted and anodized. Anodizing helps to prevent aluminum from being corroded by deionized water, and sand-blasting provides for a good wettability of the surface which is important for an even ice layer in the cold part of IMCA. The 3.5 cm wide side walls of IMCA are made of stainless steel and are separated from the aluminum walls by a VMQ elastomer layer (by Angst + Pfister). This tightens the interface between two metal surfaces and thermally isolates them from each other. Thermal isolation is important since in the upper part of IMCA, wall temperature differences of 20 K and more have to be maintained in an experiment. Without an isolating layer, heat conduction via the stainless steel side walls would not allow for such large temperature differences. As the screws attaching the sidewalls to the chamber walls also conduct heat, they are isolated from the side walls by teflon distance rings (white on Fig. 4.2). Cooling the chamber walls at CU1 and CU2 is achieved by copper blocks. Cooling liquid flows through these blocks in copper tubes with an inner diameter of 10 mm. In order to obtain sufficient thermal contact between the copper blocks and the aluminum walls, the surfaces are coated with heat conducting paste before the blocks are screwed onto the chamber walls. The same principle is used to heat the uppermost parts of the IMCA walls. The two heating blocks enclose two cylindrical electrical heaters by Probag each (the power cords for these heaters can be seen in Fig. 4.2). On the cooler IMCA wall, a total power of 250 W is sufficient, whereas the two heaters on the warm wall have a total power of 640 W. High performance heaters are required because a large amount of thermal energy is transported from the heating blocks to CU1 through the aluminum wall. On one hand, the good thermal conductivity of aluminum leads to a quick development of a linear temperature profile within the wall. On the other hand, sufficient power is needed at the heating and cooling stages.

4.1.1 The Humidification System

Humidification of the chamber walls is achieved by a continuous flow of water down a filter paper on each wall. At the top, the papers are pinched into a channel by a stainless steel tube carrying water. The water is pumped into that tube by a KNF membrane pump and leaves the tube via a row of small holes contacting the filter paper. A schematic picture of this can be seen in Fig. 4.3.

The filter paper ends at the position of CU1, where channels in the walls collect the excess water
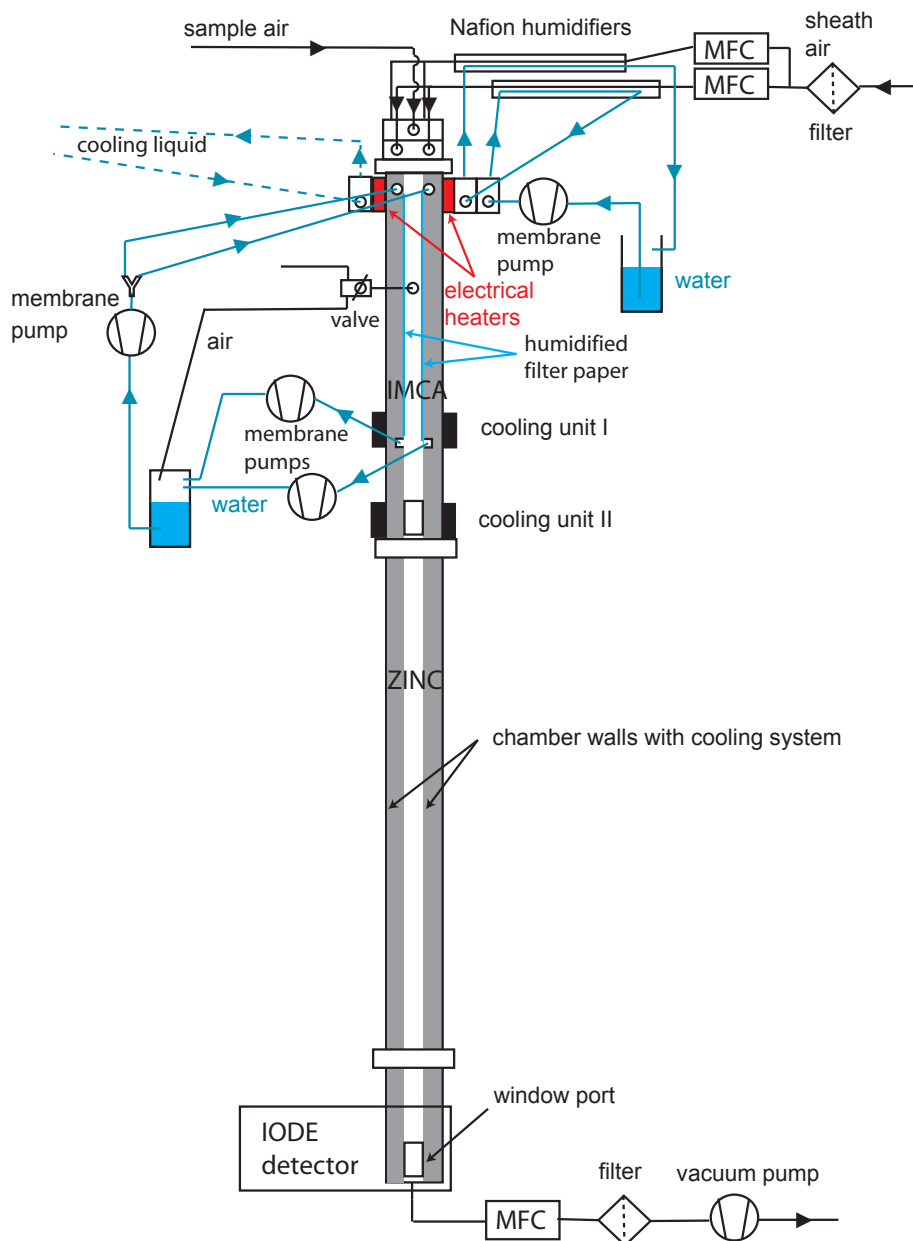
Figure 4.1: *Schematic of the IMCA chamber (side view). See text for details.*

which is pumped out of each channel by a KNF membrane pump. The flow rate of water in the supply tube is on the order of some ml/min. We use separate pumps to pump the water in and out of the chamber, since the chamber cannot be operated with a closed water cycle. The flow rate at which the water has to be pumped out at CU1 reacts with a delay around one minute to the flow rate at the water inlet. With a closed water cycle including only one membrane pump per chamber wall, a reduction of the flow rate could lead to insufficient draining of the collecting water channel during around one minute. In general, overflow of the collecting channel needs to be avoided since otherwise, water can run down below CU1 and freeze between CU1 and CU2. Clogging of the chamber is the consequence. To avoid this, the pump rate is always larger at the draining channel, which implicates that a mixture of water and air is pumped
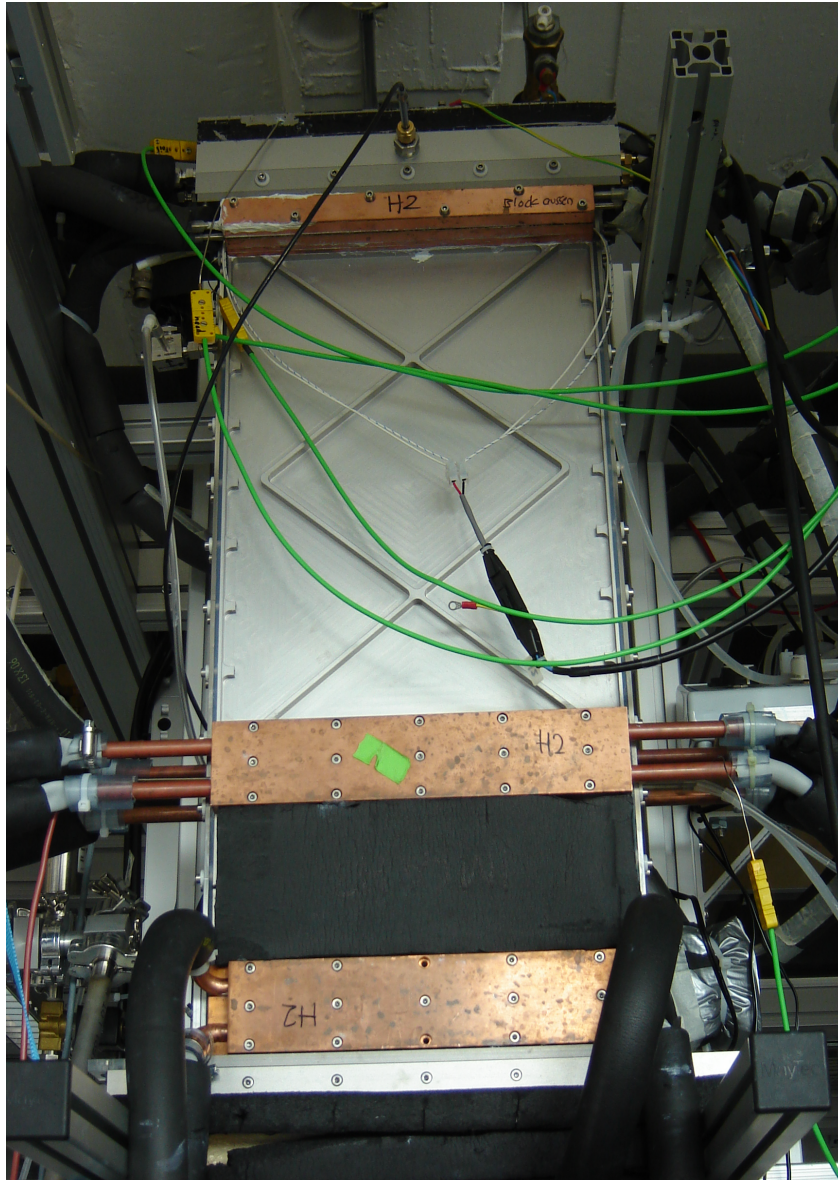
Figure 4.2: *Frontal view of IMCA in the laboratory, mounted on top of the ZINC chamber.*

out of the chamber most of the time. Both water and air are recycled: The water is pumped back into the inlet channel, and the air re-enters the chamber by a valve visible in Fig. 4.1 and 4.2.

An even more important reason why a closed water cycle cannot be used in this setup is that diffusion transports a considerable amount of water from the warm IMCA wall to the colder wall when a temperature difference is applied to the heating blocks. Thus, the flow rate of water into the draining channel can be significantly larger than the flow rate in the inlet channel on the colder wall. Furthermore, when humidified sheath air is cooled from 313 K to 273 K, water vapour condenses on the walls and leads to an additional flow towards the draining channels. The total outflow of water can therefore be larger than the total inflow.

The filter papers have to be mounted and humidified during the assembling process of IMCA. Capillary forces attach the wet paper to the walls, but air bubbles have to be removed manually before the chamber is closed. Once mounted in the chamber, the filter papers must not dry out, otherwise they detach from the walls and have to be replaced. Detached filter papers would disturb the flow inside IMCA and are very hard to humidify regularly.
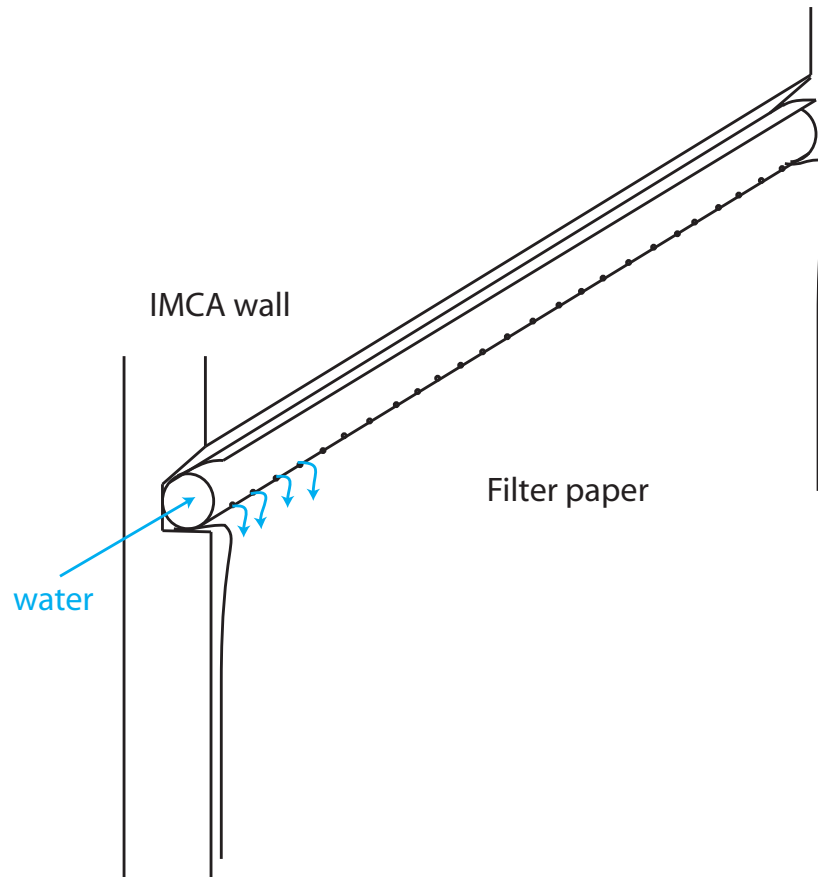
79

Figure 4.3: *Schematic of the water supply for the humidification of the chamber walls. The tube is closed at the far end, such that the water has to leave the tube by the small holes. The tube at the same time fixes the filter paper and humidifies it by continuous water supply.*

4.1.2 Icing the Low Part of IMCA

As discussed in section 2.5, each of the cooling blocks of CU2 carries the cooling liquid of the corresponding ZINC wall, which leads to a relative humidity RH_w significantly above ice saturation, provided that the walls are coated with ice. Especially on the warmer wall, the ice layer needs to be thick enough to allow for a diffusive flux of water vapour towards the cooler wall during 2 to 3 hours, which is roughly the time required for one experiment. Ice layers on the IMCA walls in the cold section between CU1 and CU2 are achieved by the same icing procedure as for the ZINC chamber. Prior to icing, ZINC (and therefore also CU2 of IMCA) is cooled to 253 K, whereas CU1 is cooled to 266 K. Water is then pumped into ZINC from below until the water reaches a water level sensor. Compared to the original use of ZINC, this water level sensor has been raised to a higher location by a tube connected to ZINC at the port where originally the water level sensor was placed. This configuration is illustrated in Fig. 4.4.

The water therefore continues to rise until it reaches the lower edge of CU1, where the temperature transition between $T < 273\,\text{K}$ and $T > 273\,\text{K}$ is located. During 30 seconds, an ice layer can establish on the walls before the water is pumped out of the chamber again. This method of sensing the water level in IMCA indirectly in a parallel tube has the disadvantage that it is not very precise. Due to wall friction, the water level does not necessarily have to be at exactly the same level in the tube and in IMCA during pumping. It is therefore impossible to determine precisely which level the ice layers reach up to after icing. For future work, modifications to the IMCA sidewalls will allow to sense the water level in IMCA directly.

The deionized water used to ice ZINC and IMCA is precooled to 280 K. Although this has not been systematically tested, using precooled water seems to yield more reliable icing of the low part of IMCA
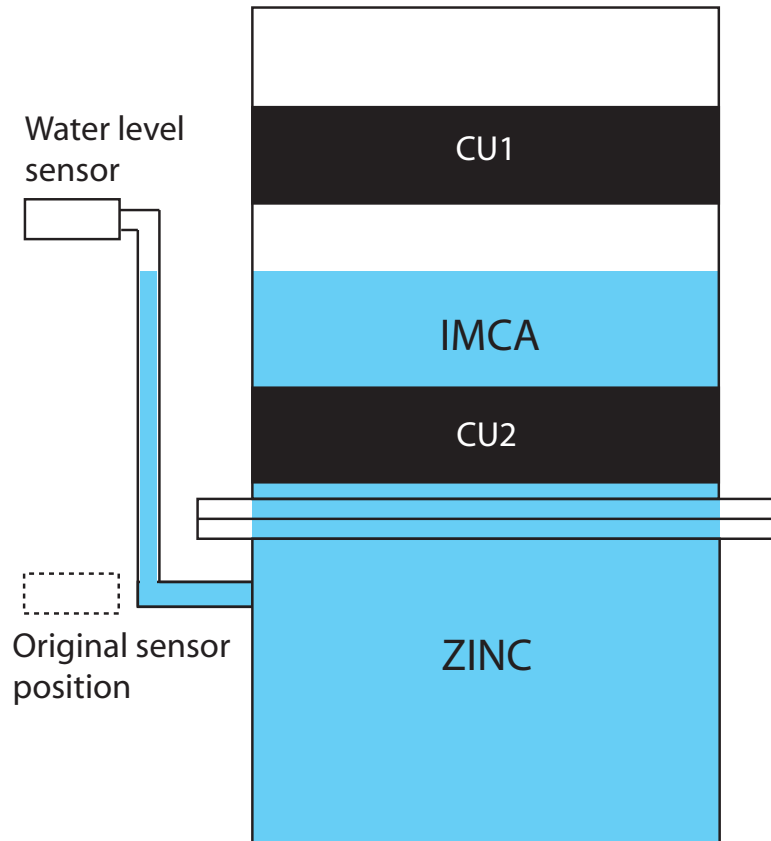
Figure 4.4: *Configuration used for icing of ZINC and the lower part of IMCA at the same time. A tube raises the position of the water level sensor to the lower edge of CU1, such that the IMCA walls get an ice coating where $T < 273\,K$. Blue color indicates rising water during pumping.*

than using water at room temperature. Although water pumped in at room temperature is certainly cooled to some degree on the way up the cold ZINC chamber, the IMCA walls are considerably heated by the water, because the heat capacity of the relatively thin IMCA walls is lower than the one of the massive ZINC walls. On the other hand, excessive precooling of the water can lead to an enhanced thickness of the ice layer. After icing with water cooled to 274 K, background ice counts quickly increase to a level at which no reliable measurements could be taken anymore. In this case the ice layer is probably too thick or irregularly formed in the lower part of the IMCA chamber.

4.1.3 The Inlet Section

A schematic picture of a vertical cross section of the inlet section of IMCA is shown in Fig. 4.5. It largely resembles the corresponding setup for the ZINC chamber, which can be seen in Stetzer et al. (2008). In Fig. 4.5, sealings and screws have been omitted for simplicity.

After the inlet connector, the sample flow is evenly distributed over the depth of the IMCA chamber (0.3 m) by two injection blades and injected into the region where the sample flow is combined with the sheath air flows. Little below, the chamber narrows from 1 cm diameter to 0.5 cm which remains constant for the rest of the IMCA chamber. Below the water inlet channels (WI in Fig. 4.5), a supersaturation profile establishes between the walls heated to different temperatures, and cloud droplets nucleate and grow on the aerosol particles. The region where the sample and sheath air flows are combined is not humidified from the walls. This can be crucial when WCPC-droplets are injected into the chamber instead
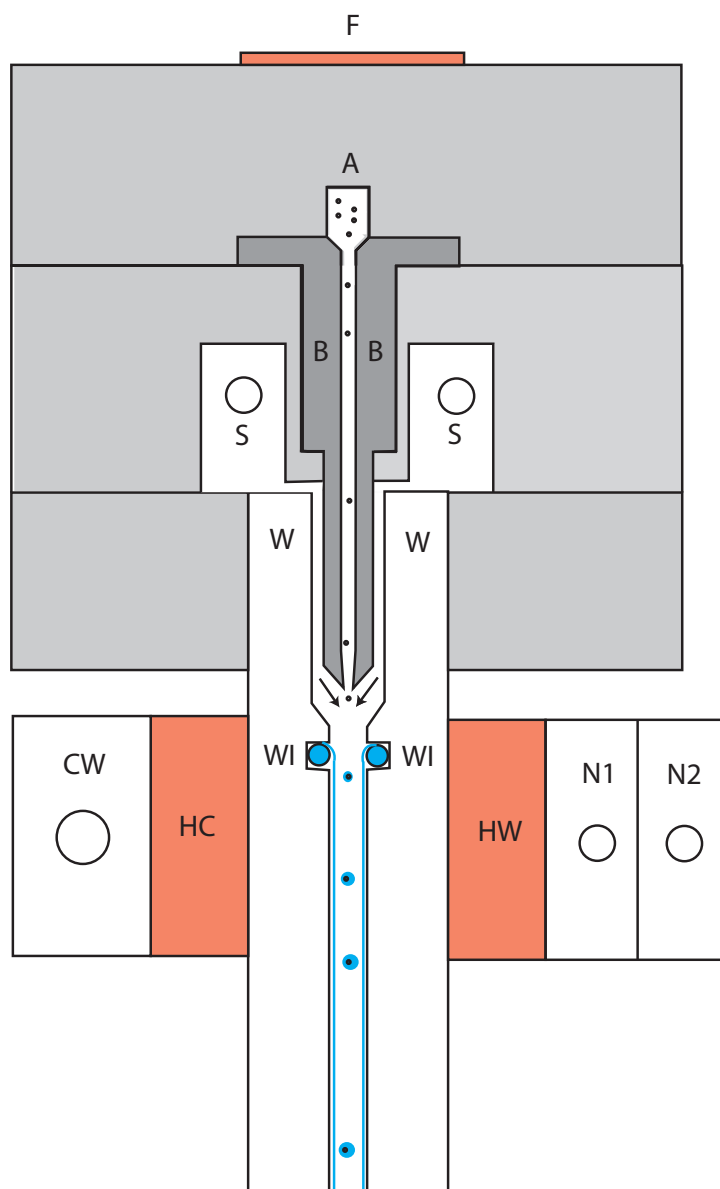
Figure 4.5: *Schematic picture of the inlet section of IMCA (side view). A - Aerosol inlet channel. B - Blades distributing the sample flow over the depth of the chamber (perpendicular to the image plane), and focusing it in the center of the chamber. CW - Block carrying cooling water for the cooler wall. F - Heating foil. HC, HW - Heating blocks. N1, N2 - Blocks carrying water used to humidify the sheath air in Nafion humidifiers. S - Sheath air inlet. W - IMCA chamber walls. WI - Water supply tubes for humidification of the filter papers (see Fig. 4.3).*

of bare aerosol particles. WCPC-droplets with a diameter between 3 and 4 μm need a precise control of the relative humidity in order not to evaporate before they reach the humidified part of IMCA. From experiments performed with droplet activation in a WCPC we could not see that less supersaturation in IMCA would be required to obtain liquid water droplets at the detector position. This suggests that the WCPC-droplets evaporate before droplets nucleate again on the remaining particles in the humidified part of IMCA. Either the droplets encounter variations in temperature and thus in relative humidity before they leave the injection blades, or the combination of sample and sheath air leads to a subsaturated spot after the injection blades. The occurrence of subsaturation is probably due to a complicated

temperature distribution in the sheath air channels, as the saturation of the humidified sheath air is very difficult to control. Furthermore, already the humidity of the sheath air entering the sheath air channels is hard to control. Humidification of the sheath air is obtained by passing each of the two sheath flows through an 48" Nafion humidifier (by Permapure). There, a cylindrical Nafion membrane separates the inner air volume from the outer water volume, and the membrane allows for diffusion of water vapour into the air. The relative humidity of the air at the exit of the humidifier depends on the air flow rate and the water temperature. These dependencies are specified on data sheets for constant water temperatures. However, the water temperature cannot be considered constant in the present setup. Water is heated in two recipients on top of the warm wall heater (N1 and N2 in Fig. 4.5), and is pumped into the Nafion humidifiers. Cooled by the air flow entering at room temperature, the water is colder by several degrees when it leaves the Nafion humidifiers and circulates back to the heating recipients. In order to obtain the highest mixing ratio at the end of the humidifier (just before the sheath air enters the sheath air channel of IMCA), air and water circulate according to the counter flow principle. Nevertheless, the degree of humidification of the sheath air is not known without CFD modeling. A schematic picture of the sheath air humidification can be seen in Fig. 4.6.
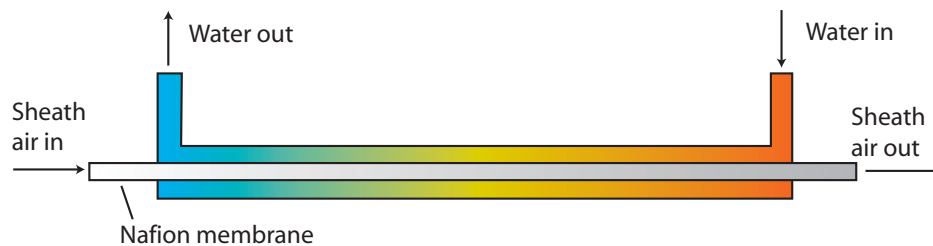

Figure 4.6: *Schematic picture of the sheath air humidification. Colours indicate the water temperature (red corresponding to warmer, blue to colder). Grey shading of the air volume indicates the increasing relative humidity of the sheath air.*

Due to these issues, all experiments reported in chapter 3 have been performed with CCN activation directly in the IMCA chamber. In this case, the relative humidity of the sheath air is not of crucial importance.

4.1.4 The Evaporation Section

In conventional ZINC experiments, an optical particle counter (OPC) in combination with a multichannel analyzer (MCA) is used to distinguished between ice crystals and aerosol particles via the size. As the OPC cannot distinguish between ice crystals and water droplets that might form if RH_w in ZINC is above water saturation, an evaporation section after the main chamber of ZINC evaporates liquid water droplets while conserving ice crystals. This evaporation section is isothermal, meaning that the ice coated walls are at equal temperatures (Stetzer et al., 2008). A constant relative humidity of $RH_i = 100\%$ establishes which corresponds to subsaturation with respect to liquid water, depending on the temperature.

For experiments on immersion freezing, liquid water droplets must not evaporate before they reach the detector retrieving the phase of particles. Therefore, the original evaporation section has been replaced by a short one with a length of only 14 cm between the ZINC main chamber and the detector position. Although it is not ideal to conserve liquid droplets, this section is cooled by the warm wall cooling liquid of ZINC on both sides. As previously discussed, differing wall temperatures would lead to a droplet trajectory shifted towards the colder wall, which would move the aerosol layer out of the detection volume of the IODE detector. However, the residence time in this isothermal section is short enough that droplets nucleated and grown in IMCA should not evaporate for the settings used in experiments (see section 2.5). For future experiments, changes in the sidewalls of ZINC are planned which

allow to measure the frozen fraction of droplets directly in the ZINC chamber.

4.2   IMCA Control

IMCA is operated with a LabView program developed in this project, which controls the hardware and samples data. Several I/O modules are used to measure temperatures and control heating elements. K-type thermocouples are read out with NI 9211 thermocouple input modules by National Instruments, and most control voltages are output with NI 9263 analog output modules. Additionally, a NI 6008 module is used to control and read out a humidity sensor for the sheath air channels. All modules communicate with a laptop via USB. Temperatures in the warm part of IMCA are regulated by virtual PID controllers implemented in the main LabView program. According to a measured temperature, a PID controller calculates a control voltage which is passed to the corresponding heating element. The control voltage is proportional to the power at which the heating element is running. Temperatures in the cold part of IMCA (i. e. at CU1 and CU2) are controlled by bath cryostats. While CU2 is cooled by the ZINC system, CU1 is cooled by an independent cryostat (Lauda RE 310). The setpoint temperature for CU1 is passed to this cryostat via a RS232 serial port. A screenshot picture of the LabView program's user interface with the most important functionalities highlighted is shown in Fig. 4.7.

On Panel 1, the IMCA top temperature (labeled "Master Temp") can be set as well as the top wall temperature difference dT and the setpoint temperature for the cryostat at CU1. The "send" buttons serve to communicate the entered values to the corresponding temperature control unit (software or hardware). The routine is programmed in a way that control parameters are only transferred when they are changed, i. e. the value in the input field is only read out when the "send" button is pressed. On panel 2, the two top wall temperatures measured at the heating blocks are monitored (first and second subplot). The third subplot can monitor the temperature in a tube connecting the WCPC exit with the sample inlet of IMCA (labeled "transition"). For reasons discussed in section 4.1.3, this is not used in the present work. Panel 3 monitores the temperature between one of the two cooling blocks of CU1 and the IMCA wall (labeled "Temp zeroline"). Precise monitoring of this temperature is important as the temperature has to be close to 273 K (usually the temperature is set to 273.3 K), but it must not decrease below 273 K. Temperatures below 273 K at CU1 can lead to freezing up of the draining channels of the wall humidification system, which can damage the membrane pumps. The switches on panel 4 serve to switch the water pumps of the wall humidification system on and off, and to regulate the flow rates in the inlet and the draining channel. Pressing the "LOG DATA" switch enables writing of the measured temperatures and of the calculated peak supersaturation at the top of IMCA into separate files. These files are used to generate time series plots as shown in Fig. 3.5. On panel 6, the PID parameters of the PID-subroutines controlling the heating elements can be set. Panel 7 allows to remotely adjust the WCPC settings or to read out the counts, in case the WCPC is used to activate aerosol particles.

4.3   The New Version of the IODE Detector

The working principle and the application of the IODE detector in the present experiments have been discussed in section 3.2.3. Technical details about IODE (in the original version) can be found in Nicolet et al. (2008). In the present section, improvements to the original version and details that are important for the operation of IODE in experiments on immersion freezing are discussed.

The new version of IODE has been built in a more compact and user-friendly way compared to the original version. All optical elements have fixed positions in a microoptic cage structure called Nanobench (by Linos). The small dimensions of elements and cage structure allows for a small detector size. Due to the moderate weight, the detector can be attached directly to the chambers and does not need additional support. The attachment parts of the detector are mechanically separated from the optical elements, such that mechanical strain arising from temperature changes in the ZINC chamber is not
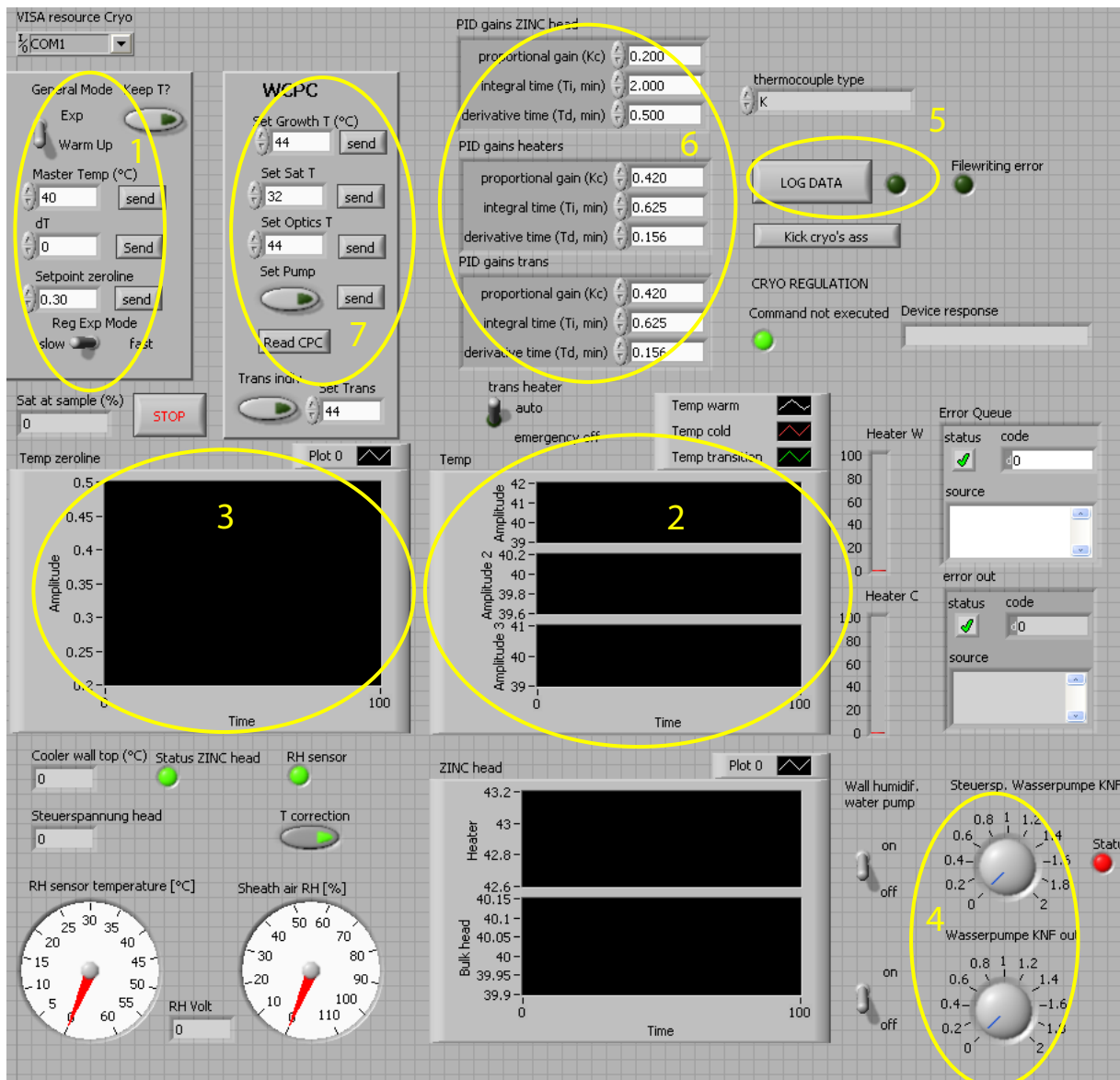
Figure 4.7: *Screenshot picture of the LabView user interface controlling IMCA operation. The most important functionalities are highlighted: 1 - Panel to set the main temperatures, 2 - Graph monitoring the main temperatures, 3 - Graph monitoring the temperature at CU1, 4 - Switches to turn the wall humidification pumps on and off and to regulate the pump speed, 5 - Switch to write measured data to files, 6 - PID parameters of the virtual PID controllers, 7 - Panel to set WCPC parameters*

transferred to the optics and does not lead to misalignment. The laser beam is directed into the chamber via three mirrors. Adjustment of the first two mirrors can be done from outside the detector housing by two screws for each mirror changing the orientation of the mirror in two dimensions.

4.3.1 Peak Detection

An important change has been done on the software level. In order to calculate single particle depolarisations as described in section 3.2.3, a peak detection algorithm is applied to the measured backscattered signal to decide when a particle is present in the laser beam. The sampling rate of the detector electronics is 10 kHz. The LabView program operating the detector passes a data package of 5000 data points every 0.5 seconds to the peak detection algorithm which identifies the locations and amplitudes of the signal peaks. In the original version of the software, the peak detection algorithm was applied to both

the parallel and the perpendicular channel. Three cases were distinguished: If in both channels a peak was detected at the same time (up to a certain tolerance), the depolarisation of the corresponding particle was calculated according to equation (3.1). Depending on the value of the depolarisation, the particle was counted as an ice crystal or a water droplet. If only a peak was detected in the parallel but not in the perpendicular channel, the corresponding particle was automatically counted as a water droplet without calculating the actual depolarisation of the signal. If a peak was detected in the perpendicular but not in the parallel channel, no particle was counted. However, this method of calculating the depolarisation only when a peak is detected in both channels can lead to erroneous counting. In Fig. 4.8, this is illustrated with two hypothetical particles.
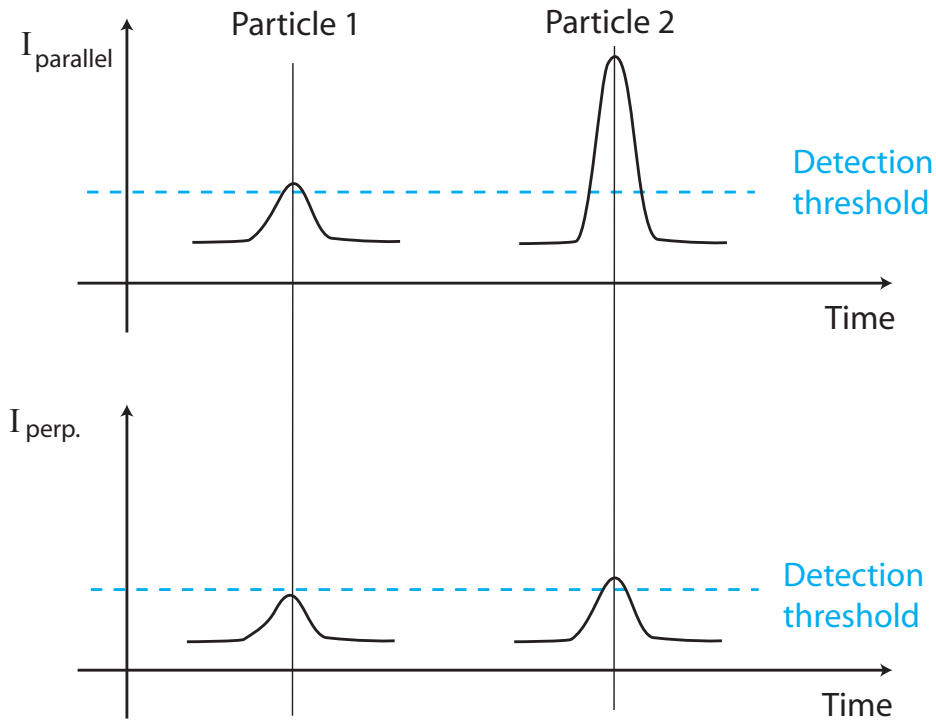

Figure 4.8: *Example for erroneous particle phase identification with the original IODE software. The parallel channel (upper panel) and the perpendicular channel (lower panel) signal are displayed for two hypothetical particles. Particle 1 is counted as a water droplet, whereas particle 2 is counted as an ice crystal, although particle 1 has a higher depolarisation ratio than particle 2.*

Particle 1 generates a parallel channel signal which is only slightly above the detection threshold. As the signal in the perpendicular channel is slightly below the detection threshold, a peak is detected only in the parallel channel, and the particle is automatically counted as a water droplet. Particle 2 generates a generally larger signal, e. g. due to a larger size. A peak is detected in both channels, and the particle can be counted as an ice crystal even if its depolarisation ratio is smaller than the one of particle 1. For typical peak detection thresholds, particles with a depolarisation ratio up to around 0.15 can be counted as water droplets if their parallel signal is close to the peak detection threshold. This is in contradiction to the significantly lower depolarisation threshold used to discriminate between ice and water when a peak is detected in both channels. As a consequence, it has to be assumed that the original detector software underestimates the number of ice counts, especially for small ice crystals.

In the improved version, the peak detection algorithm is applied to the total signal, i. e. the sum of the parallel and the perpendicular channel. The depolarisation is calculated for every detected particle, regardless of its signal intensity in the perpendicular channel. As no peak detection is applied to this channel, the perpendicular signal intensity is directly taken from the raw signal, averaged over 20 data

points around the location of the peak in the total signal. This has the advantage that particles generating a small backscattered signal are not biased towards being counted as water droplets. However, fluctuations in the signals, e. g. from electronic noise, have a larger influence on the resulting depolarisation ratio for weaker signals. Particularly fluctuations in the perpendicular channel can lead to considerable error bars in the depolarisation ratio. This measurement error and its effect on the derived frozen fraction of droplets is adressed in section 4.3.4.

The determination of the best value for the peak detection threshold τ is done by analyzing the background signal (Nicolet, 2008). τ is determined by the mean value μ_{BG} and the standard deviation σ_{BG} of the background signal according to

$$\tau = \mu_{BG} + n \cdot \sigma_{BG}. \tag{4.1}$$

As the background noise is approximately normally distributed in intensity, a measured signal larger than $\tau(n=3)$ has a probability of 99.7% not to belong to the background fluctuation. However, noise fluctuations superimposed e. g. to the flank of a peak or to the valley between two close peaks might nevertheless cross τ and be counted as a particle. In order to reduce such false counts, we used $n=5$ for the data analysis. Doing so, we tolerate missing some particles generating a backscattering signal lower than $\tau(n=5)$. A question that might arise here is whether a reduction in captured particles entails a change in the relative amount of ice crystals and water droplets. In fact, increasing τ beyond $n=5$ to very high values leads to an increase in the frozen fraction f of the droplets. Assuming that larger particles produce higher backscattered intensity, this is not unexpected since frozen droplets can grow in the ZINC chamber until they reach IODE, whereas unfrozen droplets are exposed to a slight subsaturation. However, for detection thresholds τ used in the experiments, the dependence of f on τ is usually negligible. Therefore, we consider $\tau(n=5)$ as a reasonable particle detection threshold, even if not all particles producing a small backscattered signal might be captured.

4.3.2 Data Analysis

We have developed a data analysis program in LabView to determine the frozen fraction f of droplets and the associated error bars. During an experiment, a real-time data file with the raw data from the parallel and the perpendicular channel was recorded by the IODE software for each experimental temperature. Each data file yields one data point in the plots of frozen fraction f as a function of temperature as shown in section 3.3.2. In order to obtain a good number of droplets and ice crystals to calculate the frozen fraction, raw data were collected during one minute roughly corresponding to around 600'000 data points and up to around 3000 captured particles, depending on the aerosol particle concentration in the inlet sample air. This data file was then loaded with the analysis software to perform the data analysis.

One important reason to use an external data analysis program and not perform data analysis online with the IODE software is the issue of slow variations in the background level which could not be resolved so far. Calculation of the depolarisation ratio δ according to equation (3.1) requires the subtraction of the background level from the signals, i. e. precise knowledge of the background level μ_{BG} is essential for the calculation of the correct value of δ. Background signal measured by IODE originates to a small degree from electronic noise with a low average value. Compared to this, a relatively large "DC fraction" originates from stray light from the laser beam reflected inside the chamber. In all experiments, this DC fraction slowly decreased from the beginning to the end of the experiment. The change of μ_{BG} was roughly 10% in around 2 hours. The reason for this decrease is unclear and will be investigated in future work. In any case, the background level subtracted from the measured signal needs to be updated for every data file. Therefore, a background measurement (with only filtered sheath air flowing into the chamber) was always performed after two measurements (i. e. two experimental temperatures). The actual background value at the time when a measurement was taken was then determined by linear interpolation between the background measurements. Analysis of the measured data therefore requires analysis of the background measurements beforehand, which makes an online data analysis impossible.

Background measurements were also used to measure the amount of background counts which have to be subtracted from the measured counts. Such background counts can originate from frost particles forming at the walls and eventually falling into the chamber. Accordingly, the number concentration of background particles captured with IODE is almost negligible at the beginning of an experiment, and increases slowly during the experiment. After 2 to 3 hours of operation, sometimes a rapid increase in background particles determined the end of an experiment. The background level of the signal was always determined from parts of the signal were no background particle counts were present.

A screenshot picture of the user interface of the data analysis software with the most important features highlighted is shown in Fig. 4.9.
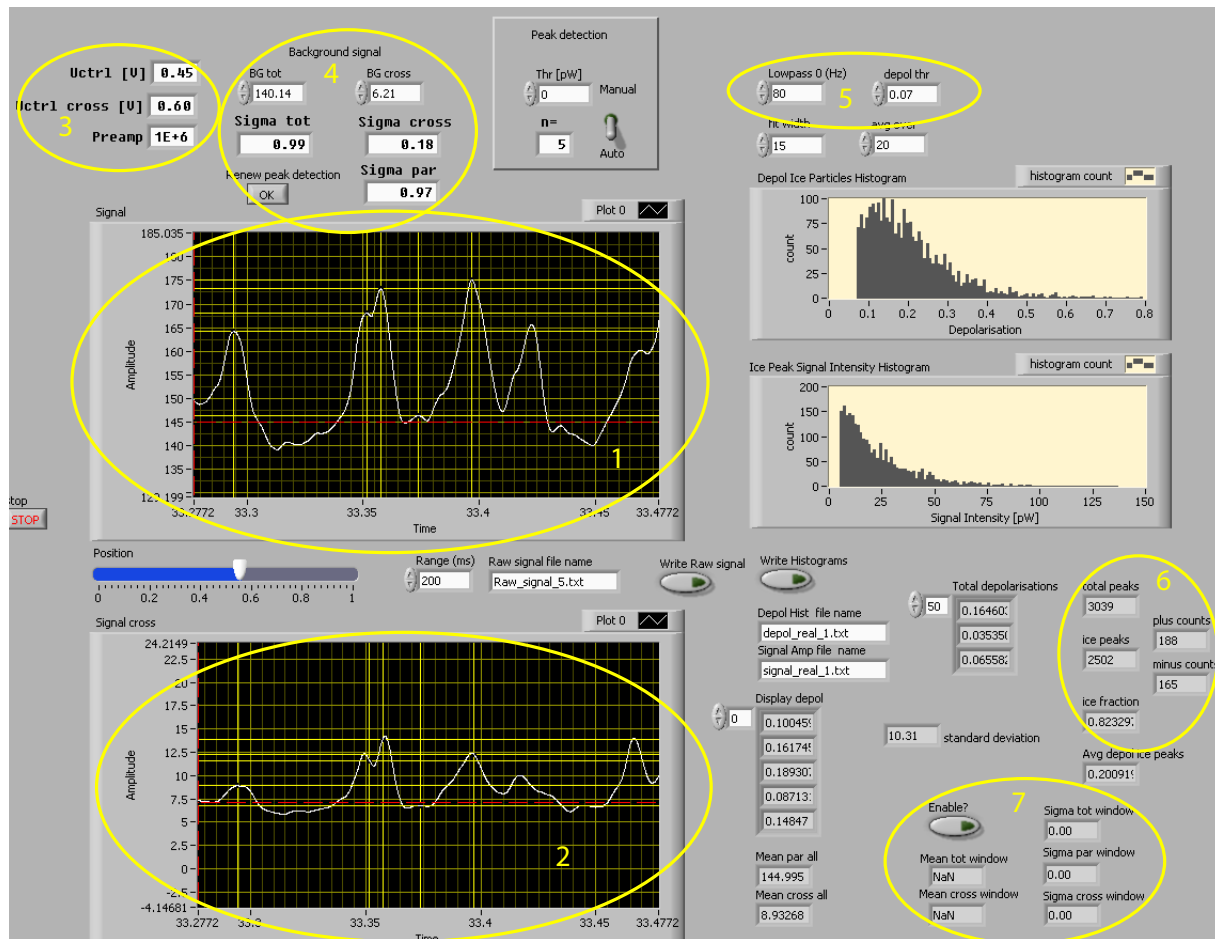

Figure 4.9: *Screenshot picture of the LabView user interface of the data analysis software. The most important functionalities are highlighted: 1 - Time series of the total raw signal measured by IODE (i. e. the sum of the parallel and the perpendicular channel signal). Yellow lines indicate the positions and amplitudes of the peaks identified by the peak detection algorithm. Only the first 5 peaks in the window are displayed. 2 - Same as 1, but separately for the perpendicular channel. 3 - Panel to enter settings for the gains of the photomultipliers and the preamplifier used in the experiment. 4 - Panel to enter the current background signal levels and the standard deviations of the background signals. 5 - Panel to apply a lowpass filter to the signal prior to peak detection, and to define the depolarisation threshold. 6 - Panel indicating the number of total particles and of ice crystals identified in the current sample, plus the derived frozen fraction and indications used to calculate the error bars for f. 7 - Panel indicating mean and standard deviations of the signals in the panels 1 and 2, used for determining background signal levels.*

Panel 3 in Fig. 4.9 is used to enter the gains applied to the photomultiplier tubes (PMTs) of IODE and the preamplifiers. As the backscattered signal in the perpendicular channel is generally smaller than the

one in the parallel channel, the PMT gain of the perpendicular channel (labeled "cross") is set to a higher level than the one of the parallel channel in order to improve the signal to noise ratio. An increase of the gain by 0.15 corresponds to a multiplication of the PMT current by a factor around 10. A preamplifier unit converts the PMT current into a voltage signal from which the intensity of the backscattered light is calculated and displayed in panels 1 and 2. Panel 4 is used to enter the current background signal level for the total signal and the perpendicular channel. Also, the standard deviations of the background signal is entered. These informations are essential for the peak detection algorithm. Panel 5 is used to specify a lowpass filter applied to the raw data prior to the peak detection. Filtering the signal is essential to prevent the peak detection algorithm from counting background noise peaks superimposed to the signal. The peak detection algorithm in the current version of IODE does not discriminate peaks according to their width. Therefore noise peaks have to be removed from the signal by filtering in order to avoid a large number of false counts. As discussed in section 3.2.3, a 80 Hz filter removes components of the noise with a frequency larger than the one corresponding to the width of a typical signal peak (around 12 ms). Noise components with lower frequencies cannot be removed without considerably influencing the signal. Figures 4.10 and 4.11 visualize the effect of the filter. In Fig. 4.10, the cutoff frequency of the filter is set to 80 Hz, whereas in Fig. 4.11, it is set to 1000 Hz. Green vertical lines indicate the locations of the peaks identified by the peak detection algorithm, and the red dashed line indicates the peak detection threshold. Only the first 5 peaks are displayed.
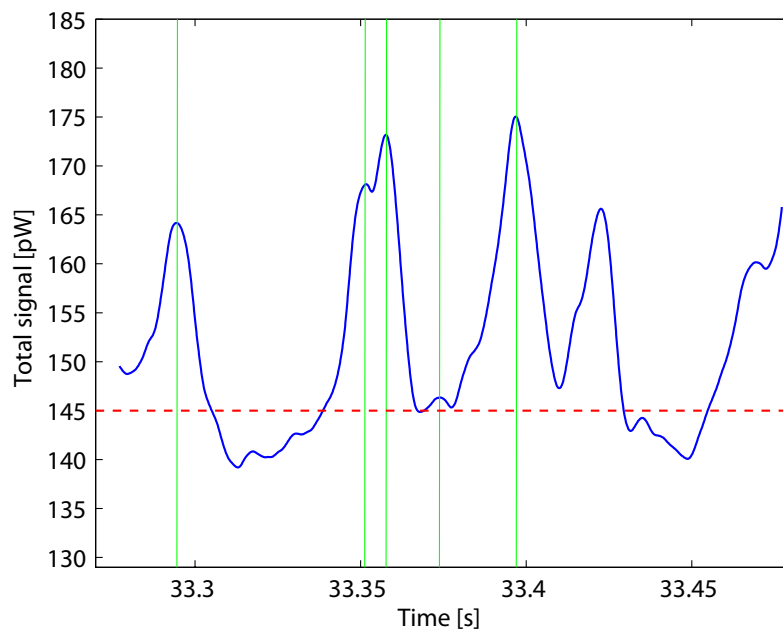

Figure 4.10: *Example of the IODE total signal (sum of parallel and perpendicular channel) during an experiment with 200 nm Kaolinite particles at a temperature of 237 K. A lowpass filter with a cutoff frequency of 80 Hz was applied prior to peak detection. Vertical green lines indicate the locations of peaks identified by the peak detection algorithm. The red dashed line indicates the peak detection threshold.*

Whereas the peak detection algorithm correctly identifies peaks originating from backscattering on particles if the cutoff frequency is set to 80 Hz, it mainly counts peaks from noise superimposed to the signal peaks for a cutoff frequency of 1000 Hz. The data analysis in the present work has therefore been done with a 80 Hz filter.

In panel 5 of Fig. 4.9, also the depolarisation threshold needs to be set. The depolarisation threshold is adressed in section 4.3.3. The resulting total number of counts and the number of ice counts in the loaded sample are displayed in panel 6 of Fig. 4.9. Also, the fraction *f* of ice crystals among all particles is displayed, and two numbers labeled "plus counts" and "minus counts" required to calculate error bars
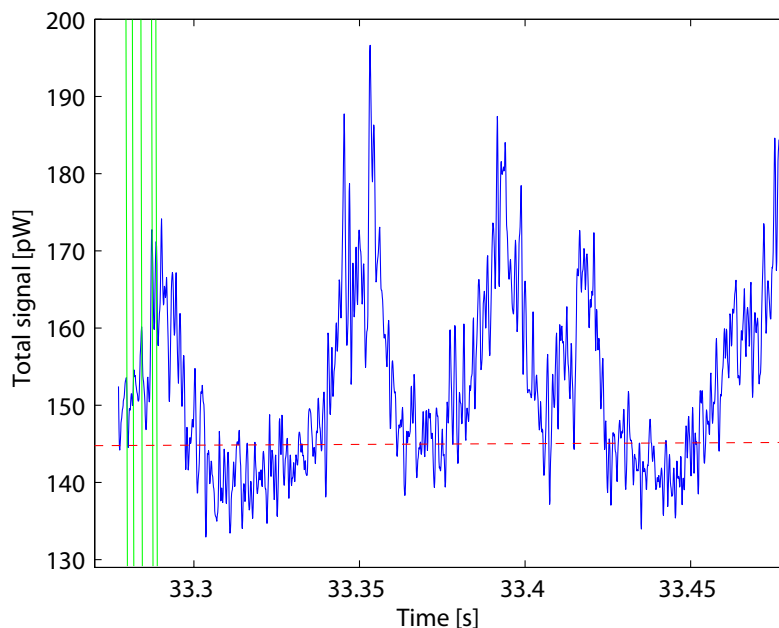
Figure 4.11: *Same as in Fig. 4.10, but with a lowpass filter cutoff frequency of 1000 Hz.*

for f. This will be explained in section 4.3.4.

4.3.3 Depolarisation Threshold

In order to distinguish between liquid droplets and ice crystals by means of the depolarisation, a depolarisation threshold τ_δ is required according to which a measured particle is classified as an ice crystal, if its depolarisation δ is larger than τ_δ, or as a water droplet, if δ is lower than τ_δ. Unfortunately, theory does not provide an unambiguous value for τ_δ: Spherical droplets have a depolarisation ratio of zero or close to zero in an experiment where imperfections in the setup can lead to small measured depolarisations even for spherical particles. However, simulations with (idealized) ice crystals have shown that depending on shape and orientation of the crystals with respect to the detector optics, ice crystals can also exhibit depolarisations close to zero. Therefore, a certain error in the frozen fraction f of droplets has to be expected which cannot be quantified since shape and orientation of ice crystals in the ZINC chamber are unknown. Experiments have shown that the depolarisation of ice crystals in the present experiments is usually large enough that they cannot be miscounted as water droplets. Figure 4.12 shows histograms of the depolarisation of measured particles for two cases. In both cases, more than 95% of the particles were identified as ice crystals.

The experiment in Fig. 4.12a has been done with no supersaturation in IMCA, i. e. the detected ice crystals nucleated in the deposition mode in ZINC. Figure 4.12b shows the case of droplet nucleation in IMCA with 800 nm kaolinite particles and subsequent freezing of practically all droplets at 239.6 K. Figure 4.13 shows a cutout of the total signal (upper panel) and the signal in the perpendicular channel (lower panel) from the experiment in 4.12a.

Both depolarisation histograms in Fig. 4.12 show very little counts at depolarisations that could possibly be attributed to liquid water droplets. However, we have observed lower average depolarisation ratios for frozen droplets than for ice crystals nucleated in the deposition mode at temperatures where f is clearly below 1 (cf. Fig. 3.5). At such temperatures, droplets probably do not necessarily freeze at the beginning of ZINC, if we assume a stochastic contribution to the freezing process (cf. section 3.4). If a droplet only freezes in the lower part of ZINC, it has less time to grow in the ice supersaturated environment of ZINC and to obtain a considerably aspherical shape. Immediately after freezing, droplets
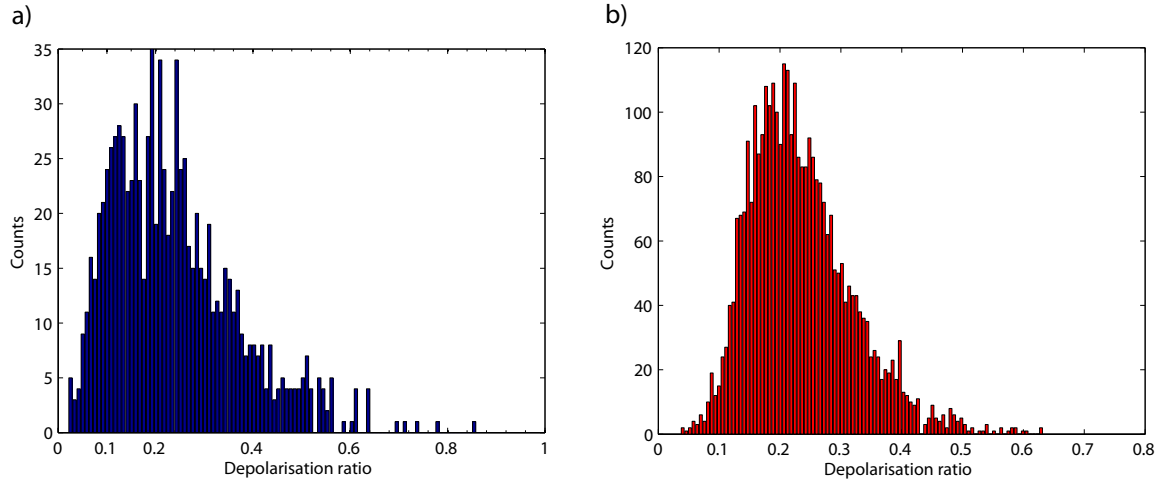
Figure 4.12: *Depolarisation histograms of ice crystals a) nucleated in the deposition mode, and b) nucleated in the immersion mode, measured with IODE.*
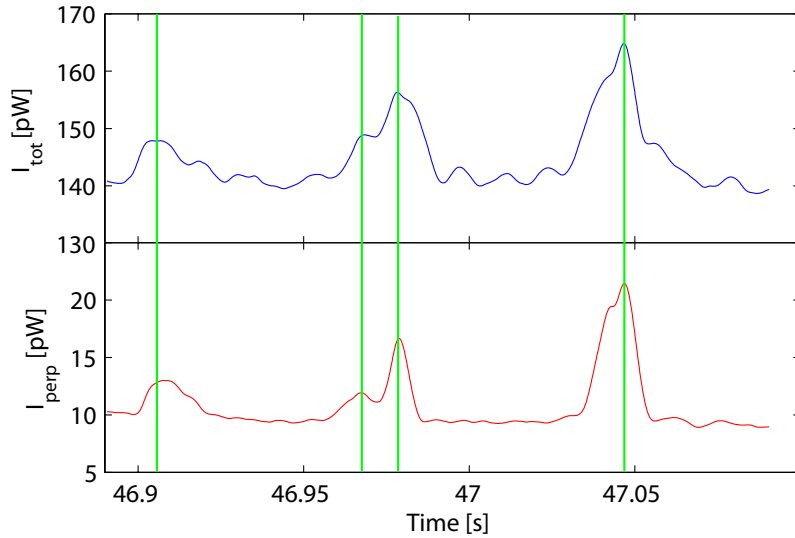

Figure 4.13: *Cutout of the total (upper panel) and perpendicular channel signal (lower panel) for an experiment with ice nucleation in the deposition mode. Vertical green lines indicate the positions of detected peaks in the total signal. According to their depolarisation ratio, all displayed peaks are identified as ice crystals.*

might exhibit a depolarisation ratio that could be misinterpreted as belonging to a liquid droplet. Thus, the largest uncertainty arising in f due to ambiguous classification of particles with low depolarisation can be expected for intermediate values of f. As this error can be considered unimportant for high and low values of f, and f quickly increases with decreasing temperature around the median freezing temperature T_m (for 800 nm kaolinite particles, the slope of f is around 0.5/K), an upper estimate for the error in T_m can be seen in the temperature interval in which f increases from close to 0 to 1. This corresponds to 2 - 3 K in the present experiments.

Two test experiments have been performed in order to find the best value for the depolarisation threshold τ_δ. In the first experiment, ZINC was operated without ice layers at a warm temperature (293 K). $(NH_4)_2SO_4$ particles with a diameter of 100 nm were activated into solution droplets in IMCA. As both cooling units CU1 and CU2 of IMCA were set to 293 K and no subsaturation occurs in the sample air, the droplets do not evaporate until they reach the IODE detector. With this setup, a lower boundary for τ_δ can be found by tuning the depolarisation threshold to the minimum value at which no

ice counts are detected. This minimum value turned out to be $\tau_\delta = 0.07$ in the present experiment. This value is relatively high; In the deposition nucleation experiment shown in Fig. 4.12a, around 5% of the particles are identified as liquid water for $\tau_\delta = 0.07$, although no water droplets are expected to form without supersaturation in IMCA. This suggests that τ_δ should not be larger than 0.07. The second test experiment served to test $\tau_\delta = 0.07$. It was also performed with $(NH_4)_2SO_4$ particles, but at normal operating conditions in ZINC (i. e. ice layers, temperature 253 K at $RH_w \approx 99\%$). An IMCA activation yielded 39 ice counts out of 672 total counts for $\tau_\delta = 0.07$, with background ice counts subtracted. As solution droplets do not homogeneously freeze at temperatures around 253 K, the ice counts have to be considered false ice counts leading to an error of 5.8% in f. $\tau_\delta = 0.07$ appears to be a good compromise between false ice counts with low δ and false water counts with high δ, as these make up for around 5 - 6% in both cases. A different value for τ_δ would result in a bias towards either false ice counts or false water counts. In fact, the median freezing temperature of droplets is not very sensitive to an uncertainty in τ_δ, as has already been discussed in section 3.3.3.

4.3.4 Error Analysis

There are several potential sources of error in the frozen fraction f of droplets. These can be:

- Uncertainty in the value of the peak detection threshold

- Uncertainty in the depolarisation threshold τ_δ

- Measurement errors in the signal intensities

- Contributions to measured ice counts from deposition nucleation

The first two potential error sources are difficult to quantify and have been discussed in sections 4.3.1 and 4.3.3. A method to estimate the contribution of deposition nucleation to the measured ice counts has been discussed in section 3.3.1. The major source of error, however, is the measurement error in the signal intensities of the parallel and the perpendicular channel of IODE. It has been shortly discussed in section 3.3.2 and is adressed in a more detailed manner in the present section.

Electronic noise leads to a measurement uncertainty in the signal intensities $I_\parallel$ and $I_\perp$ of the parallel and the perpendicular channel of IODE. As these fluctuations approximately follow a normal distribution in intensity (Nicolet, 2008), the corresponding standard deviation of the signal is taken as the measurement error of each channel, i. e. $\Delta I_\parallel = \sigma_\parallel$ and $\Delta I_\perp = \sigma_\perp$. These measurement errors give rise to an error $\Delta\delta$ in the depolarisation ratio δ. As the measurement errors in the two channels are independent from each other, $\Delta\delta$ can be obtained with the following error propagation:

$$\Delta\delta = \sqrt{\left(\frac{\partial\delta}{\partial I_\perp}\Delta I_\perp\right)^2 + \left(\frac{\partial\delta}{\partial I_\parallel}\Delta I_\parallel\right)^2}\,. \tag{4.2}$$

This is based on the assumption that the first derivatives of δ can be considered as constant within the considered variations in the signals. As δ is given by

$$\delta = \frac{I_\perp}{I_\parallel + I_\perp}\,,$$

equation (4.2) can be written as

$$\Delta\delta = \frac{1}{(I_\parallel + I_\perp)^2} \cdot \sqrt{(I_\parallel\Delta I_\perp)^2 + (I_\perp\Delta I_\parallel)^2}\,. \tag{4.3}$$

The effect of this error in depolarisation on the number of ice and water counts identified by IODE depends on the depolarisation of individual particles. This is illustrated in Fig. 4.14.
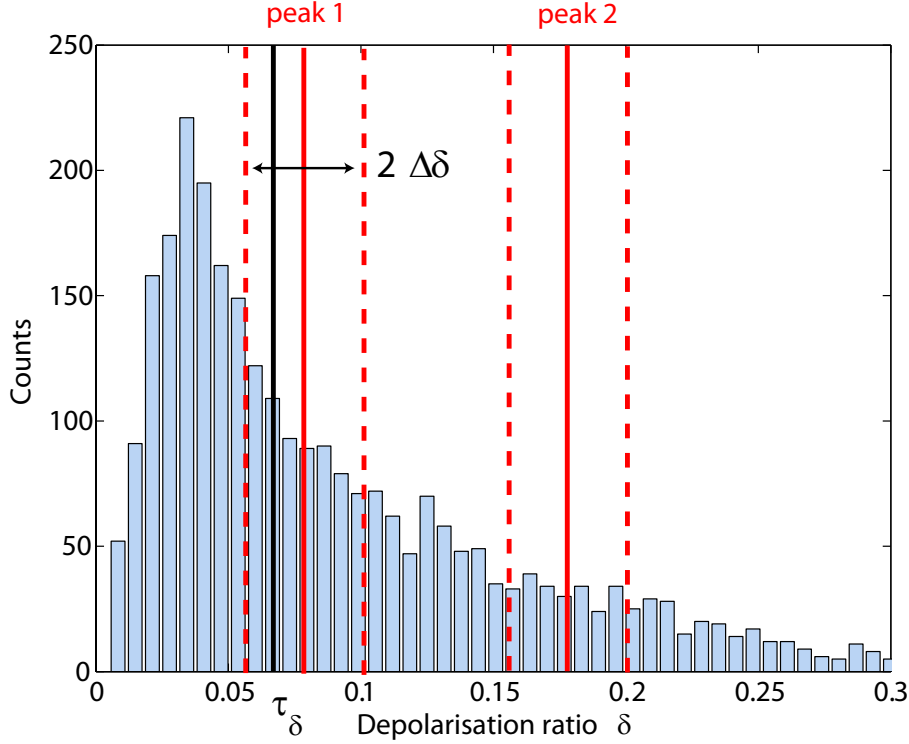
Figure 4.14: *Example of a depolarisation histogram to illustrate the effect of the measurement error in the depolarisation δ on the counting of ice crystals and water droplets. The black vertical line indicates the depolarisation threshold τ_δ. Red solid lines denote the measured depolarisation of two individual peaks, and red dashed lines indicate the measurement error in δ.*

An example of a depolarisation histogram is displayed together with red vertical lines indicating the depolarisation of two individual peaks. The dashed red lines exemplarily indicate the measurement error $\Delta\delta$. The black vertical line indicates the depolarisation threshold discriminating between ice crystals and water droplets. Peak 2 with a depolarisation between 0.15 and 0.2 is clearly an ice crystal: Subtracting the measurement error Δ_δ from its δ value still yields a δ value clearly above the depolarisation threshold. Peak 1 is also counted as an ice crystal, but it might also belong to a water droplet within the measurement error. Thus, the measurement error in δ influences the discrimination between ice crystals and water droplets for peak 1, but for peak 2 which has a depolarisation far from the depolarisation threshold, it is of no influence.

We applied the following method to calculate the resulting error bars in the frozen fraction f of droplets: For every detected signal peak, its depolarisation ratio δ and the corresponding measurement error $\Delta\delta$ is determined. If $\delta > \tau_\delta$ and $\delta - \Delta\delta < \tau_\delta$, then this peak adds 1 to a number N_- of potentially miscounted ice peaks. Vice versa, if $\delta < \tau_\delta$ and $\delta + \Delta\delta > \tau_\delta$, then it adds 1 to a number N_+ of potentially miscounted water droplets. f is calculated as the number N_i of measured ice crystals divided by the total number N_{tot} of detected particles in the data file. The real number of ice crystals in this data file then lies between $N_i - N_-$ and $N_i + N_+$. This leads to an error bar in f ranging between f_- and f_+, if f_- and f_+ are given by

$$f_- = f - \frac{N_-}{N_{tot}} \quad \text{and} \quad f_+ = f + \frac{N_+}{N_{tot}}.$$

For depolarisation histograms with a large number of peaks with a depolarisation close to τ_δ, this error bar can be large. This is mainly the case for intermediate values of f, where error bars with a size close to 0.4 have been observed for some data points (see section 4.4 and 3.3.2). Due to these error bars and the difficulty to precisely assess the contribution from deposition nucleation to the measured ice crystals (see section 4.4), it has not been possible so far to reliably detect the onset of freezing.

4.4 Deposition Nucleation - The Issue of Unactivated Aerosol Particles

Experimental results obtained in the present work are mainly discussed in section 3.3. In section 3.3.2, the temperature dependent frozen fraction f of droplets has been plotted after subtraction of an estimated contribution from deposition nucleation in ZINC. The corresponding results without this correction are plotted in Fig. 4.15, 4.16 and 4.17.
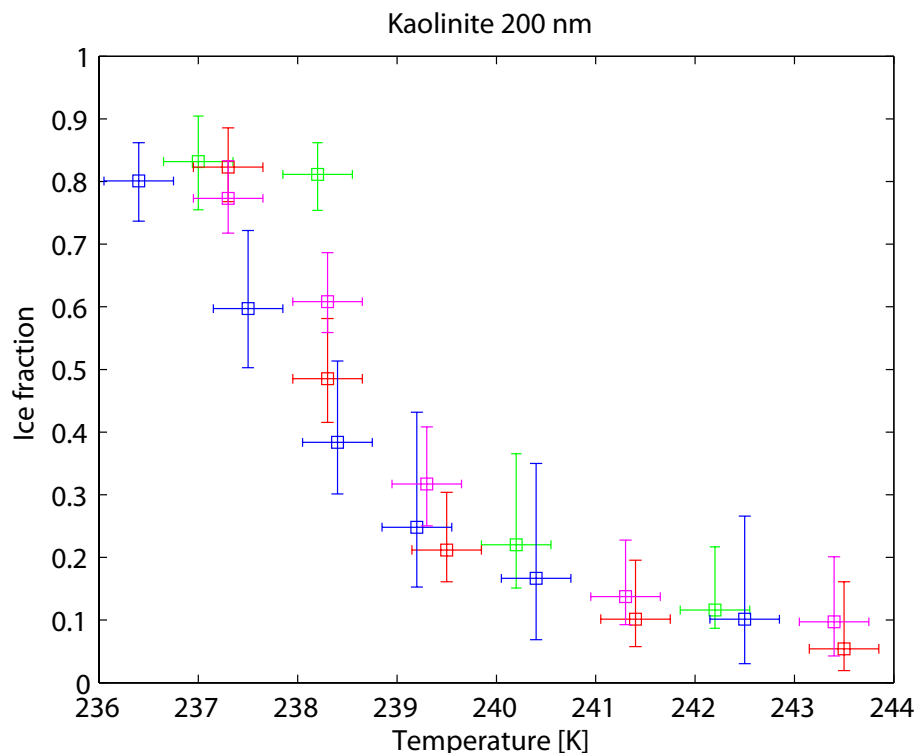

Figure 4.15: *Temperature dependent frozen fraction f of droplets for immersed 200 nm kaolinite particles. Different marker colours represent different experiments.*

Different marker colours indicate different experiments each of which comprises a series of 3 to 6 data points. Each series was started at the lowest temperature, and the temperature was increased after each data point. A total of 4 or 5 series was performed for each aerosol particle size in order to obtain more significant data sets. In Fig. 4.15, 4.16 and 4.17 it can be seen that f does not rapidly approach zero for increasing temperature, but only slowly decreases below $f = 0.2$. None of the drop freezing models discussed in section 3.4 captures this slow decrease of f. Theory describing heterogeneous freezing of droplets probably cannot account for this behaviour, unless parameterizations of surface properties (e. g. the surface distribution of active sites in the active site model) are drastically changed. Figure 4.18 qualitatively illustrates the effect of a hypothetical change in the active site (AS) surface distribution on the temperature dependence of the ice fraction f.

The black curves show an AS surface density as a fuction of the contact angle and an ice fraction as a function of temperature as obtained with the active site model in section 3.4. If, instead of a rapidly decaying AS surface density towards small contact angles, the AS surface density remains constant for a certain contact angle interval, a small fraction of droplets can freeze at significantly higher temperature than the median freezing temperature T_m. This scenario is visualized with the red curves. In this case, the active site model would predict a decrease of f more similar to the measured one for increasing temperatures. However, no plausible physical argument would suggest an active site surface density
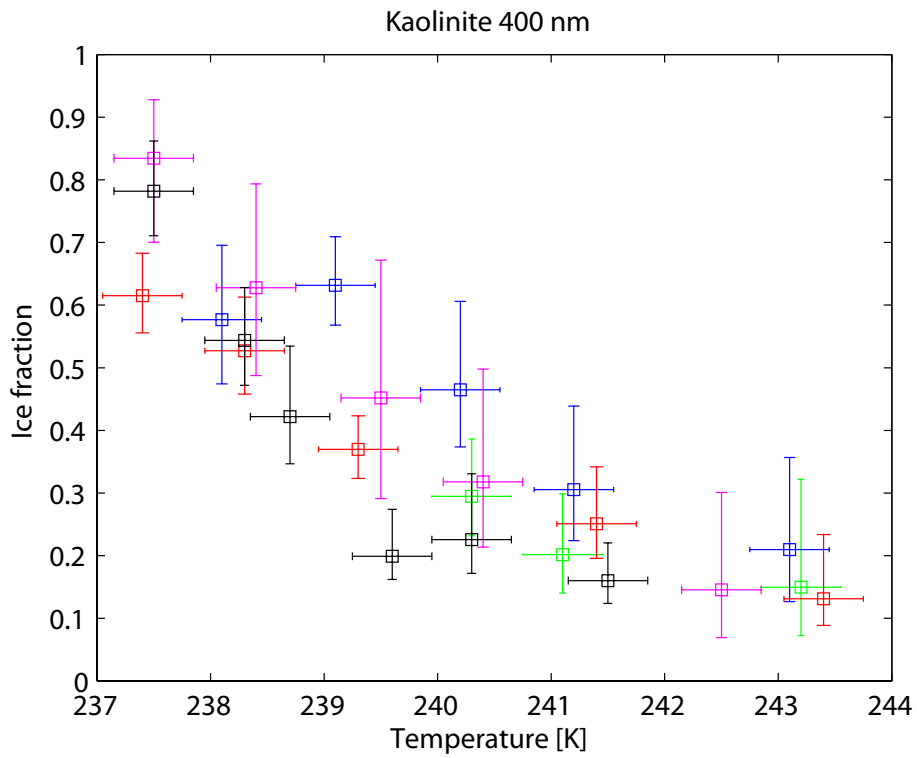
94

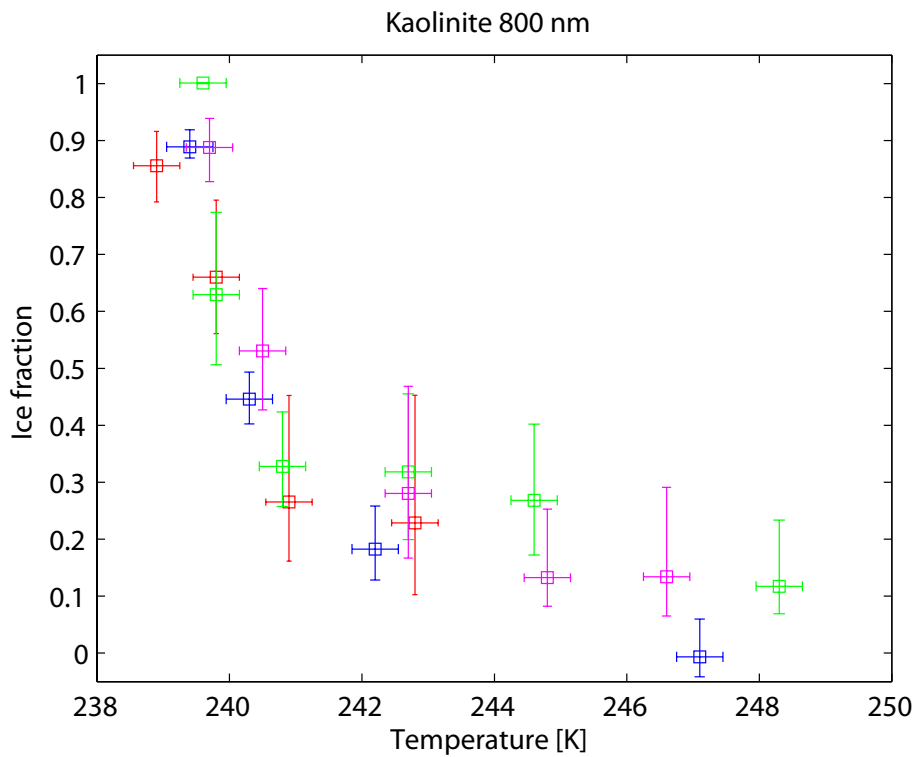**Figure 4.16:** *Same as Fig. 4.15 for 400 nm kaolinite particles.*

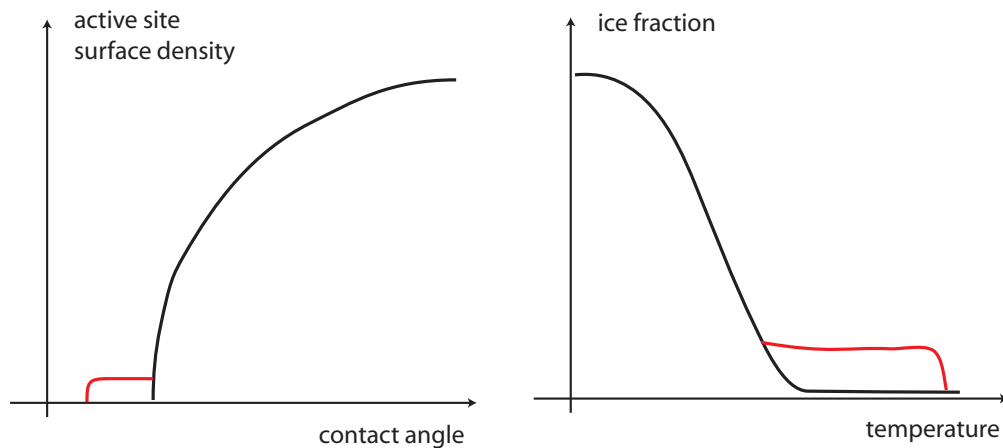**Figure 4.17:** *Same as Fig. 4.15 for 800 nm kaolinite particles.*

Figure 4.18: *Qualitative illustration of the influence of a significant change in the active site surface distribution on the temperature dependence of the ice fraction f. An (unrealistic) tail towards low contact angles can shift the decay of f to larger temperatures.*

curve similar to the one displayed by the red curve. Therefore, it is more likely that the remaining ice counts at higher temperatures do not originate from droplet freezing, but from deposition nucleation on unactivated particles in ZINC, which becomes active around 243 K for kaolinite particles (Welti et al., 2009). This raises the question if and how unactivated particles get into the ZINC chamber although aerosol particles are CCN activated in IMCA. Although we do not have direct evidence for unactivated, dry aerosol particles in ZINC during an IMCA activation, some observations suggest that probably not all aerosol particles activated in IMCA are still immersed in a cloud droplet when they arrive in the ZINC chamber. On one hand, we have observed that for 200 nm kaolinite particles, the number concentration of aerosol particles in the inlet sample air had to be chosen significantly higher than for 800 nm particles in order to obtain a comparable number of detected peaks. Obviously, the detection efficiency of IODE is smaller in experiments with smaller aerosol particles. An explanation for this can be that for small aerosol particles, a larger fraction of nucleated droplets evaporate in the lower part of IMCA or in ZINC than for large aerosol particles.

On the other hand, we attempted to measure the size distribution of particles arriving at the bottom of ZINC during an IMCA activation with 200 nm illite particles at 258 K. An aerodynamic particle sizer (APS, TSI 3321) was connected to the exit of ZINC, and the size distribution of particles was measured for increasing IMCA supersaturation. The result can be seen in Fig. 4.19.

At low supersaturation in IMCA, droplets evaporate before they reach the APS, and a distribution of small particles can be seen in the APS size spectrum. As the IMCA supersaturation increases, a second mode appears at large particle sizes, corresponding to water droplets nucleated in IMCA. The fact that despite large IMCA supersaturations, a large number of small particles is detected by the APS suggests that a considerable fraction of the particles does not reach the APS as immersed in a droplet. However, the APS measurement might not be quantitative since temperature and relative humidity of the sample air cannot be well controlled between the exit of ZINC and the detection volume of the APS. The APS might therefore overestimate the number of unactivated particles present in ZINC.

These indications suggesting the presence of unactivated, dry aerosol particles in ZINC even during an IMCA activation are contradictory to the results of droplet evolution calculations presented in section 2.5.3. According to these calculations, liquid droplets should not completely evaporate before reaching the IODE detector for typical IMCA supersaturations generated in the experiments. If dry aerosol particles really are present in ZINC, the mismatch between the calculation and reality raises the question if the droplet evolution calculation or the CFD simulation make assumptions that do not really represent
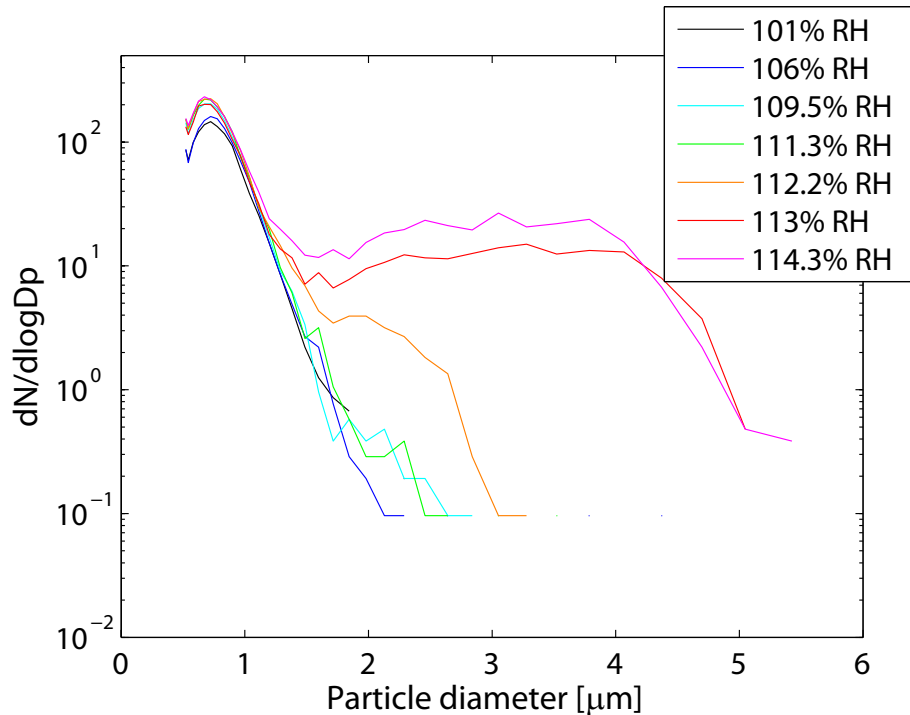
Figure 4.19: *APS size distribution of particles measured at the bottom of ZINC for different IMCA supersaturations.*

reality in the experiment. Two main assumptions might lead to an overestimation of the droplet size at the bottom of the IMCA chamber in the calculation:

- The IDL routine calculating the droplet evolution based on conditions calculated with the FLU-ENT simulation does not include the nucleation process itself. The assumption is made that a small droplet with a diameter of 1 μm is injected into the IMCA chamber. If CCN activation of injected aerosol particles immediately occurs upon entrance of the particles into the supersaturated region of IMCA, the error imported by this simplification is negligible. However, if cloud droplets nucleate with a certain delay, droplet growth can be overestimated in the IDL calculation.

- In the FLUENT simulation, liquid water humidification of the warm part of IMCA and ice coating of the cold part are seamlessly connected at the position where the IMCA wall temperature is at $T = 273\,\mathrm{K}$. This cannot precisely be achieved in reality. As the water level sensor used to terminate water pumping into ZINC and IMCA during the icing routine is not mounted directly to the chamber, but only indirectly senses the water level, the level up to which the ice coating of the IMCA wall reaches cannot be determined with great precision. A small region with bare IMCA walls providing no water vapour supply can establish which might lead to an increased droplet evaporation compared to the calculation.

The importance of the former issue is supported by the observation of a higher inlet number concentration of small aerosol particles required to obtain a certain number of hydrometeors detected by IODE, as compared to larger aerosol particles. If all particles immediately nucleated cloud drops, and the better CCN activity of larger particles did not play a role in the IMCA environment, droplets would reach similar sizes in IMCA for all aerosol particle sizes. Then, there would be no reason for the aforementioned observation. The latter issue is technical and will be resolved in future experiments.

Furthermore, experiments with mineral dust particles coated with soluble substances are planned to assess the importance of deposition nucleation in the present experimental setup. Solution droplets ex-

posed to subsaturation with respect to water do not leave dry aerosol particles in ZINC, as the relative humidity in the experiment never decreases below the efflorescence point of typical soluble substances found in the atmosphere. Therefore, deposition nucleation can be ruled out, and comparison with the experimental results of the present work can give information about the importance of unactivated aerosol particles in the present experimental setup.

Chapter 5

Conclusions

5.1 The IMCA Chamber

In the present thesis, we have developed a new instrument to extend the ZINC setup for experiments on immersion freezing. The IMCA chamber has been designed as a vertical extension on top of the ZINC chamber which nucleates cloud droplets with single immersed IN, and continuously cools them to the temperature in ZINC. This method of immerging single aerosol particles into cloud droplets by CCN activation of the particles and gradually cooling them mimics immersion freezing in the atmosphere. Computational fluid dynamics simulations have been performed to find the required chamber dimensions and to characterize flow, temperature and relative humidity conditions in IMCA. Calculations of the evolution of cloud droplets nucleated at the beginning of the supersaturated region in IMCA have shown that for typical conditions used in the experiments, droplets grow large enough in the top part of IMCA that they are not lost due to evaporation before they reach the detector at the bottom of ZINC. Calculations of droplet evolution for varying conditions in IMCA have shown that a top temperature of 313 K with a top wall temperature difference of $dT = 20\,\mathrm{K}$ or more at a total flow rate of 5 lpm are favourable for droplet growth. It has also been shown that precooling of the sample and sheath air does not significantly increase the final droplet radius. Although for decreasing inlet temperature, the peak supersaturation at the top of the chamber increases, the reduced temperature also reduces the efficiency of the diffusive transport. Finally, we have excluded a significant influence of the consumption of water vapour by growing droplets on the relative humidity in the supersaturated area of IMCA. Therefore, the simulated supersaturation values can be taken as representative for the real conditions in IMCA.

Experiments with IMCA coupled to ZINC have proven that nucleation and sufficient growth of cloud droplets can be achieved with the IMCA chamber. The appearance of particles of detectable size (i. e. frozen or unfrozen droplets) in the signal of the IODE detector directly correlates with the level of supersaturation applied in IMCA. However, APS particle size distributions measured after the exit of ZINC suggest that not all particles entering IMCA reach the detector as immersed in a droplet or an ice crystal. A possible reason for this contradiction to simulation results could be the assumption made in the droplet evolution calculation, that aerosol particles immediately nucleate cloud droplets upon entrance in the IMCA chamber. CCN activation of aerosol particles with a WCPC prior to entrance in IMCA might reduce uncertainties in the final droplet size due to the short exposure of particles to large supersaturation in IMCA. However, test experiments have not shown a reduction of the IMCA supersaturation required to observe nucleated droplets with IODE. This suggests that droplets leaving the WCPC evaporated before reaching the supersaturated region of IMCA. Therefore, experiments reported in this study have been carried out without WCPC activation.

5.2 Immersion Freezing of Size Selected Kaolinite Particles

First successful experiments on immersion freezing have been carried out with size selected kaolinite particles. The fraction of frozen droplets has been inferred from single particle depolarisation measurements with the IODE detector. Measurements with three selected particle diameters between 200 nm and 800 nm have not revealed small kaolinite particles to be particularly efficient IN. The effect of IN size on IN efficiency is clearly visible, although not very strong: Median freezing temperatures range between 238 K for 200 nm particles and 240 K for 800 nm particles. If no supersaturation is established in IMCA, ice crystals nucleated in the deposition mode are detected below temperatures around 245 K. Upon applying supersaturation to IMCA, deposition nucleation is substantially suppressed, but so far, we could not determine from the IODE ice counts if it vanishes completely or if a small contribution remains due to dry particles reaching ZINC. The latter is supported by the observation that below a value around 0.2, the ice fraction f only slowly decays to zero for increasing temperature. A contribution from deposition nucleation to the ice counts has been estimated and subtracted from the measured counts, in order to isolate immersion freezing and to equate the corrected ice fraction with the fraction of droplets frozen by immersion freezing. A difference between the mean depolarisation ratio of ice crystals nucleated in the deposition mode and the one of ice crystals nucleated in the immersion mode could be observed. The lower depolarisation of frozen droplets is most likely due to a lower asphericity as compared to ice crystals directly nucleated from the vapour phase.

Considerable uncertainty in f arises from the fact that histograms of the measured single particle depolarisations usually exhibit a considerable amount of particles with depolarisations around the depolarisation threshold $\tau_\delta = 0.07$ used in this study. As a consequence, the measurement error in the depolarisation ratio δ and a potential error in τ_δ have a significant effect on f. However, around $f = 0.5$, f increases steeply enough for decreasing temperatures, that for the uncertainty in the median freezing temperature T_m due to the uncertainty in f, an upper boundary of 1 K can be estimated. Whereas the determination of T_m does not suffer strongly from the measurement uncertainties, it has not been possible to reliably determine the onset of freezing so far due to the measurement uncertainties and the difficulty to precisely assess the contribution from deposition nucleation to f.

The measured temperature dependence of f has been fitted to nucleation theory with four different models representing different assumptions on the IN surface structure between the stochastic and the singular hypothesis. All fits have been calculated with the entire set of data, i. e. the fit parameters depend on the IN species, but not on particle size. The first three models are based on CNT. Assuming a constant contact angle for all IN does not well represent the data. A lognormal distribution of contact angles among the IN yields a better fit, but underestimates the size dependence of f. This suggests that the size dependence of f is not only based on the larger surface area of larger IN, but that larger IN have an increased probability to carry efficient nucleating sites. A third model distributing active sites with different contact angles on the IN surface better captures the size dependence of f. Fitting the data with this model yields active sites with contact angles larger than $\alpha \simeq 80°$ to occur with a significant surface density. A fourth, deterministic model distributing active sites with distinct freezing temperatures on the IN surface has also been tested. Whereas the RMS error is lowest for the deterministic model compared to the other models, the deterministic model suffers from the weakness that although T_m increases correctly with increasing IN size, the onset of freezing does not depend on IN size. Based on these considerations, we suggest that size effects on the IN efficiency of kaolinite in the immersion mode can be captured with a nucleation model based on CNT in combination with a suitable surface distribution of active sites with different contact angles.

In order to compare our results to previous studies on the IN efficiency of kaolinite particles in the immersion mode, we have extrapolated the active site model to hypothetically large particle sizes of 20 μm, assuming that one large IN may substitute many smaller particles in suspension droplets. Extrapolation yields an increase of T_m with increasing particle size, but it also shows a saturation around $T_{m,\mathrm{max}} = 242\,\mathrm{K}$. We conclude that the present study does not support the high T_m values for kaolinite found by Pitter and Pruppacher (1973) of 249 K, whereas it is in reasonable agreement with Hoffer

(1961). We suppose that this disagreement with Pitter and Pruppacher (1973) is due to large differences in the experimental technique.

5.3   Outlook

First successful experiments with the IMCA chamber together with the IODE detector have shown that the present experimental setup is suitable for investigating the IN efficiency of aerosol particles in the immersion mode. However, more work is needed to fully characterize the setup and to reduce uncertainties in the measurements. Also, the issue of unactivated particles leaving IMCA has to be adressed to assess the contribution of deposition nucleation to the measurements in more detail. Information on the droplet size at different positions in ZINC will be available when a detection channel for laser light scattered in the forward direction will be implemented in IODE. Improvements to the performance of the IODE detector are planned in order to reduce the large measurement uncertainties and to better resolve the onset of freezing. This will predominantly be addressed at the level of peak detection. Once the experimental setup is optimized, further experiments are planned with different mineral dust species. Furthermore, different vertical positions in ZINC for measuring the frozen fraction of droplets will yield information on the time dependence of immersion freezing. This will help to decide whether a CNT-based freezing model like the active site model is required to satisfyingly describe immersion freezing, or if a simpler deterministic model can be favoured. Moreover, since a field version of the ZINC chamber is operational, a future deployment of IMCA in field campaigns might be envisaged.

Appendix A

Parameters for the Calculation of Droplet Evolution

For correct calculation of diffusional growth or evaporation of water droplets, it is necessary to take into account the dependencies of all physical parameters on temperature, pressure etc. In the following, data sets and relations required for the calculations in section 2.4 are listed.

A.1 Heat Capacity c_p of Liquid Water

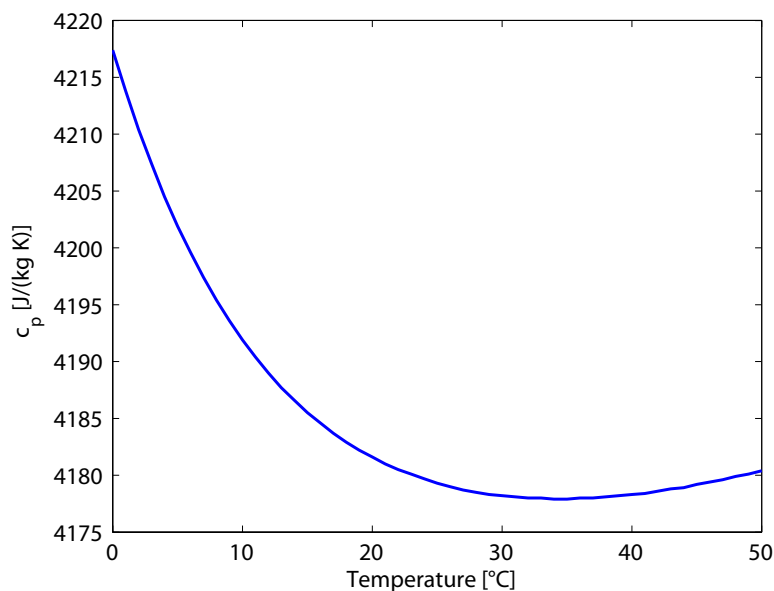For temperatures between 0°C and 50°C, data for c_p can be found in Lide (2008):

Figure A.1: *Heat capacity c_p of liquid water (Lide, 2008)*

For $T < 0$°C, Angell et al. (1982) provide data for c_p of liquid water, given in Tab. A.1.

Temperature [°C]	c_p [J kg^{-1} K^{-1}]
-37	5678
-36	5483
-35	5339
-34	5244
-33	5078
-31	4911
-28	4694
-23	4522
-18	4372
-13	4272
-8	4244

Table A.1: *Heat capacity c_p for liquid water for temperatures below 0°C (Angell et al., 1982)*

A.2 Surface Tension $\sigma_{w,a}$

The surface tension of a water surface surrounded by humid air can be parameterized as a function of temperature by

$$\sigma_{w,a}(T) = -1.57142 \times 10^{-4} T + 0.0762857,$$

with T in °C (Pruppacher and Klett, 1997).

A.3 Latent Heat of Evaporation

For $T > 0$°C, Pruppacher and Klett (1997) provide the following function for the latent heat of evaporation of water:

$$L_e(T) = 2.498 \times 10^6 - 2.346 \times 10^3 T,$$

with T in °C and $L_e(T)$ in J kg^{-1}. For $T < 0$°C, tabulated data from Rogers and Yau (1996) can be interpolated, which are given in Tab. A.2.

Temperature [°C]	L_e [10^6 J kg^{-1}]
-40	2.603
-30	2.575
-20	2.549
-10	2.525
0	2.498

Table A.2: *Latent heat of evaporation of water for $T < 0$°C (Rogers and Yau, 1996)*

A.4 Water Density

Figure A.2 shows the density ρ_w of water as a function of temperature. For $T > 0$°C, data are provided in Toolbox (2005c), for $T < 0$°C in Hare and Sorensen (1987).

A.5 Water Vapour Pressure

The equilibrium water vapour pressure above a flat water surface, $e_{sat,w}$, as a function of temperature has been parameterized by Murphy and Koop (2005) with the following function:
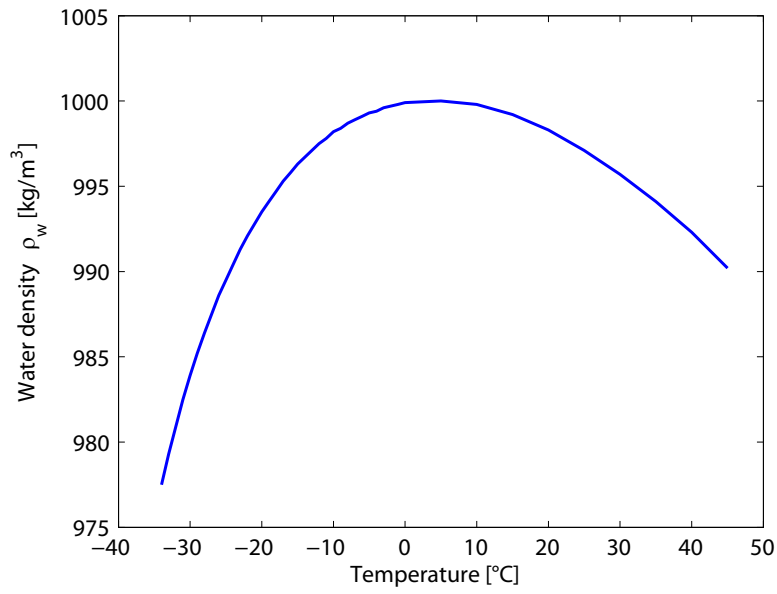
Figure A.2: *Water density* ρ_w *according to data from Hare and Sorensen (1987) and Toolbox (2005c).*

$$\ln\left(\frac{e_{sat,w}(T)}{[\text{Pa}]}\right) = 54.842763 - \frac{6763.22}{T} - 4.21\ln(T) + 0.000367\,T$$
$$+ \tanh[0.0415(T - 218.8)]\left(53.878 - \frac{1331.22}{T}\right.$$
$$\left. - 9.44523\ln(T) + 0.014025\,T\right) \tag{A.1}$$

Bibliography

Albrecht, B. A.: Aerosols, Cloud Microphysics, And Fractional Cloudiness, Science, 245, 1227–1230, 1989.

Alty, T. and Mackay, C. A.: The accommodation coefficient and the evaporation coefficient of water, Proceedings Of The Royal Society Of London Series A-Mathematical And Physical Sciences, 149, 0104–0116, 1935.

Angell, C. A., OGUNI, M., and SICHINA, W. J.: Heat-Capacity Of Water At Extremes Of Supercooling And Superheating, Journal Of Physical Chemistry, 86, 998–1002, 1982.

Archuleta, C. M., DeMott, P. J., and Kreidenweis, S. M.: Ice nucleation by surrogates for atmospheric mineral dust and mineral dust/sulfate particles at cirrus temperatures, Atmos. Chem. Phys., 5, 2617–2634, 2005.

Bundke, U., Nillius, B., Jaenicke, R., Wetter, T., Klein, H., and Bingemer, H.: The fast Ice Nucleus chamber FINCH, Atmospheric Research, 90, 180–186, 2008.

Connolly, P. J., Mohler, O., Field, P. R., Saathoff, H., Burgess, R., Choularton, T., and Gallagher, M.: Studies of heterogeneous freezing by three different desert dust samples, Atmos. Chem. Phys., 9, 2805–2824, 2009.

Cooper, W. A.: Possible Mechanism For Contact Nucleation, Journal Of The Atmospheric Sciences, 31, 1832–1837, 1974.

Cziczo, D. J., Stetzer, O., Worringen, A., Ebert, M., Weinbruch, S., Kamphus, M., Gallavardin, S. J., Curtius, J., Borrmann, S., Froyd, K. D., Mertes, S., Mohler, O., and Lohmann, U.: Inadvertent climate modification due to anthropogenic lead, Nature Geoscience, 2, 333–336, 2009.

Davies, C. N.: Fundamentals of aerosol science, chap. Evaporation of airborne droplets, John Wiley & Sons, Inc., New York, USA, 1978.

DeMott, P. J., Cziczo, D. J., Prenni, A. J., Murphy, D. M., Kreidenweis, S. M., Thomson, D. S., Borys, R., and Rogers, D. C.: Measurements of the concentration and composition of nuclei for cirrus formation, Proceedings Of The National Academy Of Sciences Of The United States Of America, 100, 14 655–14 660, 2003a.

DeMott, P. J., Sassen, K., Poellot, M. R., Baumgardner, D., Rogers, D. C., Brooks, S. D., Prenni, A. J., and Kreidenweis, S. M.: African dust aerosols as atmospheric ice nuclei, Geophys. Res. Lett., 30, 2003b.

Denman, K. L., Brasseur, G., Chidthaisong, A., Ciais, P., Cox, P. M., Dickinson, R. E., Hauglustaine, D., Heinze, C., Holland, E., Jacob, D., Lohmann, U., Ramachandran, S., da Silva Dias, P. L., Wofsy, S. C., and Zhang, X.: Climate Change 2007: The Physical Science Basis. Contribution of Working Group 1 to the Fourth Assessment Report of the Intergovernmental Panel on Climate Change, chap. Couplings Between Changes in the Climate System and Biogeochemistry, Cambridge University Press, Cambridge, United Kingdom and New York, NY, USA, 2007.

Deshler, T. and Vali, G.: Atmospheric Concentrations Of Submicron Contact-Freezing Nuclei, Journal Of The Atmospheric Sciences, 49, 773–784, 1992.

Diehl, K. and Wurzler, S.: Heterogeneous drop freezing in the immersion mode: Model calculations considering soluble and insoluble particles in the drops, J. Atmos. Sci., 61, 2063–2072, 2004.

Diehl, K., Matthias-Maser, S., Jaenicke, R., and Mitra, S. K.: The ice nucleating ability of pollen: Part II. Laboratory studies in immersion and contact freezing modes, Atmospheric Research, 61, 125–133, 2002.

Durant, A. J. and Shaw, R. A.: Evaporation freezing by contact nucleation inside-out, Geophys. Res. Lett., 32, 2005.

Ferek, R. J., Garrett, T., Hobbs, P. V., Strader, S., Johnson, D., Taylor, J. P., Nielsen, K., Ackerman, A. S., Kogan, Y., Liu, Q. F., Albrecht, B. A., and Babb, D.: Drizzle suppression in ship tracks, Journal Of The Atmospheric Sciences, 57, 2707–2728, 2000.

Fletcher, N. H.: On Contact Nucleation, Journal Of The Atmospheric Sciences, 27, 1098–&, 1970.

FLUENT: FLUENT 6.2 User's Guide, Fluent Inc., Centerra Resource Park, 10 Cavendish Court, Lebanon, NH 03766, USA, 2005.

Forster, P., Ramaswamy, V., Artaxo, P., Berntsen, T., Betts, R., Fahey, D. W., Haywood, J., lean, J., Lowe, D. C., Myhre, G., Nganga, J., Prinn, R., Raga, G., Schulz, M., and Van Dorland, R.: Climate Change 2007: The Physical Science Basis. Contribution of Working Group I to the Fourth Assessment Report of the Intergovernmental Panel on Climate Change, chap. Changes in Atmospheric Constituents and in Radiative Forcing, Cambridge University Press, Cambridge, United Kingdom and New York, NY, USA, 2007.

Fuchs, N.: Velocity of evaporation of small drops in a gaseous atmosphere, Physikalische Zeitschrift der Sowjetunion—Physikalische Zeitschrift der Sowjetunion, pp. 224–243, 1934.

Fukuta, N. and Walter, L. A.: Kinetics Of Hydrometeor Growth From A Vapor-Spherical Model, Journal Of The Atmospheric Sciences, 27, 1160–&, 1970.

Gorbunov, B., Baklanov, A., Kakutkina, N., Windsor, H. L., and Toumi, R.: Ice nucleation on soot particles, Journal Of Aerosol Science, 32, 199–215, 2001.

Hare, D. E. and Sorensen, C. M.: The Density Of Supercooled Water .2. Bulk Samples Cooled To The Homogeneous Nucleation Limit, Journal Of Chemical Physics, 87, 4840–4845, 1987.

Herich, H., Tritscher, T., Wiacek, A., Gysel, M., Weingartner, E., Lohmann, U., Baltensperger, U., and Cziczo, D. J.: Water uptake of clay and desert dust aerosol particles at sub- and supersaturated water vapor conditions, Geochimica Et Cosmochimica Acta, 73, A524–A524, 2009.

Hering, S. V., Stolzenburg, M. R., Quant, F. R., Oberreit, D. R., and Keady, P. B.: A laminar-flow, water-based condensation particle counter (WCPC), Aerosol Science And Technology, 39, 659–672, 2005.

Heymsfield, A. J. and Miloshevich, L. M.: Homogeneous Ice Nucleation And Supercooled Liquid Water In Orographic Wave Clouds, Journal Of The Atmospheric Sciences, 50, 2335–2353, 1993.

Hinds, W. C.: Aerosol Technology - Properties, Behavior, and Measurement of Airborne Particles, John Wiley & Sons, Inc., 1999.

Hobbs, P. V. and Rangno, A. L.: Ice Particle Concentrations In Clouds, J. Atmos. Sci., 42, 2523–2549, 1985.

Hoffer, T. E.: A Laboratory Investigation Of Droplet Freezing, Journal Of Meteorology, 18, 766–778, 1961.

Hoose, C., Lohmann, U., Erdin, R., and Tegen, I.: The global influence of dust mineralogical composition on heterogeneous ice nucleation in mixed-phase clouds, Environ. Res. Lett., 3, 2008.

Hung, H. M., Malinowski, A., and Martin, S. T.: Kinetics of heterogeneous ice nucleation on the surfaces of mineral dust cores inserted into aqueous ammonium sulfate particles, J. Phys. Chem. A, 107, 1296–1306, 2003.

Hussain, K. and Saunders, C. P. R.: Ice Nucleus Measurement With A Continuous-Flow Chamber, Quarterly Journal Of The Royal Meteorological Society, 110, 75–84, 1984.

Jiang, H., Xue, H., Teller, A., Feingold, G., and Levin, Z.: Aerosol effects on the lifetime of shallow cumulus, Geophysical Research Letters, vol.33, no.14, 4 pp., 2006.

Kanji, Z. A., Florea, O., and Abbatt, J. P. D.: Ice formation via deposition nucleation on mineral dust and organics: dependence of onset relative humidity on total particulate surface area, Environ. Res. Lett., 3, 2008.

Khain, A., Rosenfeld, D., and Pokrovsky, A.: Aerosol impact on the dynamics and microphysics of deep convective clouds, Quarterly Journal Of The Royal Meteorological Society, 131, 2639–2663, 2005.

Knopf, D. A. and Koop, T.: Heterogeneous nucleation of ice on surrogates of mineral dust, Journal Of Geophysical Research-Atmospheres, 111, 2006.

Koehler, K. A., Kreidenweis, S. M., DeMott, P. J., Petters, M. D., Prenni, A. J., and Carrico, C. M.: Hygroscopicity and cloud droplet activation of mineral dust aerosol, Geophysical Research Letters, 36, 2009.

Koop, T., Luo, B. P., Tsias, A., and Peter, T.: Water activity as the determinant for homogeneous ice nucleation in aqueous solutions, Nature, 406, 611–614, 2000.

Kulmala, M., Pirjola, U., and Makela, J. M.: Stable sulphate clusters as a source of new atmospheric particles, Nature, 404, 66–69, 2000.

Kumai, M.: Snow Crystals And The Identification Of The Nuclei In The Northern United-States Of America, Journal Of Meteorology, 18, 139–150, 1961.

Kumar, P. P., Broekhuizen, K., and Abbatt, J. P. D.: Organic acids as cloud condensation nuclei: Laboratory studies of highly soluble and insoluble species, Atmospheric Chemistry And Physics, 3, 509–520, 2003.

Levin, Z. and Yankofsky, S. A.: Contact Versus Immersion Freezing Of Freely Suspended Droplets By Bacterial Ice Nuclei, Journal Of Climate And Applied Meteorology, 22, 1964–1966, 1983.

Lide, D. R., ed.: CRC Handbook of Chemistry and Physics, CRC Press, Taylor & Francis Group, 89 edn., 2008.

Lohmann, U.: A glaciation indirect aerosol effect caused by soot aerosols, Geophysical Research Letters, 29, 2002.

Lohmann, U. and Diehl, K.: Sensitivity studies of the importance of dust ice nuclei for the indirect aerosol effect on stratiform mixed-phase clouds, J. Atmos. Sci., 63, 968–982, 2006.

Lohmann, U. and Feichter, J.: Global indirect aerosol effects: a review, Atmospheric Chemistry And Physics, 5, 715–737, 2005.

Marcolli, C., Gedamke, S., Peter, T., and Zobrist, B.: Efficiency of immersion mode ice nucleation on surrogates of mineral dust, Atmos. Chem. Phys., 7, 5081–5091, 2007.

Möhler, O., Stetzer, O., Schaefers, S., Linke, C., Schnaiter, M., Tiede, R., Saathoff, H., Kramer, M., Mangold, A., Budz, P., Zink, P., Schreiner, J., Mauersberger, K., Haag, W., Karcher, B., and Schurath, U.: Experimental investigation of homogeneous freezing of sulphuric acid particles in the aerosol chamber AIDA, Atmospheric Chemistry And Physics, 3, 211–223, 2003.

Möhler, O., Field, P. R., Connolly, P., Benz, S., Saathoff, H., Schnaiter, M., Wagner, R., Cotton, R., Kramer, M., Mangold, A., and Heymsfield, A. J.: Efficiency of the deposition mode ice nucleation on mineral dust particles, Atmospheric Chemistry And Physics, 6, 3007–3021, 2006.

Morrison, H. and Gettelman, A.: A new two-moment bulk stratiform cloud microphysics scheme in the community atmosphere model, version 3 (CAM3). Part I: Description and numerical tests, Journal Of Climate, 21, 3642–3659, 2008.

Murphy, D. M. and Koop, T.: Review of the vapour pressures of ice and supercooled water for atmospheric applications, Quarterly Journal Of The Royal Meteorological Society, 131, 1539–1565, 2005.

Nicolet, M.: Characterization of ice crystals and water droplets with the ice optical detector device (IODE) using depolarization measurements, Ph.D. thesis, ETH Zurich, 2008.

Nicolet, M., Stetzer, O., and Lohmann, U.: Depolarization ratios of single ice particles assuming finite circular cylinders, Appl. Opt., 46, 4465–4476, 2007.

Nicolet, M., Stetzer, O., and Lohmann, U.: Single ice crystal measurements during nucleation experiments with the depolarization detector IODE, Atmos. Chem. Phys. Discuss., 8, 20 965–21 000, 2008.

Niedermeier, D., Hartmann, S., Shaw, R. A., Covert, D., Mentel, T. F., Schneider, J., Poulain, L., Reitz, P., Spindler, C., Clauss, T., Kiselev, A., Hallbauer, E., Wex, H., Mildenberger, K., and Stratmann, F.: Heterogeneous freezing of droplets with immersed mineral dust particles - measurements and parameterization, Atmos. Chem. Phys. Discuss., 9, 15 827–15 865, 2009.

Pitter, R. L. and Pruppacher, H.: Wind-Tunnel Investigation Of Freezing Of Small Water Drops Falling At Terminal Velocity In Air, Quart. J. R. Met. Soc., 99, 540–550, 1973.

Pruppacher, H. R. and Klett, J. D.: Microphysics of Clouds and Precipitation, Kluwer Academic Publishers, 1997.

Richardson, M. S., DeMott, P. J., Kreidenweis, S. M., Cziczo, D. J., Dunlea, E. J., Jimenez, J. L., Thomson, D. S., Ashbaugh, L. L., Borys, R. D., Westphal, D. L., Casuccio, G. S., and Lersch, T. L.: Measurements of heterogeneous ice nuclei in the western United States in springtime and their relation to aerosol characteristics, Journal Of Geophysical Research-Atmospheres, 112, 2007.

Rogers, D. G.: Development of a continuous flow thermal gradient diffusion chamber for ice nucleation studies, Atmos. Res., 22, 149–81, 1988.

Rogers, R. R. and Yau, M. K.: A Short Course in Cloud Physics, Butterworth Heinemann, 1996.

Rosenfeld, D. and Woodley, W. L.: Deep convective clouds with sustained supercooled liquid water down to-37.5 degrees C, Nature, 405, 440–442, 2000.

Sassen, K.: Indirect climate forcing over the western US from Asian dust storms, Geophys. Res. Lett., 29, 2002.

Seinfeld, J. H. and Pandis, S. N.: Atmospheric Chemistry and Physics: From Air Polltion to Climate Change, Hoboken, N.J.: Wiley, 2006.

Sinnarwalla, A. M. and Alofs, D. J.: A cloud nucleus counter with long available growth time, Journal of Applied Meteorology—Journal of Applied Meteorology, vol.12, no.5, 831–5, 1973.

Stetzer, O., Baschek, B., Luond, F., and Lohmann, U.: The Zurich Ice Nucleation Chamber (ZINC) - A new instrument to investigate atmospheric ice formation, Aerosol Sci. Tech., 42, 64–74, 2008.

Szyrmer, W. and Zawadzki, I.: Biogenic and anthropogenic sources of ice-forming nuclei: A review, Bulletin Of The American Meteorological Society, 78, 209–228, 1997.

Toolbox: Air Properties, Internet database, http://www.engineeringtoolbox.com, 2005a.

Toolbox: Water Vapor Properties, Internet database, http://www.engineeringtoolbox.com, 2005b.

Toolbox: Water - Thermal Properties, Internet database, http://www.engineeringtoolbox.com, 2005c.

Twomey, S.: Pollution And Planetary Albedo, Atmospheric Environment, 8, 1251–1256, 1974.

Twomey, S. and Warner, J.: Comparison Of Measurements Of Cloud Droplets And Cloud Nuclei, Journal Of The Atmospheric Sciences, 24, 702–&, 1967.

Vali, G.: Atmospheric Ice Nucleation - A review, J. Rech. Atmos., 19, 105–115, 1985.

Vali, G.: Freezing Rate Due To Heterogeneous Nucleation, J. Atmos. Sci., 51, 1843–1856, 1994.

Vali, G.: Repeatability and randomness in heterogeneous freezing nucleation, Atmos. Chem. Phys., 8, 5017–5031, 2008.

Vali, G. and Stansbury: Time-Dependent Characteristics Of Heterogeneous Nucleation Of Ice, Canadian Journal Of Physics, 44, 477–502, 1966.

Voigtlander, J., Stratmann, F., Niedermeier, D., Wex, H., and Kiselev, A.: Mass accommodation coefficient of water: A combined computational fluid dynamics and experimental data analysis, Journal Of Geophysical Research-Atmospheres, 112, 2007.

Vonnegut, B. and Baldwin, M.: Repeated Nucleation Of A Supercooled Water Sample That Contains Silver-Iodide Particles, J. Clim. appl. Met., 23, 486–490, 1984.

Welti, A., Luond, F., Stetzer, O., and Lohmann, U.: Influence of particle size on the ice nucleating ability of mineral dusts, Atmos. Chem. Phys. Discuss., 9, 6929–6955, 2009.

Winkler, P. M., Vrtala, A., Wagner, P. E., Riipinen, I., Vesala, T., Lehtinen, K. E. J., Viisanen, Y., and Kulmala, M.: Condensation of water vapor: experimental determination of mass and thermal accommodation coefficients, Journal of Geophysical Research-Part D-Atmospheres, pp. 1–12, 2006.

Young, K. C.: Role Of Contact Nucleation In Ice Phase Initiation In Clouds, Journal Of The Atmospheric Sciences, 31, 768–776, 1974.

Zimmermann, F., Weinbruch, S., Schutz, L., Hofmann, H., Ebert, M., Kandler, K., and Worringen, A.: Ice nucleation properties of the most abundant mineral dust phases, Journal Of Geophysical Research-Atmospheres, 113, 2008.

Zobrist, B.: Heterogeneous ice nucleation in upper tropospheric aerosols, Ph.D. thesis, ETH Zurich, 2006.

Zobrist, B., Koop, T., Luo, B. P., Marcolli, C., and Peter, T.: Heterogeneous ice nucleation rate coefficient of water droplets coated by a nonadecanol monolayer, J. Phys. Chem. C, 111, 2149–2155, 2007.

Zuberi, B., Bertram, A. K., Koop, T., Molina, L. T., and Molina, M. J.: Heterogeneous freezing of aqueous particles induced by crystallized (NH4)(2)SO4, ice, and letovicite, Journal Of Physical Chemistry A, 105, 6458–6464, 2001.

Zuberi, B., Bertram, A. K., Cassa, C. A., Molina, L. T., and Molina, M. J.: Heterogeneous nucleation of ice in (NH4)(2)SO4-H2O particles with mineral dust immersions, Geophysical Research Letters, 29, 2002.

Acknowledgements

I would like to express my gratitude to all people from whom I obtained any kind of support for this PhD thesis. I thank

- Ulrike Lohmann, head of the atmospheric physics group, who gave me the opportunity to do my PhD thesis in her group. I appreciated her trust in me, even though experimental results were still missing after two and a half years...

- Olaf Stetzer, my direct supervisor, who helped me with a lot of scientific and technical advice, and always found some time to discuss problems. His optimism sometimes helped me to keep confidence in the experiments...

- Edwin Hausammann, for his unvaluable help in designing and constructing all parts of the IMCA chamber. I was very glad about his immense patience when I happened to come with urgent changes after a technical drawing had been finished...

- Hannes Wydler, who did a great job helping me to set up the electronics of IMCA. He always offered elaborate solutions in practically no time! And, after amusing himself about my solderings, he taught me how to use a soldering iron...

- Peter Isler, who did a lot of short-notice machining of IMCA-pieces in the workshop.

- Frank Stratmann, who agreed to be my external co-examinator.

- Zamin Kanji, for proof reading my thesis very attentively and giving valuable inputs in both scientific and language aspects.

- Pete, for a lot of inspiring discussions and some private classes in electronics. And also some competitions during the movie nights...

- Luis, for repeatedly passing me all the tools that I dropped from 3 m altitude when repairing the IMCA chamber...

- Marco and Doris, my office mates, who closed their eyes in front of the mess on my tables, and accepted my bike as a fourth office mate...

- My parents, for patiently listening to sorrows of any kind and for the relaxing sunday evenings.

- Stefanie, for her patience, comfort, encouragement and support of any kind. Tqm...!

- The Simpsons, for providing me a creative break now and then, during long working hours...

Curriculum Vitae

Felix Lüönd
born 22 November 1980 in Zürich, Switzerland
citizen of Sattel (SZ), Switzerland

Education

08/2006–10/2009	PhD studies at ETH Zürich, Institute for Atmospheric and Climate Science, under supervision of Prof. Dr. Ulrike Lohmann. Project funded by the Swiss National Funds (SNF).
10/2000–09/2005	Studies of physics at ETH Zürich and EPF Lausanne (Diploma degree Dipl. Phys. ETH). Diploma thesis (4 months research project) under supervision of Dr. Wolfgang Harbich, Institut de Physique des Nanostructures, EPF Lausanne.
01/2000	High-school graduation in Type A, Kantonsschule Hohe Promenade, Zürich

Professional Experience

01/2006–03/2006	Internship at Kistler Instrumente AG, Winterthur. Development of LabView software for a measurement setup.
2003–2004	Private teacher for mathematics and physics at Logos Lehrerteam, Zürich.
06/2000	Employee at the post office Briefzentrum Sihlpost, Zürich.

Conferences

International Conference on Nucleation and Atmospheric Aerosol (ICNAA), Prague, Czech Republic (2009)

British Association for Crystal Growth (BACG) Conference, Loughborough, UK (2008)

International Conference on Clouds and Precipitation (ICCP), Cancun, Mexico (2008)

Virtual Institute Aerosol Cloud Interaction (VI-ACI) meeting, Frankfurt, Germany (2008)

International Union of Geodesy and Geophysics (IUGG), Perugia, Italy (2007)

Teaching

Two lectures on heterogeneous nucleation, given on behalf of Prof. U. Lohmann, in Cloud Microphysics, MSc course in Atmospheric and Climate Sciences (2007 and 2008).

Supervised Master Thesis

André Welti: Influence of Particle Size on the Ice Nucleating Ability of Mineral Dusts, 2008.

Publications

Lüönd, F., Stetzer, O., and Lohmann, U. (2009): Experimental study on the ice nucleation ability of size selected kaolinite particles in the immersion mode, submitted to J. Geophys. Res.

Nicolet, M., Stetzer, O., Möhler, O., Lüönd, F., and Lohmann, U. (2009): Single ice crystal measurements during nucleation experiments with the depolarization detector IODE, submitted to Atmos. Chem. Phys.

Welti, A., Lüönd, F., Stetzer, O., and Lohmann, U.(2009): Influence of particle size on the ice nucleating ability of mineral dusts, Atmos. Chem. Phys. **9**, 6705–6715.

Stetzer, O., Baschek, B., Lüönd, F., and Lohmann, U. (2008): The Zurich Ice Nucleation Chamber (ZINC) – A new instrument to investigate atmospheric ice formation, Aerosol Sci. Tech. **42**, 64–74.